Spontaneous Brain Activity

How dynamics and topology shape the emergent correlation structure

Ruggero G. Bettinardi

TESI DOCTORAL UPF / 2016

Thesis Supervisor

Prof. Dr. Gustavo Deco,
Department of Information and Communication Technologies

ad Alice

Aknowledgements

"Happiness only real when shared"

Christopher McCandless

First and foremost, I want to warmly thank Gustavo Deco to have given to me the opportunity to start a PhD under his supervision; I really think he is one of the best mentors a young scientist could have: the one always present when needed, and that let you be free to work on the details and develop your own ideas and perspectives, intervening only when your enthusiasm deviates from logic, ready to listen your opinion, and that always makes you feel able to do whatever you are interested to do. This is, in my opinion, an invaluable way to let you grow the best you can. A mentor and a friend, that was able to create an amazing research group, made of many talented scientists that are, at the same time, wonderful persons: the computational neuroscience group have been, and will always be, a second family. Between them, I would like to specially thank those who directly supported me in my work during these years, and in completing this dissertation: Andrea Insabato, great friend and scientist, that helped me so much when I first joined the group, and still helps me patiently: I have not enough lines to thank him as much as he deserves; Marina Martínez-Garcia, that always endured me and taught me a lot while I was learning to program, as well as Tristan T. Nakagawa, and Miguel Lechón, whose ability in programming I still think is magic; Adrián Ponce-Alvarez, who friendly helped me so many times to understand how different models work; Romain Brasselet, wonderful friend and agile mind; Gorka Zamora López, who taught me and guided in understanding the fascinating and powerful realm of graph theory and network science: I still have so much to learn from him; Mario Pannunzi, with whom I learned so much -not only about the analysis of variance-, above all how

a scientist should think, and act: his teachings I will never forget. I really hope we will continue to work together.

Then, I would like to thank all my friends: Niccoló Gravina, Alessandro Larcher, Francesco De Martino, Andrea Galbiati, Ramón Nogueira, Victor Saenger, Emmanuel Biau, Francesca Branzi, Vicente Pallares, Beatrice Jobst, Tommaso Gagliardi, Josefina Cruzat, Silvana Silva, Marta Szabina-Papai, Matthieu Gilson, Patricio Donnelly, Adriá Tauste, Giovanni Maffei, Lorenzo Rinaldi, Irune Fernandez, Mabel Fernandez, Philipp Shustek, Iñigo Arandia, Laura Ferreri, Grazia Fino, Nicoló Cesana Arlotti, Cassandra Arce, Roberto Gonella, Alice Paglia, Mateus Coehlo, Martino Boniardi, Dario Pardini, Martina Federici, Miquel Lull, Jacobo Picardo, Janet Vidal, Luca Bergomi, Berend Hesselink, Allard Hesselink, Niccoló Bertini.

My mother Elisabetta, the best mother I could have ever imagined, my father Giorgio, and my fantastic sisters and brothers, Virginia, Sofia, and Gerardo. It is an honor to be your brother, and you make me happy; remember, always be what you want to be, and never abandon your passions, your dreams.

And finally, Alice; I will always be with you, and for you; wherever you are, there is my home, wherever you go, there is my heart. I love you.

I promised myself not to write romantic acknowledgements in this dissertations, to stay professional, but it has been impossible. I am grateful to all and each one of you for the person I am.

Thank you all.

Barcelona, July 2016.

Abstract

Neuroscientific research in the last decades has revealed that ongoing brain activity exhibits highly structured spatio-temporal patterns of neural activations. The fundamental core of this endogenously generated correlation structure reflects, to a large extent, the complex anatomical organization of the central nervous system, whereas the variability of spontaneous brain activity is determined by regional properties. These cellular and circuit properties are in turn modulated either by external stimuli and ongoing computations as well as by significant changes in local dynamics due to the internal system's physiology, such as sleep, or induced by external factors, such as injuries, diseases, hypnosis or psychoactive substances. In this dissertation we will demonstrate how manipulations of regional dynamics and of the topological structure defined by anatomy determine changes in the emergent large-scale correlation structure displayed by spontaneous brain activity, and how this can be used to shed light on the intriguing but still elusive relationship between structure and function.

Resumen

En las ultimas décadas, la investigación neurocientífica ha revelado que la actividad del cerebro exhibe patrones de activaciónes neuronales altamente estructurados, tanto espacialmente como temporalmente. El núcleo fundamental de esta estructura funcional endógena tende a reflejar la compleja organización del sistema nervioso central, y que por otro lado, la variabilidad de la actividad espontánea del cerebro es determinada por propriedades regionales. Estas propriedades celulares y de circuito son moduladas tanto por estimulación externa o procesamento de información que por cambios significativos en las dinámicas locales debidos a la fisiología del sistema, como en el caso del sueño, o inducídos por factores externos, como daños, enfermedades, hipnosis o substancias psicoactivas. En la presente tesis se demonstrará como manipulaciónes de las dinámicas locales y de la estructura topológica definida por la anatomia determínan cámbios en la emergente estructura de las correlaciónes entre distintas areas que caracteriza la actividad espontánea del cerebro, y como esto puede informar sobre la interesante pero elusiva relación entre estructura y función.

Contents

List of Figures xvi

Preface xxi

1 Spontaneous Brain Activity 1
- 1.1 Overview . . . 1
- 1.2 Measuring spontaneous activity . . . 9
  - 1.2.1 Energy consumption . . . 12
  - 1.2.2 Hemodynamic fluctuations . . . 13
  - 1.2.3 Electrical and magnetic oscillations . . . 24
  - 1.2.4 Anatomical Connectivity . . . 28
- 1.3 Brain Networks . . . 36

2 Modulating dynamics through anesthesia 41
- 2.1 Summary . . . 42
- 2.2 Introduction . . . 43
- 2.3 Materials and Methods . . . 44
  - 2.3.1 Animal preparation . . . 44
  - 2.3.2 fMRI recordings . . . 45
  - 2.3.3 In vivo LFP recordings . . . 48
  - 2.3.4 fMRI data analysis . . . 49
  - 2.3.5 Deep and light anesthesia . . . 50
  - 2.3.6 Coupled and uncoupled area pairs . . . 51
  - 2.3.7 Detection of functional communities . . . 52

2.3.8 LFP data analysis . . . 53
2.3.9 Frequency shift to higher frequencies . . . 54
2.4 Results . . . 55
2.4.1 Correlation increases as anesthesia fades away 55
2.4.2 Functional integration and segregation . . 58
2.4.3 Emergence of functional networks . . . 58
2.4.4 FC between areas of the same networks . . 62
2.4.5 Frequency-specific changes in neural coupling 62
2.4.6 Shifts to higher frequencies . . . 64
2.4.7 Similarity of fMRI and LFP time courses . 66
2.5 Discussion . . . 66
2.6 Limitations . . . 74
2.7 Conclusions . . . 75

3 Modelling brain activity 77
3.1 Introduction . . . 77
3.2 Conductance-Based Models . . . 80
3.3 FitzHugh-Nagumo Model . . . 83
3.4 Wilson-Cowan Model . . . 84
3.5 Spiking Neural Network Model . . . 85
3.6 Kuramoto Model . . . 89
3.7 Hopf Normal Model . . . 90

4 How topology sculpts interactions 93
4.1 Introduction . . . 93
4.2 Exploring simple topologies . . . 94
4.2.1 Single pair of nodes . . . 97
4.2.2 Adding leaves . . . 99
4.2.3 Chains . . . 103
4.2.4 Path redundancy . . . 106
4.2.5 Cycles . . . 109
4.3 Expected covariation . . . 113
4.4 Understanding empirical data . . . 115
4.5 Conclusions . . . 129

5 General discussion 131

I Appendix **137**

A Notes on the origins of spontaneous brain activity **139**

B Supplementary Materials **149**
B.1 Estimation of BOLD global synchronization . . . 156
B.2 Detection of functional communities and modularity 156
B.3 LFP data analysis . . . 157
B.4 Quantification of the frequency shift . . . 157

C Measuring graph properties **159**
C.1 Graph Density . . . 160
C.2 Degree and Strength . . . 163
C.3 Measures of Assortativity . . . 163
C.4 Clustering coefficient . . . 164
C.5 Path length . . . 166
C.6 Small-Worldness . . . 167
C.7 Communicability . . . 168
C.8 Expected covariation . . . 170

Bibliography **175**

List of Figures

1 Edwin Smith papyrus xxvii

1.1 Spontaneous co-activations resemble task 3
1.2 Ongoing fluctuations modulate evoked response's variability 4
1.3 Intrinsic fluctuations exhibit temporal structure . . . 5
1.4 Task-independent decreases observed in fMRI 6
1.5 Comparative view of the DMN 7
1.6 Resting-State Networks derived from ICA 8
1.7 Structural levels of organization of the CNS 10
1.8 Spatio-temporale scales of different techniques 11
1.9 Energetic demand cortical functions 12
1.10 Global cortical metabolism explains level of awareness. 14
1.11 Simple behaviors can affect BOLD fluctuations . . . 15
1.12 Probability to fall asleep increases with resting-state scan duration. 17
1.13 Frequency bands sampled in rs-fMRI 19
1.14 Intrinsic activity recapitulates task and anatomy. . . 19
1.15 Reproducibility of RSN spatial maps 21
1.16 Reliability of resting-state correlations 22
1.17 Overview of neural oscillations. 25
1.18 Power envelope correlations 27
1.19 Tracking connectivity ex vivo 30
1.20 Diffusion Spectrum Imaging 31

1.21 Tractography is affected by distance 32
1.22 Comparison between tractography and tract-tracing . 33
1.23 Tractography can detect important pathways 34
1.24 Reconstructed pathways underlying DMN 35
1.25 Analyzing brain networks 38

2.1 Experimental Protocol and recorded areas 46
2.2 Fading of anesthesia associated with changes in brain activity 57
2.3 Different brain states are mirrored by different properties of the underlying functional networks 60
2.4 Networks' stability increases while anesthesia fades out 61
2.5 BLCs discriminate between network areas and different brain states 65
2.6 BOLD correlations and BLCs of specific frequency ranges exhibit comparable time courses 67

3.1 Overview of the Hopf model 92

4.1 Simple network topologies 95
4.2 Single pair of nodes 98
4.3 Adding leaves 100
4.4 Effect of adding leaves to the reference nodes 101
4.5 Effect of chain length and strength 104
4.6 Redundant paths of different length 107
4.7 Effect of Redundant paths 108
4.8 Cyclic topologies 109
4.9 Triangular networks 111
4.10 Effect of cycles 112
4.11 Empirical structural and functional data 117
4.12 Joint clustering coefficient and assortativity 118
4.13 Fit between models and empirical data 120
4.14 Comparison between numerical and analytic results . 121
4.15 Relative network layers 123
4.16 Adding link procedure 124
4.17 Effect of varying topology 125
4.18 Quantification of whole-network contribution 128

A.1 Up and Down states observed in the anesthetized mouse 141

A.2 Spike correlations in spontaneous and evoked activity 142
A.3 Axonal projections and spontaneous cortical correlations 143
A.4 Genetic contribution to anatomical and spontaneous connectivity 144
A.5 Spontaneous activity in the zebrafish larva 147

B.1 fMRI: Gradual changes in signal variability and FC as anesthesia naturally fades out 150
B.2 Individual FC time courses of a subset of cortical ROIs 151
B.3 Individual FC time courses of a subset of subcortical ROIs 152
B.4 Scatterplots of variables measuring different aspects of functional dynamics 153
B.5 Ketamine/medetomidine modulation of the power spectra in deep and light intervals 154
B.6 BLC time courses of all area pairs simultaneously recorded in LFP experiments and BOLD FC time courses of the corresponding ROIs 155

C.1 Graph representation 161
C.2 Weighted and adjaency matrices 162
C.3 Graph density 162
C.4 Local clustering coefficient 165
C.5 Shortest path 167
C.6 Small-world topology 169

Men ought to know that from nothing else but the brain come joys, delights, laughter and sports, and sorrows, griefs, despondency, and lamentations. And by this, in an especial manner, we acquire wisdom and knowledge, and see and hear and know what are foul and what are fair, what are bad and what are good, what are sweet and what are unsavory. And by the same organ we become mad and delirious, and fears and terrors assail us. All these things we endure from the brain when it is not healthy. In these ways I am of the opinion that brain exercises the greatest power in the man.

Hippocrates (460-370 B.C.)

The Brain - is wider than the Sky
For - put them side by side
The one the other will contain
With ease - and You - beside

The Brain is deeper than the sea
For - hold them - Blue to Blue
The one the other will absorb
As Sponges - Buckets - do

The Brain is just the weight of God
For - Heft them - Pound for Pound
And they will differ - if they do
As Syllable from Sound.

Emily Dickinson (1830-1886)

Preface

> "The most beautiful thing we can experience is the mysterious. It is the source of all true art and science."
>
> Albert Einstein

The brain has been repeatadly described as one of the most complex object in the known universe. This opinion reflects our still young knowledge about its organization and functions, and our apparently intrinsic difficulty to intimately understand how this physical object gives rise to ourselves. We now know what Hippocrates already suggested more than two thousand years ago, namely that the brain is the organ responsible for all what we feel, do, and are: nonetheless, we still strive to find a satisfactory explanation of how matter becomes thought.[1] We know so many things about the brain, and still so few. This makes the brain not only one of the most complex object in the universe, but also one of the most mysterious, and thus most fascinating.

This dissertation will focus on just a small region of the vast unkown territories of the brain. However small, this region is indeed

[1] This sentence paraphrases the title of a book written by Nobel laureate Gerald Edelman together with neuroscientist Giulio Tononi, "A universe of consciousness. How matter becomes imagination" (2000).

capital, dealing with the intriguing interplay between anatomical and functional structure, two fundamental aspects of this fascinating object that is, ultimetely, us.

The **First Chapter** (1) introduces the phenomenon of spontaneous brain activity, consisting in intrinsically generated patterns of neural activations present even during sleep, anesthesia and in absence of overt experimental manipulation, and observed in humans as well as in other animals. Understanding what spontaneous brain activity is, what causes it, and what is its function is crucial if we ought to understand how the brain works: spontaneous brain activity never ceases until the death of the organism, and it is responsible for around 20% of all body's energy consumption. In addition, as we will see, endogenous brain activations are far from being random, but instead mirror an highly structured spatio-temporal organization. As such, one cannot have a complete understanding of the brain without accounting for its intrinsic ongoing activity.

Spontaneous brain activity never stops, but it does change, giving rise to different behavioral states such as conscious wakefulness, drowsiness, or sleep. Endogenous activity can in fact exhibit different dynamical regimes, consisting of more or less widespread changes in the spatial and temporal organization of neural activity. Characterizing different states, and what drives the change from one global state to another, is of enormous importance to understand the functional role of the different shades of spontaneous activity. To this aim, in the **Second Chapter** (2) we will explore how experimental manipulation of local brain dynamics -through anesthesia- dramatically modulates the resulting functional organization of ongoing brain activity at different spatial and temporal scales.

As mentioned above, large-scale spontaneous activity cannot be explained by simple stochastic fluctuations, but instead recapitulates to a large extent the anatomical structure of the brain, which in turn plays a fundamental role in determining function. The following part of this dissertation will thus be focused -by means of simulations- on investigating how much of endogenous brain ac-

tivity can be understood in terms of the underlying anatomical constraints.

With this in mind, in the **Third Chapter** (3) we will first review some of the most commonly used mathematical models of mesoscopic brain activity, and will introduce the Hopf model, a phenomenological model that we will later use in the following chapter to approximate local brain dynamics and simulate large-scale spontaneous activity.

The **Fourth Chapter** (4) is dedicated to the contribution of network topology in weaving the fundamental structure of spontaneous brain activity. Topology is that branch of mathematics that studies spaces whose fundamental properties do not change under continuous deformations. Reporting a classic example, squares and circles are different geometrical shapes that however belong to the same topological class, as one can be obtained deforming the other: in fact, both shapes are different instances of the same fundamental topological structure, namely an object with one hole. In the framework of network science -the approach that we will adopt- topology refers to the geometric properties of networks (also called *graphs*). In this dissertation, the networks that we will use will be those describing the anatomical connections between different brain regions. In this chapter, we will first evaluate how networks with different structures (*i.e.* networks having different topologies) determine different synchronization properties between their elements, and then we will introduce a novel measure able to predict the expected synchronization between different elements of the network just by using the information about the topological structure of the network itself. Finally, we will use this novel measure to estimate the average correlation structure of empirical data, and compare the results with those obtained using a dynamical model of mesoscopic activity.

We will finally discuss (**General discussion**, 5) the most important results and findings, trying to put them in perspective and elaborating on the relationship between structure and function in determining the complex correlation patterns characterizing spontaneous brain activity.

The study presented in **Chapter 2** reproduces the below listed publication, as indicated in the corresponding chapter:

"Gradual emergence of spontaneous correlated brain activity during fading of general anesthesia in rats: evidences from fMRI and local field potentials." Bettinardi, R.G., Tort-Colet, N., Ruiz-Mejias, M., Sanchez-Vives, M.V., & Deco, G. (2015). *Neuroimage*, 114, 185-198

Chapter 1 introduce two papers in preparation (see Figure 1.16 and Figure 1.21) listed below:

"Characterizing the reliability and the variability of resting-state fMRI functional correlations: intrinsic and finite-sample variability." Pannunzi M., Hindriks R., Bettinardi R.G., Kuhn S, & Deco G

"Cross-subject and empirical variability in human structural brain connectivity: reliability of link weights." Zamora-López G., Bettinardi R.G., Pannunzi M., & Deco G.

The work presented in **Chapter 4** reflects two papers in preparation, listed below:

"Understanding how simple network topologies affects the correlation of single pairs of nodes." Bettinardi R.G., Zamora-López G., & Deco G.

"Expected covariation: an analytic approach to link topological structure and the emergent organization of networks." Bettinardi R.G., Zamora-López G., & Deco G.

Figure 1: One column of the Edwin Smith papyrus. This papyrus, written in Egypt around the 7th century B.C., is the most ancient document referring to the brain. It describes different surgical practices, and summarize symptoms and diagnoses of two subjects that suffered from brain injuries.

Chapter 1

Spontaneous Brain Activity

"The brain is a world consisting of a number of unexplored continents and great stretches of unknown territory"

Santiago Ramón y Cajal

1.1 Overview

The brain is always active. Even when someone is not actively performing any kind of motor or cognitive task, is sleeping or even anesthetized, brain activity never ceases: it just changes.

The continuous spontaneous activity of the brain has been observed many times from the introduction of tecnhiques that allowed to record the electrical activity of the brain, first developed in 1875 by Richard Caton (Haas, 2003; Coenen et al., 2014). The metabolyc consumption of the brain during wakeful rest is remarkably similar to that measured during performance of demanding tasks requiring active concentration (Sokoloff et al., 1955; Buckner and Vincent, 2007) and tends to diminish during sleep or anesthesia (Braun et al., 1997; Alkire et al., 1997). Indeed, behaviorally different states mirror different dynamical regimes of the underlying overall brain activity. These global

states can either be physiological (as drowsiness, sleep and wakefulness), induced (through anesthesia, psychotropic agents, or relaxation) or pathological (vegetative state, coma, mood disorders, delusional conditions). As in the case of task-specific activations, during these states the brain reveals different patterns of activity that, far from being explained just by random fluctuations, have demonstrated to be robust and informative.

While the majority of studies in cognitive neuroscience had classically focused on the neural correlates of different task-related behaviors as movement, perception and higher cognitive operations as language processing and problem-solving (Cabeza and Nyberg, 2000), interest in spontaneous (*i.e.* not overtly task-driven) brain activations arose only recently during the last twenty years, after the finding that those brain areas which were found to be co-activated during specific finger movements tended to exhibit correlated activations also during rest (Biswal et al. 1995, see Figure 1.1).

This finding was critical for the traditional subtractive method routinely applied in functional neuroimaging studies (Ogawa et al., 1990a), whose results relied on the comparison with a baseline activity in order to infer task-induced activations. In fact, the implicit assumptions underlying the use of the subtractive method was the idea that ongoing spontaneous brain activity could be considered, at least as a first approximation, as unstructured noise. This assumption was motivated by the observation that, at a much smaller scale, the precise pattern of action potentials generated by individual neurons was not deterministic, but exhibited some degree of stochasticity (Stein et al., 2005); this unpredictability have been linked with the apparent stochastic nature of the opening dynamics of ion channels on the neuron's membrane (Faisal et al., 2008; Yarom and Hounsgaard, 2011). Recent findings are shedding light on the laws governing the emergence of structured oscillations from an underlying background stochasticity (Sancristbal et al., 2016), help bridging the apparent discrepancy between observations at the microscopic and at the mesoscopic scale.

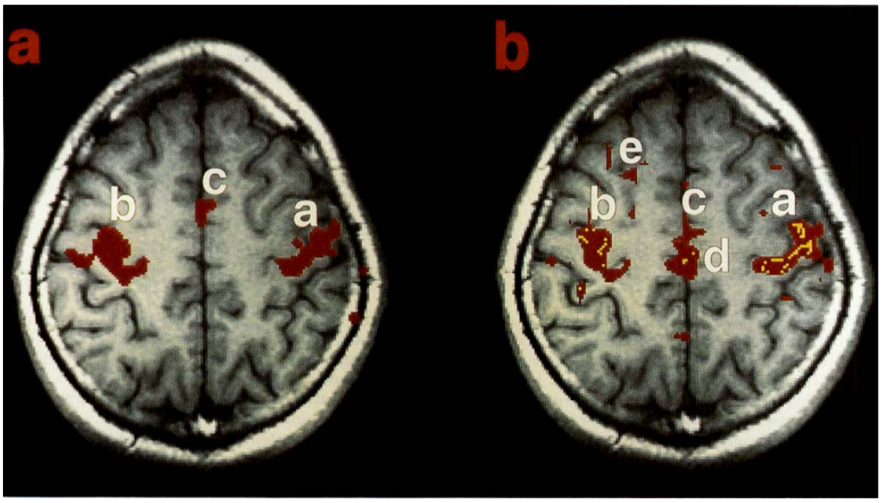

Figure 1.1: Spontaneous co-activations resemble task. The first evidence that spontaneous brain co-activations resembled that observed during task. (Left) fMRI activations in response to bilateral finger movement. (Right) BOLD fluctuations obtained during rest. Regions marked as (a,b,c) are those that showed statistical similarities between the two conditions, whereas (d,e) those markedly present only during rest. Figure from Biswal et al. 1995.

The observation that the spontaneous activity of the cerebral cortex strikingly resembled that observed during a specific voluntary task (Biswal et al., 1995) prompted interest in trying to understand the details of the relationship between ongoing and evoked activity, which was crucial to properly analyze and interpret findings obtained during most of the experiments performed in neuroscience. In a seminal paper, Arieli and colleagues (1996) demonstrated that the inter-trial variability in evoked activations was in fact due to the specific underlying dynamics of ongoing brain activity; the authors showed that singe trials responses could be predicted by a linear summation of the cortical ongoing activity preceding the stimulus and the deterministic response (see Figure 1.2), suggesting that cortical ongoing activity must play an important role and that proper neurophysiological investigation of cognitive processes cannot neglect the modulation exerted by

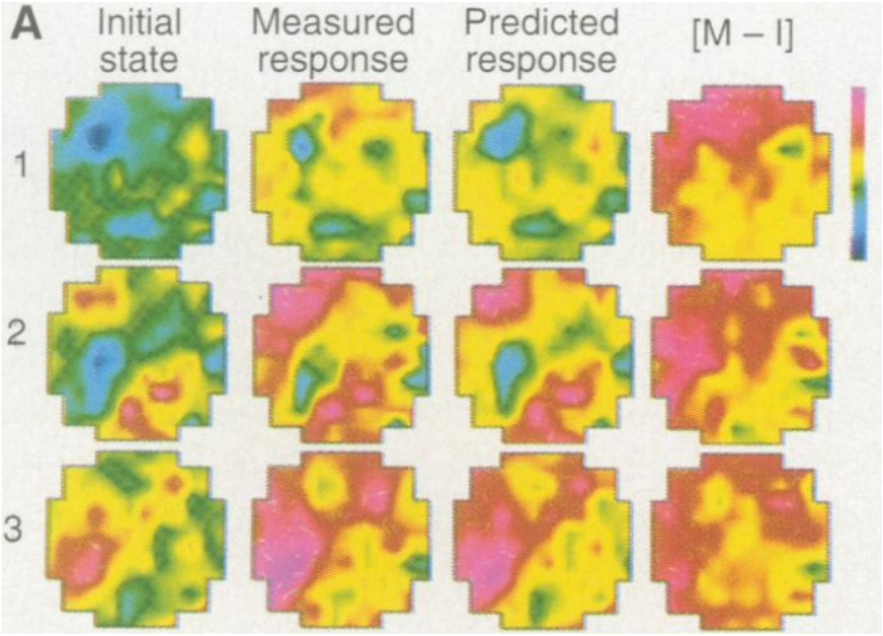

Figure 1.2: Ongoing fluctuations modulate evoked response's variability. Ongoing fluctuations can be used to predict evoked response's variability of cat visual cortex using optical imaging. Examples from three consecutive trials responses (rows 1,2,3) to the same visual stimulus. The four columns show the activity measured at time 0, the measured response, the predicted one, and the difference between the measured response and the initial state (M-I), *i.e.* the net effect produced by the stimulus. The color code corresponds to the intensity of the signal. Figure adapted from Arieli et al. 1996.

spontaneous activity.

It became clear that these spontaneous dynamics couldn't be considered just unstructured random fluctuations, as they exhibited rich patterns of spatiotemporally organized activations (Gusnard and Raichle, 2001; Beckmann et al., 2005) and deactivations (Mazoyer et al., 2001; Shulman et al., 2004; Fransson, 2006), as illustrated in Figure 1.3.

The measurement of oxygen extraction fraction performed using Positron Emission Tomography (PET) and of oxygenation of the

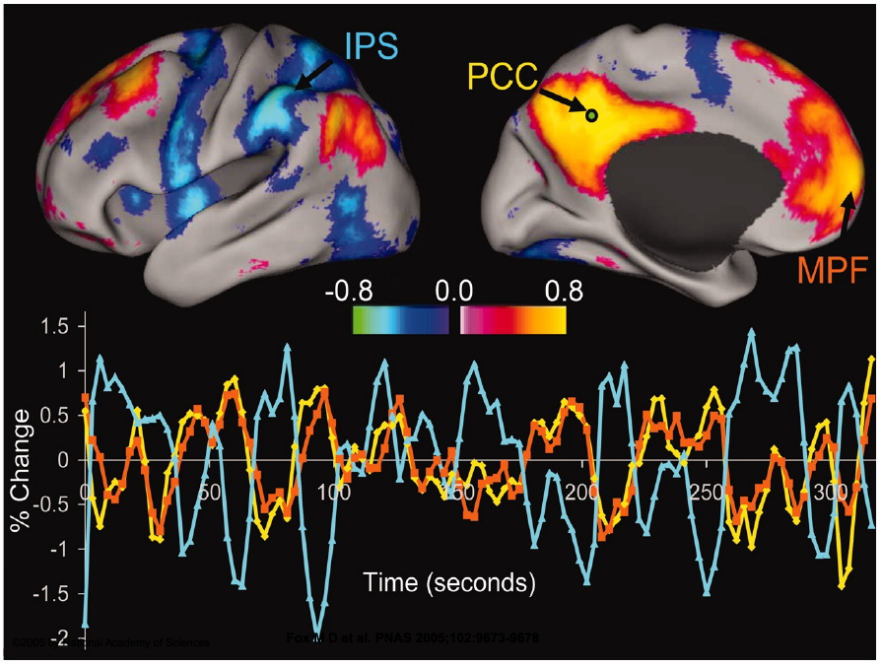

Figure 1.3: Intrinsic fluctuations exhibit temporal structure. Intrinsic temporal correlations between a seed region in the posterior cingulate/precuneus (PCC), the intraparietal sulcus (IPS) and medial prefrontal cortex (MPF). The PCC (yellow) is a region positively correlated with the MPF (orange) whereas negatively correlated with the IPS (blue) during rest. Reproduced from Fox et al. (2005).

regional blood flow using fMRI performed during rest unveiled the existence of a well defined subset of brain regions that systematically showed decreased activity during classical task-paradigms, and that had been implicitly considered as non relevant to function in most of previous studies (Raichle et al., 2001; Gusnard and Raichle, 2001); the authors of such discovery suggested that the activity of those areas could be considered as a physiological baseline of brain activity, that they baptized as *default mode*. Further studies confirmed the presence of a specific and reliable network of areas whose co-activations tended to decrease during the majority of tasks but systematically increased their glucose metabolysm (measured with PET) during passive rest (Greicius

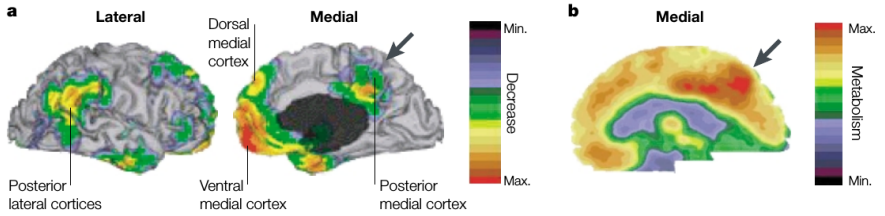

Figure 1.4: Task-independent decreases observed in fMRI. Systematic task-independent decreases observed in functional imaging experiments. (a) Task *vs.* Rest decrease obtained averaging PET scans of 132 healthy subjects performing different type of tasks. (b) Areas associated with increased glucose metabolism rate during rest in 22 healthy adults. Reproduced from Gusnard and Raichle (2001).

et al. 2003 see also Raichle and Snyder 2007). This set of regions, referred to as *default-mode network* (DMN) in most of the corresponding literature, comprised midline areas within the medial prefrontal cortex, the precuneus and the posterior cingulate (see Figure 1.4).

Since its discovery, many studies have focused on trying to elucidate the elusive functional role of this network of areas, that have been shown to be associated to a plethora of different self-referential and relatively task-independent cognitive operations (Fransson, 2005; Mason et al., 2007), and recent findings suggested that regions of the DMN appear to be eminent targets of powerful psychotropic substances such as psylocibin (Carhart-Harris et al., 2012). Despite the current debate about the role of this network, the fact that this peculiar pattern of activations is systematically found in humans (Damoiseaux et al., 2006) as well as in other mammals as monkeys (Vincent et al., 2007) and rats (Lu et al., 2012; Bettinardi et al., 2015) (see Figure 1.5), argues in favor of its likely relevant role.

The application of Independent Component Analysis (ICA) to fMRI data obtained during rest has proven to be crucial to disentangle the overall spontaneous activity of the brain into its likely independent neural sources, revealing that the intrinsic dynamics of the resting brain exhibit also other specific patterns of activa-

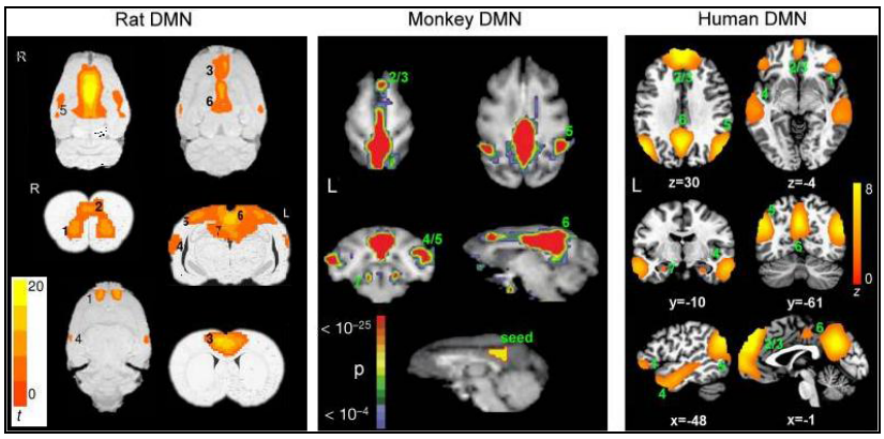

Figure 1.5: Comparative view of the DMN. Comparison of the Default-Mode Network (DMN) in rats, monkeys and humans. The three panels shows those regions whose activity tends to increase during rest and light sedation. Adapted from Lu et al. (2012).

tions that are different from those of the DMN and whose spatial organization resemble in a non-trivial manner those of different well-known task-positive functional networks (Beckmann et al., 2005; Smith et al., 2009). These sets of regions, which showed highly correlated activity during rest, have been called *resting-state networks* (RSN, Figure 1.6).

RSNs are interesting for more than one reason: first of all, as we said, their presence is consistently found both across species as well as individuals (Fox et al., 2005; Biswal et al., 2010; Snyder and Raichle, 2012; Choe et al., 2015); second, the different RSNs usually found with ICA are not just spatially segregated, but also temporally, as the activity of the different areas within a network is characterized by positive temporal correlations whereas the temporal correlation between the activity of areas pertaining to different RSNs is lower or even negative (Fox et al., 2005); third, the group of regions belonging to given RSNs tend to be activated together also during tasks (Biswal et al., 1995; Beckmann et al., 2005); finally, growing evidences suggest a link between abnormal resting-state dynamics and several disorders such as

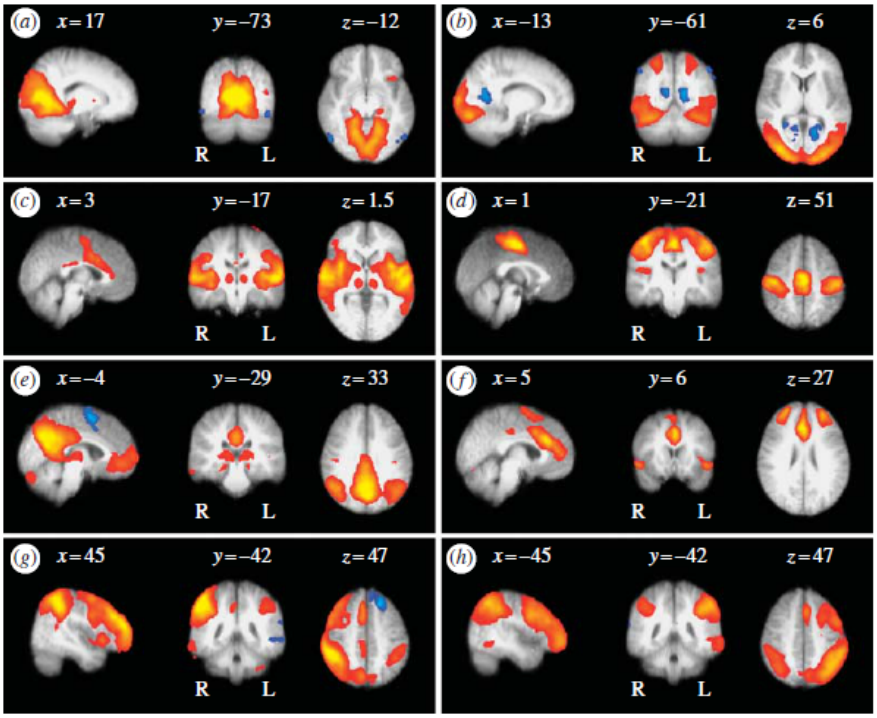

Figure 1.6: ICA based Resting-State Networks (RSNs). The hypothesized function of these networks are (a) primary vision, (b) higher order visual processing, (c) hearing, (d) sensory-motor, (e) self-referential focus, (f) salience processing, (g,h) executive control. Adapted from Beckmann et al. (2005).

Schizophrenia (Whitfield-Gabrieli et al., 2009), Autism (Kennedy and Courchesne, 2008), Alzheimer Disease (Damoiseaux et al., 2012), Multiple Sclerosis (Faivre et al., 2012), Major Depression (Greicius et al., 2007), vegetative state (Cauda et al., 2009): thus resting-state fMRI (rs-fMRI) could also serve, once properly tested for specificity and sensitivity, as a useful diagnostic tool.

Despite the intriguing similarities observed between the spatial distribution of intrinsic co-activations and task-evoked activity (Smith et al., 2009), it is important to stress that even if a given cognitive process may increase the activation of a certain brain region, the activation of that brain region does not necessar-

ily mirrors the occurrence of the cognitive or motor operation (Biswal et al., 1995); this type of reverse inference should indeed be avoided, as potentially misleading (Poldrack, 2006). In addition, findings that strikingly similar patterns of spontaneous covariations have been observed also during sleep (Horovitz et al., 2009), anesthesia (Vincent et al., 2007; Greicius et al., 2008), and seem to be conserved at least across mammals (Vincent et al., 2007; Liang et al., 2011; Lu et al., 2012) suggest a likely primitive, basal origin for these robust patterns of intrinsic fluctuations; in Appendix A we will try to offer an overview of the possible origins and functions subserved by spontaneous brain activity.

1.2 Measuring spontaneous activity

> "It makes no sense to read a newspaper with a microscope."
>
> Valentino Braitenberg

As many real systems, the brain is a fundamentally integrated entity, a system whose individual elements are inherently interdependent at different spatial and temporal scales, thus making them behaving collectively as a whole. Nonetheless, it is possible to study both structural and functional brain organization at different levels of observations (see Figure 1.7), adopting an analytic strategy at the very foundation of scientific approach (Marr, 2010; Churchland and Sejnowski, 1994).

The different level of observations can in fact be studied as relatively self-contained sub-systems, allowing great insights on the mechanisms underlying the emergence of the complex organization and dynamical processes observed both at lower and higher levels (Bertalanffy, 1968). It should be stressed that, even if those explanatory principles underlying the behavior at the smaller scales of a system are indeed necessary (and very likely sufficient) to the emergence of *all* those properties exhibited at higher levels of observation, the more far apart in space and time two distinct

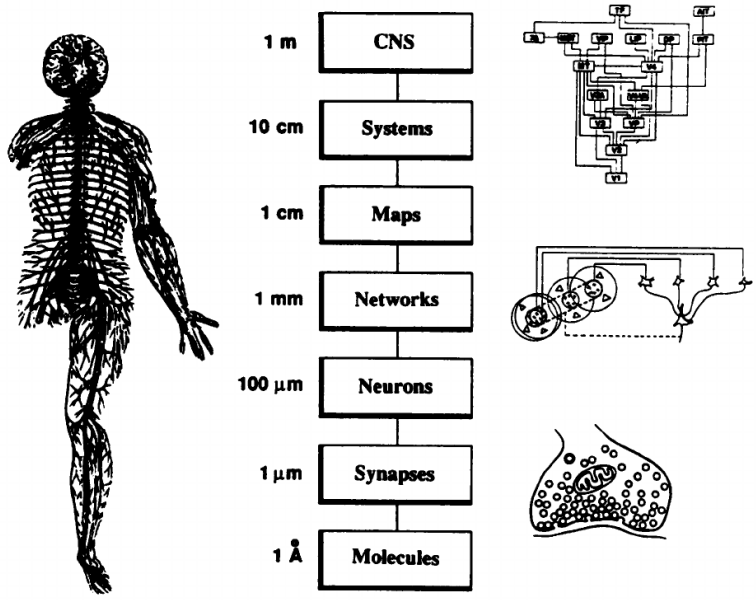

Figure 1.7: Structural levels of organization of the CNS. The spatial scale at which the structural CNS organization can be described spans over many orders of magnitude. Icons on the right represent distinct level of representation: (top) a subset of areas in visual cortex; (middle) a network model of the connectivity between ganglion cells and neurons in the visual cortex; (bottom) a chemical synapse. Reproduced from Churchland and Sejnowski (1988).

levels of observations A and B are, the more difficult will be trying to explain one as a function of the other; in fact, the complexity of the function linking A and B (function that surely *does* exist) is itself a function of all those nested functions describing the interactions between the elements at all smaller scales. A very difficult enterprise, but in principle not impossible. This also implies that the closer two levels of observations are, the simpler will be to use knowledge acquired from one of them to understand the other.

At present, there exist a plethora of different techniques used to measure structural and functional properties of the central nervous system (CNS), each of them able to sample specific spatio-

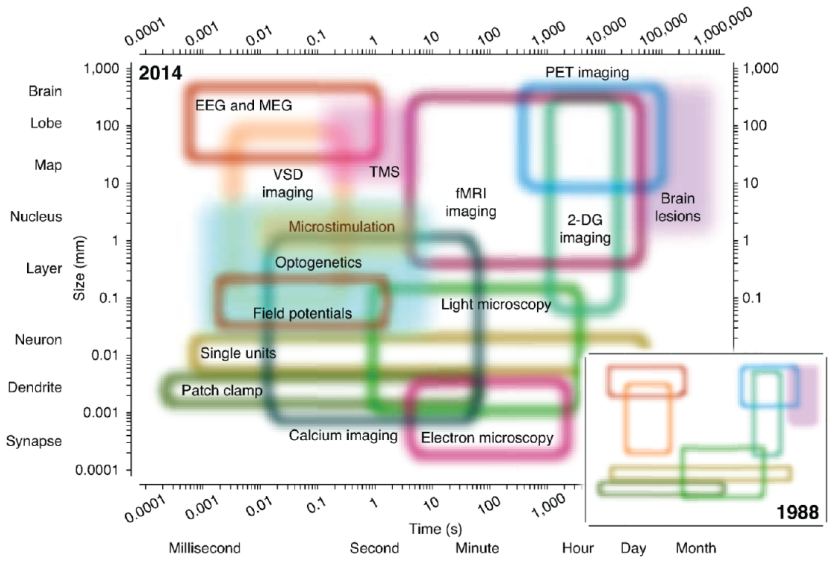

Figure 1.8: Spatio-temporale scales of different techniques. Each coloured perimeter represents the spatio-temporal domain of a given method. Open regions correspond to measurement tecnhique, whereas filled one to perturbational methodologies. *EEG*, electroencephalography, *MEG*, magnetoencephalography, *PET*, positron emission tomography, *VSD*, voltage-sensitive dye, *TMS*, transcranial magnetic stimulation, *2-DG*, 2-deoxyglucose. Reproduced from Sejnowski et al. (2014).

temporal scales, and the pace at which new techniques are developed is increasing (see Figure 1.8) due to significative technological and computational advances (Sejnowski et al., 2014).

The spatial and temporal constraints intrinsic to each tecnhique bound the domain of scientific questions that it can legitimately try to answer; paraphrasing Logothethis (Logothetis, 2008): would a given spatio-temporal resolution be enough to understand a given brain function? How far can we stretch interpretations or implications of findings obtained at a given spatio-temporal scale, and measuring a given variable? In the following sections, we will review some of the most relevant tecnhiques used to sample spon-

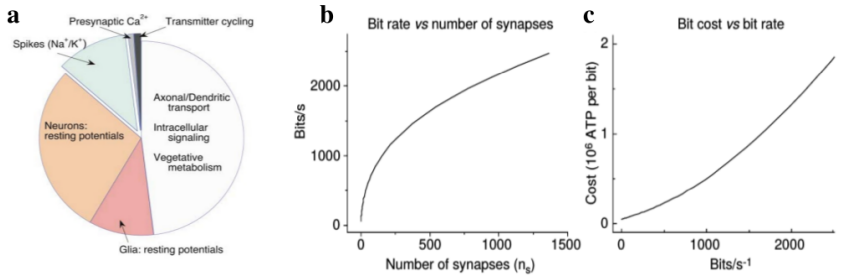

Figure 1.9: Energetic demand of cortical activity. (a) Fractions of total energy expenditure of human cortical pyramidal neurons, estimated -after proper scaling- from rat's pyramidal neurons (Attwell and Laughlin, 2001). (b,c) The number of synapses that code a signal increases both the rate at which information is transmitted (bit rate), and the energetic cost of each bit, given as the number of hydrolised ATP molecules in blowfly photoreceptors. Panels adapted from Lennie 2003 (a) and Laughlin 2001 (b,c).

taneous brain activity, together with the main contributions they made to our understanding of brain organization.

1.2.1 Energy consumption

The human brain represents around 2% of the total body mass, and nonetheless its spontaneous activity consumes approximately 20% of all body's energy (Shulman et al., 2004), mainly devoted at sustaining ongoing neural signalling and cellular basal metabolism, functions that both require high amounts of energy (Ames III 2000; Attwell and Laughlin 2001; Laughlin 2001; Lennie 2003, see Figure 1.9).

In comparison, task-related modulation of brain metabolism are rather small, accounting for <5% (Raichle and Mintun, 2006). This observation implies that intrinsic activity appear to be much more significant than task-evoked one, at least in terms of overall brain energy expenditure (Raichle, 2006). One of the most prominent methodologies to study whole brain metabolism is positron emission topography (PET), which is based on the ability to de-

tect the location in space where molecules of an injected radioactive tracer spontaneously annihilate. Depending on the radiotracer used, PET is able to sample different properties of a tissue. In neuroscience, distinct radiotracers can be used to quantify oxygen consumption (oxygen-15), glucose metabolism (FDG), or to detect the ligand site of different neurotransmitters. The spatial resolution of PET is in the scale of millimeters, whereas its temporal one crucially depends on the kinetics of the particular radiotracer used (in particular its half-life), which makes PET a rather "slow" methodology (minutes). Despite its low temporal resolution, PET has been showed to be able to capture regional differences in brain metabolism associated with different cognitive operations (Cabeza and Nyberg, 2000). Recently, the spontaneous overall glucose metabolism have been directly associated with the global state of consciousness: in fact the average metabolic index (obtained from whole-brain FDG-PET) revealed to be a fairly good predictor of the awareness level (as measured with traditional clinical scales) observed at follow-up in patients diagnosed with unresponsive wakefulness syndrome (Stender et al. 2016, see Figure 1.10).

This findings suggested the existence of a minimal amount of energy required by the brain to sustain conscious awareness, which is in fact in accordance to previous evidences that proper neural functioning is determined and constrained -not surprisingly- by the amount of energy needed to ignite and sustain all the mechanisms underlying a given operation (Laughlin, 2001).

1.2.2 Hemodynamic fluctuations

At the present time, one of the most widely used methodology for studying large-scale spontaneous activations *in vivo* is functional magnetic resonance imaging (fMRI), which builds upon the capacity of MRI of sampling changes in the magnetic properties of different tissue following a perturbation of the magnetic field around the brain, and extends it to quantify regional changes in the concentration of oxygen delivered by blood: this particular contrast, possibly the most frequently used, lead to what is

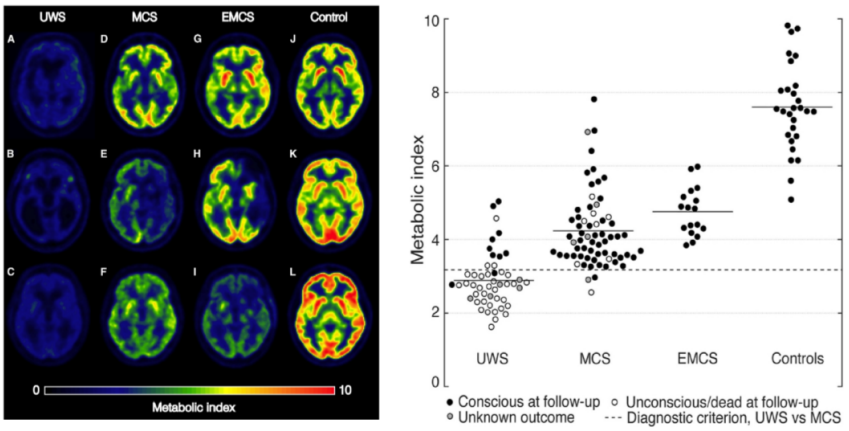

Figure 1.10: Global cortical metabolism accounts for the level of awareness. (Left) Individual FDG-PET examples. UWS, unresponsive wakefulness syndrome; MCS, minimally conscious state; EMCS, emergence from MCS. (Right) Global brain glucose metabolism. The dashed line marks the optimal diagnostic cutoff between patients in UWS and MCS. Horizontal lines mark the group averages. Metabolic values are indicated as a unitless index, with average activity in the reference area (extracerebral tissue) set to 1. Adapted from Stender et al. 2016.

referred to as the blood-oxygen-level-dependent (BOLD) signal (Ogawa et al., 1990b). Differences in the relative change of the BOLD signal can in fact be associated to differences in behavior, and can be used to detect those portions of the brain associated with different behaviors or general cognitive operations (see Figure 1.11).

The main advantage of this technique lies in its non-invasivity, a relatively high spatial resolution (depending on the force of the magnetic field and the acquisition sequence) and its ability to simultaneously measure the ongoing acivity of the entire brain. Nonetheless, as any other hemodynamic-based methodology, fMRI generates a surrogate signal, which is only indirectly related with the underlying activity of large neural masses (Lo-

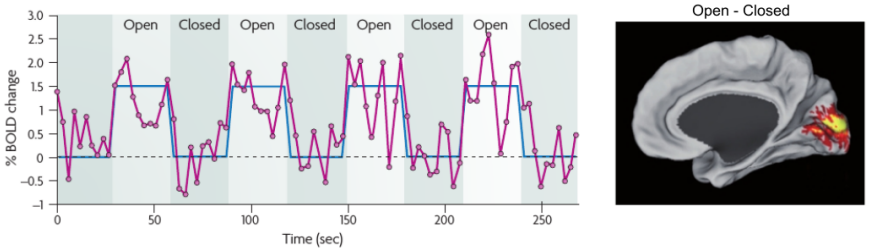

Figure 1.11: Simple behaviors can affect BOLD fluctuations. BOLD signal change is associated with corresponding changes in simple behaviors. (Left) BOLD time course (magenta) from V1 during a simple task requiring subjects to open and close their eyes, whereas the paradigm is shown in blue (note that the line corresponding to the paradigm has been delayed to account for the hemodynamic response). (Right) Subtraction of the two conditions allows to isolate the region corresponding to the difference in BOLD signal intensity. Adapted from Fox and Raichle 2007.

gothetis, 2008). As such, the ability of this method to unveil the detailed mechanism underlying neural activations crucially depends on extensive prior knowledge of the functioning and the connectivity of the units forming large-scale interacting neural populations, joint to very carefully planned experimental conditions explicitly designed to discriminate between different alternative explanations. In an influential review, Nikos K. Logothetis pointed out several important limitations of fMRI, such as the fact that it cannot distinguish between neuromodulation and proper function-specific processing, between bottom-up and top-down signalling, that it may confuse excitation and inhibition and, ultimately, that the magnitude of the BOLD signal does not accurately reflect differences between brain regions nor between tasks within the same regions (Logothetis, 2008), except for very simple paradigms (*e.g.* eyes open *vs.* eyes closed). Despite its shortcomings, fMRI is a valuable tool to test hypotheses on the large-scale spontaneous activity of the brain *in vivo*, and influential reviews (Logothetis et al., 2001; Viswanathan and Freeman, 2007) and recent findings (Magri et al., 2012) illustrated that

increase in neural activity (as measured with EEG and LFP) is indeed related to the amplitude and timing of BOLD fluctuations.

The classical procedure adopted to measure ongoing task-independent activity using fMRI is that of asking subjects to lie still in the scanner and try not to focus on any particular thoughts, either fixating a cross on a screen or with eyes closed: this design is often referred to as resting-state fMRI (rs-fMRI). This procedure thus implies a definition of "rest" based on rather constant sensory stimulation, motor output, and cognitive effort during the awake state. Nonetheless, assuming that the above mentioned condition lacks of any kind of external or internal modulation is obviously not realistic, and in fact the intrinsically uncontrolled nature of resting-state fMRI experiments has raised some concern, as it could in fact mirror a wide range of contents and cognitive states (Christoff et al., 2009; Richiardi et al., 2011; Hurlburt et al., 2015).

Although purposeful mentation of the subjects may in fact contribute to the measured BOLD fluctuations, it is indeed unlikely that it represent their primary source: coherent activations between regions associated with specific behaviors have been observed even in absence of that behaviors (Biswal et al., 1995; Fox et al., 2005) and, as mentioned above, the overall pattern of ongoing activations found in rs-fMRI can be observed across subjects (Beckmann et al., 2005; Biswal et al., 2010), species (Liang et al., 2011; Lu et al., 2012), and even global states, such as during sleep (Horovitz et al., 2009) or anesthesia (Vincent et al., 2007).

In fact, according to recent findings that analyzed data from more than a thousand subjects, the activity measured in resting-state conditions appear to be characterized by a mixture of wakefulness and sleep, with the probability for the subject to fall asleep increasing with scan duration (Tagliazucchi and Laufs 2014, see Figure 1.12). Neglecting this observation could in fact undermine the validity of the findings of classic rs-fMRI, as proper wakefulness and sleep are characterized by distinct functional architectures that are indeed differentiable using currently available classifiers, based *e.g.* on support vector machines (Tagliazucchi et al., 2012).

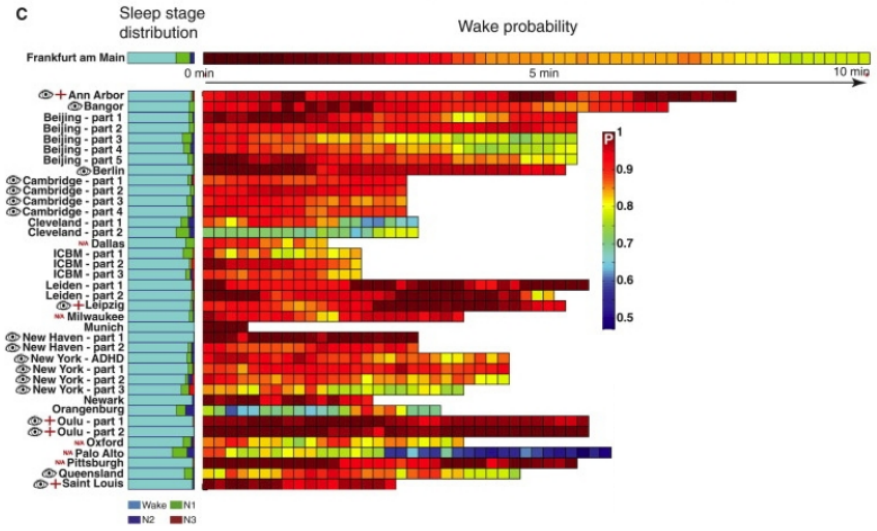

Figure 1.12: Probability to fall asleep increases with resting-state scan duration. Total time spent in the different NREM sleep stages (left) and wakefulness probability as a function of time (right). An eye next to the fMRI center name indicates an experiment with eyes open, an eye plus a cross indicates eyes open and fixation, and N/A indicates lack of data. Adapted from Tagliazucchi and Laufs 2014.

As such, the "resting-state" condition should be viewed as an arbitraty state mirroring potential differences in performance, task and vigilance.

The low frequency oscillations (<0.1 Hz) sampled by fMRI are vulnerable to possible confounds due to fluctuations in respiration and cardiac rate (Birn et al., 2006; Shmuel and Leopold, 2008; Murphy et al., 2013), that are typically regressed out jointly with other artifacts, like those due to subject motion (Van Dijk et al., 2012). Other methods used to remove physiological noise are that of excluding signals from regions more likely to display physiological artefacts, as for example those due to ventricles (Rombouts et al., 2003), using ICA to isolate components possibly due to non-neuronal sources (Beckmann et al., 2005), or regressing out the signal that is common to all voxels, referred to as *global sig-*

nal (Macey et al., 2004); note that it has been suggested that this last procedure can introduce artifactual negative correlations (Murphy et al., 2009). As such, it is important to acknowledge that fMRI has its own kind of inverse problem that, contrary to EEG and MEG, does not correspond to source localization, but consists in the proper *decomposition* of the processes underlying its generation and variation. In fact, a spontaneous increase (decrease) in the BOLD signal can never be unambigously attributed to a specific neural process, since regulation of blood flow can be determined by both genuinely neural as well as a number of other physiological mechanisms (Leopold and Maier, 2012). In a recent work, Glerean and colleagues pointed out that, according to the literature, the frequency band that seems to be the less prone to noise in human rs-fMRI is that between 0.04 and 0.07 Hz (Glerean et al. 2012, see Figure 1.13). Despite its many caveats, a considerable fraction of intrinsic BOLD signal variation appears to reflect genuine fluctuations of neuronal activations, characterized by reproducible spatial topography (Beckmann et al., 2005; Biswal et al., 2010) and coherent co-activations between regions showing some degree of similarity, both in terms of their anatomical connectivity pattern and of functionality (*i.e.* regions that are similarly modulated by different tasks, see Figure 1.14), thus making the study of BOLD spontaneous fluctuations especially relevant to try to elucidate the complex relationship between anatomy and functionality.

The vast majority of studies devoted to investigate coherent intrinsic fluctuations do so by computing the correlation of the BOLD signal measured in distinct brain regions, traditionally referred to as *functional connectivity* (FC). This term, first used to characterize the temporal coherence of trains of action potentials (Gerstein and Perkel, 1969), has been adopted to describe the correlation between spatially remote neurophysiological events, expressed as a deviation from statistical independence, and in principle independent from the particular measure or methodology used (Friston et al., 1993; Horwitz et al., 2005). The fundamental assumption behind this concept is that if two regions of the brain participate on the realization of a given operation (a

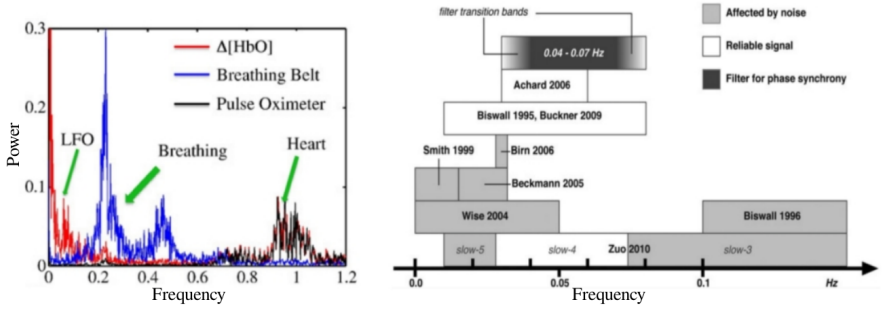

Figure 1.13: Frequency bands sampled in rs-fMRI. (Left) Power spectrum of oxygenation (Δ[HbO]), respiration and hearth pulsation obtained simultaneously with fMRI. Blood oxygenation was measured using near-infrared spectroscopy (NIRS). LFO, low-frequency oscilations. Adapted from Tong and Frederick 2010. (Right) Adapted from Glerean et al. 2012.

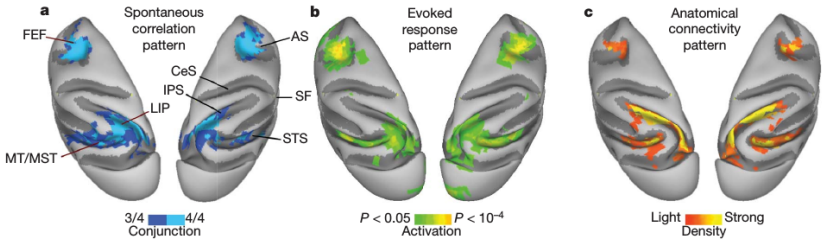

Figure 1.14: Intrinsic activity recapitulates task and anatomy. Coherent spontaneous BOLD fluctuations recapitulate activations observed during task and the underlying anatomical connectivity in the monkey. (a) BOLD correlations measured during anesthesia. (b) Activations evoked by a saccadic movement task. (c) Density of neurons labelled by retrograde tracer injections into right LIP. Reproduced from Vincent et al. 2007.

given "function"), then it is very likely that their activity will also correlate. This assumption is certainly legitimate, nonetheless it can also be misleading, as there is no guarantee of the contrary; measuring a correlation between two regions *does not* necessarily imply that this two regions are actually participating to the same operation (the same "function"): they may be just receiving similar perturbation patterns, either of neural or of non-neural origin. Furthermore, one cannote exclude that two regions contributing to the same function will exhibit weak correlation, as their coupling could be not captured by a simple linear measure. These caveats may be especially relevant when analyzing the coherence of intrinsic fluctuations, whose proper functional role is still not clear.

Despite many studies have already confirmed the high inter-subject similarity between the overall correlation structure found using resting-state fMRI (see Section 1.1 above), and even its apparent ability to correctly identify individuals (Finn et al., 2015) and predict individual differences during performance (Tavor et al., 2016), a systematic analysis of the reproducibility and of the reliability of spontaneous BOLD correlations and resting-state networks has been addressed by relatively few studies; one in particular (Choe et al., 2015), focused on quantifying the consistency of functional networks, reported an high degree of stability at the level of RSN spatial maps (see Figure 1.15).

Nonetheless, individual correlation coefficients measured between different brain regions during rest are indeed only moderately reliable across subjects, as indicated by a mean intra-class coefficient (ICC) of ≈ 0.2 (Birn et al. 2013; Zuo and Xing 2014, Pannunzi et al., in preparation, see Figure 1.16), indicating that the overall test-retest consistency of the spontaneous covariation between individual pairs of regions is indeed rather low.

On the other hand, as we briefly reviewed, many studies have repeatadly reported reproducible spatial patterns of intrinsic coactivations. How is that possible for the two findings to co-exist? How can hemodynamic spontaneous correlations be highly reproducible (even across states and across species), and at the same

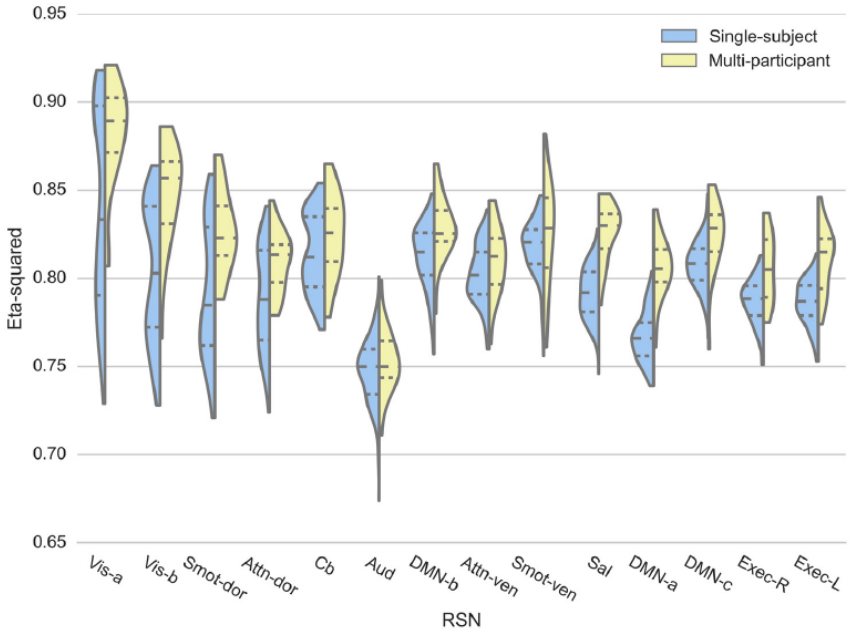

Figure 1.15: Reproducibility of RSN spatial maps. Spatial similarity of the RSN spatial maps to the corresponding group mean map, measured using eta-squared (η^2), a measure that can be used to quantify the similarity between images (0 indicates no similarity, whereas 1 indicates that they are identical). First, second and third quartiles are represented within the violin plots as dotted lines. Note that the seemingly counter-intuitive slightly larger mean similarity observed across many subjects is explained by the fact that the 14 RSNs used in the study were indeed derived from group-ICA, and as such it is by definition expected to observe large between-subjects similarity. Reproduced from Choe et al. 2015.

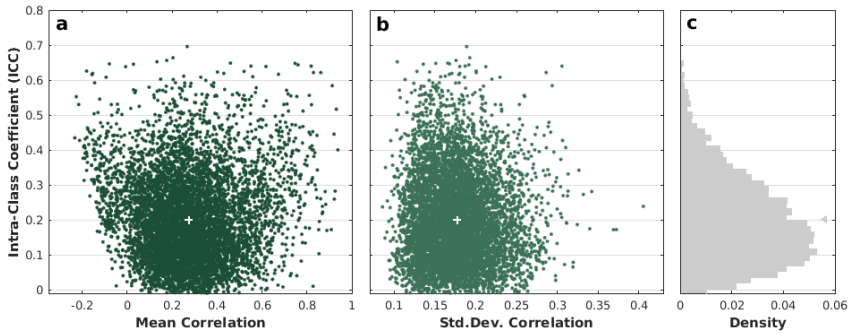

Figure 1.16: Reliability of resting-state correlations. We analyzed the reliability of correlation coefficients obtained in a classic resting-state fMRI study, finding that it is indeed rather low: this reflects the fact that the variability found across sessions for a given subject is very similar to the variability observed between different subjects. (a) Mean Pearson correlation coefficient *vs.* intra-class coefficient (ICC). (b) Standard deviation of the correlation coefficient *vs.* ICC. The white crosses in (a,b) mark the center of mass of the two bivariate distributions. (c) ICC distributions. The triangle on the right side of the panel indicates the mean ICC. Note that the reliability of the correlation between individual area pairs is practically independent from both the mean and the variance of each correlation coefficient. Adapted from Pannunzi et al., in preparation.

time so little reliable? There seem to be some sort of "scaling problem": in fact, the whole-brain functional maps (in the form of resting-state networks as well as the overall correlation structure) have been shown to be very consistent (Biswal et al. 2010; Choe et al. 2015, Pannunzi et al., in preparation), whereas the correlation values between single area pairs are, on average, little reliable (Birn et al. 2013; Zuo and Xing 2014, Pannunzi et al., in preparation).

A plausible -and not very surprising- explanation for the former observation can be that those consistent macroscopic functional structures, usually analyzed on a group-level, largely mirror the underlying anatomical organization -the basic plan- of the CNS (see Section 1.2.4, below).

On the other hand, it is possible that the poor reliability of the correlation between individual area pairs could be determined by the fact that the real pairwise covariation between brain areas is not a static object, but rather it is a processes exhibiting complex time-varying dynamics; such dynamic variability of BOLD intrinsic fluctuations would make estimates based on just a single (or just a few) scan(s) not representative of the entire process, thus dramatically affecting the reliability of the resulting correlations' estimates. As a consequence, we are analyzing (Pannunzi et al, in preparation) if the use of multiple scans could significantly increase the reliability of the estimated pairwise correlations, above and beyond estimates based on longer scans alone, as suggested by other studies (Birn et al., 2013; Power et al., 2011). In fact, increasing evidence suggests that the covariation between the intrinsic hemodynamics of different regions changes substantially over a period of minutes (Vedel Jensen and Thorarinsdottir, 2007). The time-varying fluctuations of BOLD pairwise correlations have been observed also in animal studies (Majeed et al., 2009; Thompson et al., 2013), and confirmed by comparing empirical spontaneous correlations with a stationary null model (Zalesky et al., 2014). The standard method used to analyze the time-varying pattern of spontaneous correlations is that of dividing the signal in overlapping sliding windows, and then compute the correlation between all brain regions within each sliding window (Allen et al., 2012). This simple method demonstrated that spontaneous BOLD fluctuations give rise to a repertoire of ever-changing subnetworks of correlated activity, thus unveiling the rich dynamics underlying intrinsic hemodynamic fluctuations (Hutchison et al., 2013).

1.2.3 Electrical and magnetic oscillations

It has been suggested that coherent activations of individual neurons and transient synchronization of neural assemblies should play a fundamental role in efficient information transmission (Fries, 2005; Womelsdorf et al., 2007), coordinating large-scale activity (Varela et al., 2001), as well as perceptual and cognitive binding (Singer, 1999; Engel et al., 2001); in addition, it is difficult to challenge the idea that neuronal representations, computations and higher-order cognitive processing should happen within the millisecond-to-seconds range, thus making a temporal resolution in this range of special interest. Tecnhiques such as electroencephalography (EEG), magnetoencephalography (MEG), electrocorticography (ECoG), local field potentials (LFPs) and voltage sensitive dyes (VSD) are between those tecnhiques that best suit this criterion. In addition, the non-invasivity of EEG and MEG allows them to be used on human subjects.

Activity of cortical neural masses displays oscillations at several frequancy bands, ranging from approximately 0.05 to 500 Hz and preserved in all mammalian species studied to date (Buzsáki et al. 2013, Figure 1.17).

Several studies have suggested that, within a given neural assembly, oscillations at neighboring frequencies tend to be associated with different states (Klimesch, 1999; Kopell et al., 2000; Engel and Singer, 2001). In addition, different rhythms can coexist (and even interact) within the same neuronal network (Steriade, 2001; Csicsvari et al., 2003). From a physical perspective, the $^1/_f$ power relationship typically observed between different frequency bands indicates that lower frequency components display proportionally larger amplitudes. This relationship also implies that any sufficient perturbation of the mechanisms underlying the generation of slower oscillations (*e.g.* changes in ions' concentration, hormones, neurotransmitters) can in principle cause a cascade of energy dissipation at higher frequencies (Bak et al., 1987), thus ultimately modulating fast-frequency activity (Sirota et al., 2003). In general, the period of the oscillation is determined by the size of the neuronal assembly engaged (Buzsáki and Draguhn, 2004): higher

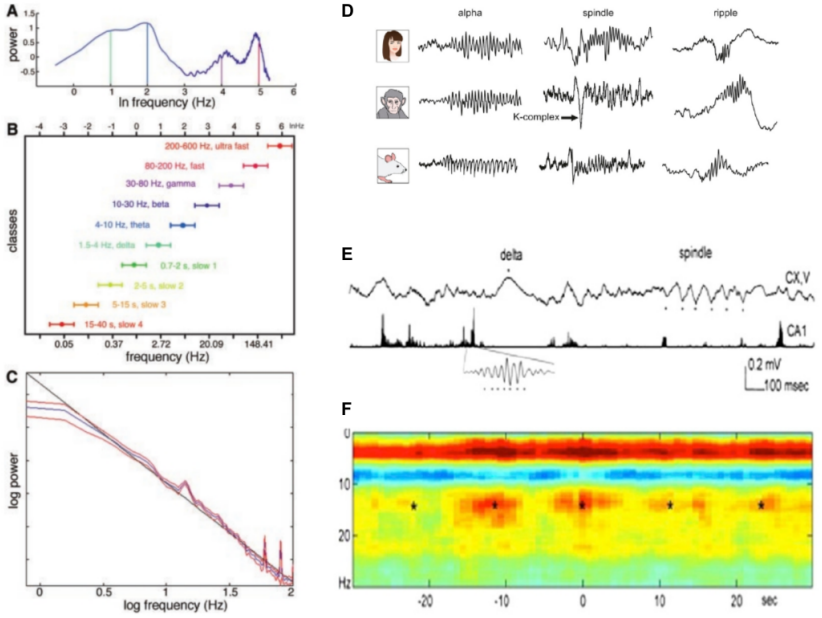

Figure 1.17: Overview of neural oscillations. (a) Power spectrum of hyppocampal EEG (note that the log-slope have been removed). (b) Classic frequency bands (log-scale). (c) Log-log power spectrum. (d) Illustrative examples of three types of oscillatory traces (α, spindles, ripples) in humans, monkeys and mice. (e) LFP from rat neocortex and filtered and rectified derivative traces from the rat's hippocampus, illustrating the emergence of "ripples". (f) Spectrogram of neocortical activity centered on hippocampal ripples. Note that ripple activity is modulated by the sleep spindles (as revealed by the power in the 10-18 Hz band), both events are modulated by the slow oscillation (strong red band at 0-3 Hz), and all three oscillations are biased by the phase of the ultraslow rhythm (approximately 0.1 Hz; asterisks). (a-c) reproduced from Buzsáki and Draguhn 2004, (d-f) adapted from Buzsáki et al. 2013.

frequencies are thus confined to small pools, whereas slower oscillations mirror the recruitment of large networks (Steriade, 2001; Csicsvari et al., 2003).

To date, many studies have analyzed in detail the relationships between neuronal oscillations (measured either with EEG, ECoG, MEG or LFPs) and intrinsic fluctuations of the BOLD signal. In order to search for potential electrophysiological correlates of BOLD fluctuations, one has first to identify corresponding neural processes that vary over the same time scale. One candidate is given by slow (<4 Hz) cortical potentials (SCP, Birbaumer et al. 1990; He and Raichle 2009), that can be measured either from intracortical or surface electrodes. Other frequency components are too fast to be directly compared with the much slower hemodynamic fluctuations, but they indeed exhibit slow power modulation, that can be captured and thus more meaningfully compared with BOLD activity (Leopold and Maier, 2012): the resulting time-varying signals are referred to as band-limited power (BLP) fluctuations. In 2001, Logothetis and colleagues (Logothetis et al., 2001) demostrated that BOLD signal changes positively correlated with fluctuations of the LFP signal around the electrode; later, Shmuel and Leopold (Shmuel and Leopold, 2008) simultaneosuly recorded BOLD and intra-cortical activity in the visual cortex of anesthetized monkeys, confirming that BOLD fluctuations correlated with BLP fluctuations in the γ band. Interestingly, a study on healthy human subjects highlighted the presence of positive correlation between the power of EEG oscillations at 17-23 Hz and the hemodynamic fluctuations within areas belonging to the default-mode network (Laufs et al., 2003). Finally, a large body of studies demonstrated that the power of LFPs signal in the α and low γ frequency bands conveys information about the timing and the amplitude of the BOLD signal (Kayser et al., 2004; Niessing et al., 2005; Schlvinck et al., 2010; Pan et al., 2011; Magri et al., 2012).

In Liu et al. (2010), the authors demonstrated that the temporal correlation between intrinsic oscillations measured with MEG during rest and during light sleep demonstrated slow (<0.1 Hz) spontaneous power modulations that synchronized over distant

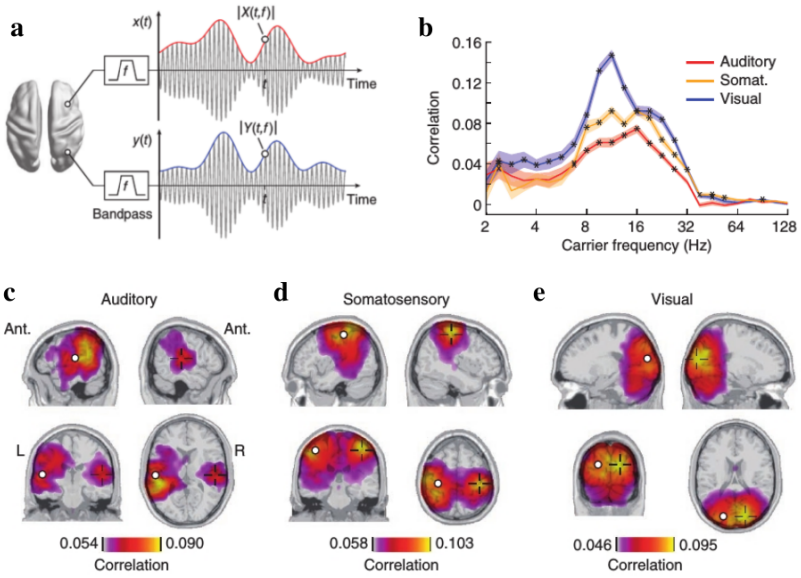

Figure 1.18: Power envelope correlations Power envelope (BLP) correlations between homologous sensory areas. (a) Illustration of the time-varying power envelopes of two source locations. (b) BLP correlations for different frequencies between homologous cortices. (c-e) Spatial distribution of the BLP correlation between auditory (c), somatosensory (d) and visual (e) cortices. White circles indicate the reference site, whereas the cross the mirrored location in the other hemisphere. Panels adapted from Hipp et al. 2012.

areas, in particular between homologous controlateral regions. In a seminal paper, Hipp and colleagues (Hipp et al., 2012) used the power envelopes of different narrow frequency bands obtained from MEG to characterize the large-scale correlation structure of spontaneous cortical activity in 43 healthy subjects (Figure 1.18).

In particular, the authors showed that the strongest correlations between band-limited power envelopes were those between 8 to 32 Hz (α to β range). BLP correlations between regions residing in the medial temporal lobes were strongest in the θ range (4-6 Hz), whereas correlations between sensorimotor areas tended to occur at higher frequencies (namely within low-γ, 32-45 Hz).

1.2.4 Anatomical Connectivity

> "To extend our understanding of neural function to the most complex human physiological and psychological activities, it is essential that we first generate a clear and accurate view of the structure of the relevant centers, and of the human brain itself, so that the basic plan - the overview - can be grasped in the blink of an eye."
>
> Santiago Ramón y Cajal

The previous sections dealt with some of the most commonly used methodologies adopted to study brain spontaneous activity and co-activations. Nonetheless, it is well-known that intrinsic inter-areal correlations, both locally and at a larger scale, appear to be fundamentally shaped and sustained by the underlying anatomical structure determining the overall connectivity profiles of neural ensembles (see Appendix A). As such, we will review some of the techniques used to capture the structural architecture of the central nervous system (CNS), a fundamental step in order to understand the emerging pattern of intrinsic co-activations discussed so far.

The importance of characterizing the connectivity among individual neurons and neuronal populations have been at the center of the work of eminent neuroanatomists, who made major contributions in our understanding of the tight link between anatomical and functional organization of the CNS (Ramón y Cajal, 1909; Swanson, 2012).

The classical methods used to track the neural fibers connecting different neurons (called *axons*) usually involved highly invasive tecnhiques such as chemical staining of individual cells with horseradish peroxidase (van der Want et al., 1997). This tecnhiques are only suitable for use either on slices of tissue, or in living animals that have next to be sacrificed, and are also very time- and computation-demanding. One of the most extensive

work was done on the macaque brain, leading to the creation of a large-scale map of its connectivity (the CoCoMac database, Stephan et al. 2001; Kötter 2004) Recent advances have brought to the creation of tecnhiques with an unprecedented resolution, such as CLARITY (Chung and Deisseroth, 2013; Chung et al., 2013) or the saturated reconstruction (Kasthuri et al., 2015), that however cannot be applied on living organisms (Figure 1.19).

The most common methods used to study anatomical connectivity *in vivo* build upon the capacity of MRI to record magnetic properties of different molecules, and apply this ability to track the bounded diffusion of water along the axons; as such it was proposed as a method to track neural fibers (Conturo et al., 1999; Bihan and Iima, 2015); nonetheless, the first implementation of this method, called diffusion tensor imaging (DTI), performed poorly in distinguishing complex wiring structures, leading to the development of more advanced methods such as diffusion spectrum and diffusion weighted imaging (DSI and DWI, respectively, Wedeen et al. 2005; Fillard et al. 2011, see Figure 1.20).

Diffusion tractography is a powerful tool, but presents some inherent limitations, the main one being that all current tractography methods tend to favor the shortest, straightest and simplest path between any two reference voxels (Jones 2010, see also Figure 1.21). From this simple fact stem the majority of the issues associated with fiber tracking, above all the consistent presence of both false positive and false negative reconstructed streamlines; in fact, it has repeatadly demonstrated that, even if highly reproducible, connectivity estimates obtained from tractography are not anatomically accurate, and as such should be taken with caution (Jones, 2010; Thomas et al., 2014; Jbabdi et al., 2015).

Another important issue related with this method lies in its interpretation. In fact, the number associated with a given reconstructed streamline does *not* correspond in any way with the probability of the detected fiber to exist, and does *not* directly mirror the real number of axons connecting two regions (Jones et al., 2013); this implies that one should not interpret it as an unambigous measure of connection strength.

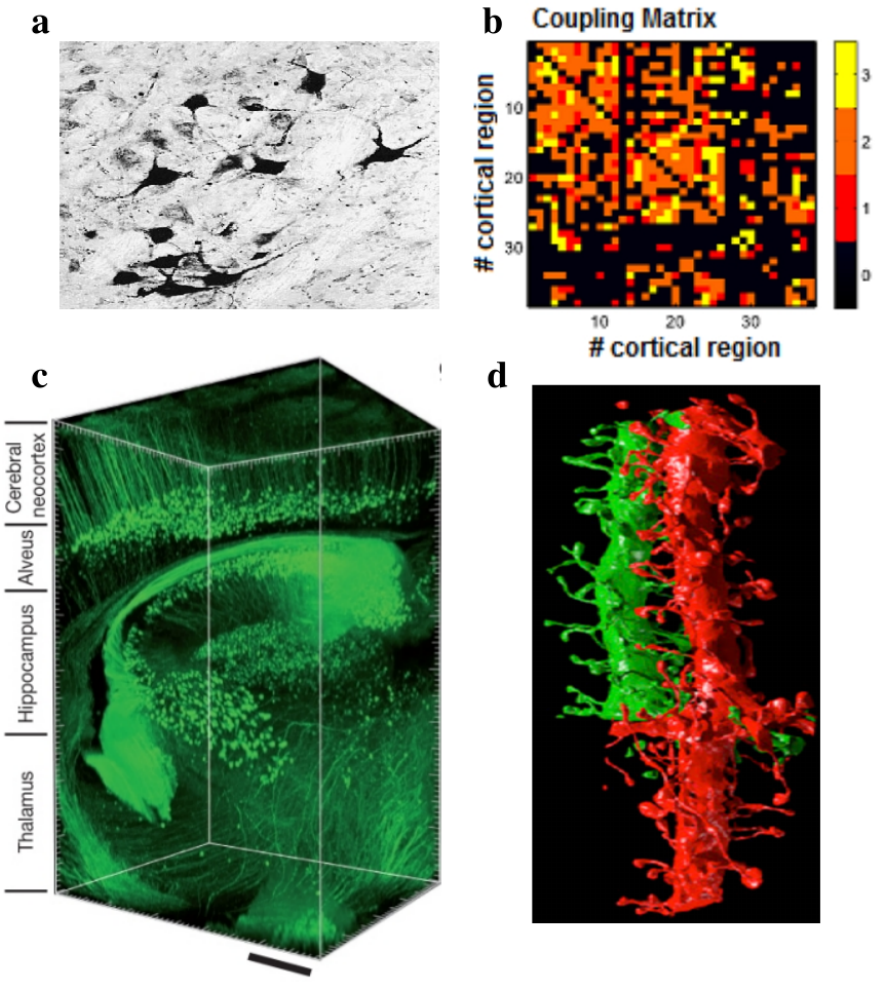

Figure 1.19: Tracking connectivity ex vivo. (a) Chemical staining (adapted from van der Want et al., 1997). (b) Directed coupling matrix obtained from CoCoMac database. Connection are classified as weak (1), medium (2) and strong (3). (c) CLARITY applied on non-sectioned mouse brain tissue (adapted from Chung et al 2013). (d) Saturated reconstruction of two dendrites and their synaptic buttons (adapted from Kasthuri et al. 2015).

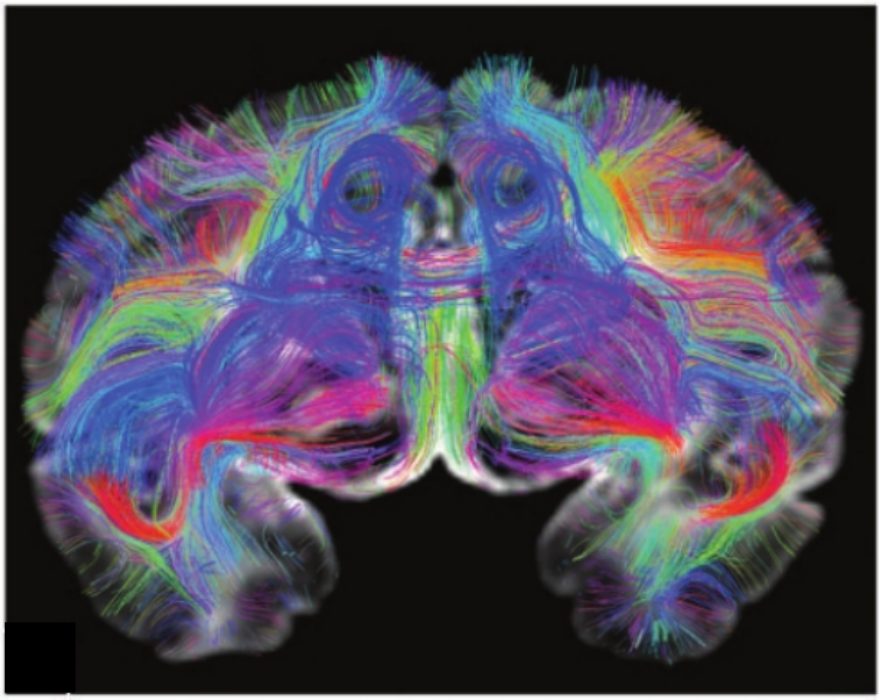

Figure 1.20: Diffusion Spectrum Imaging. Coronal cross section of the fibers detected using DSI on a monkey brain. Each fiber is coloured according to the orientation vector between its end-points. Adapted from Schmahmann et al. 2007

Different studies have compared the performance of diffusion-based imaging and invasive techniques based on injections of retrograde tracers, showing that, despite a small positive relationship, diffusion tractography is indeed, in general, not very accurate (van den Heuvel et al. 2015, see Figure 1.22).

Nonetheless, findings obtained from the comparison between DSI and histological tract-tracing on monkeys (Schmahmann et al., 2007) have definitively confirmed that diffusion tractography is indeed able to truly detect important axonal association pathways (see Figure 1.23). It is however worth to mention that these observations are not in contrast with the known limitations cited above: in fact, the 10 bundles of fibers correctly detected using DSI all are made of a large number of axons and have a rather

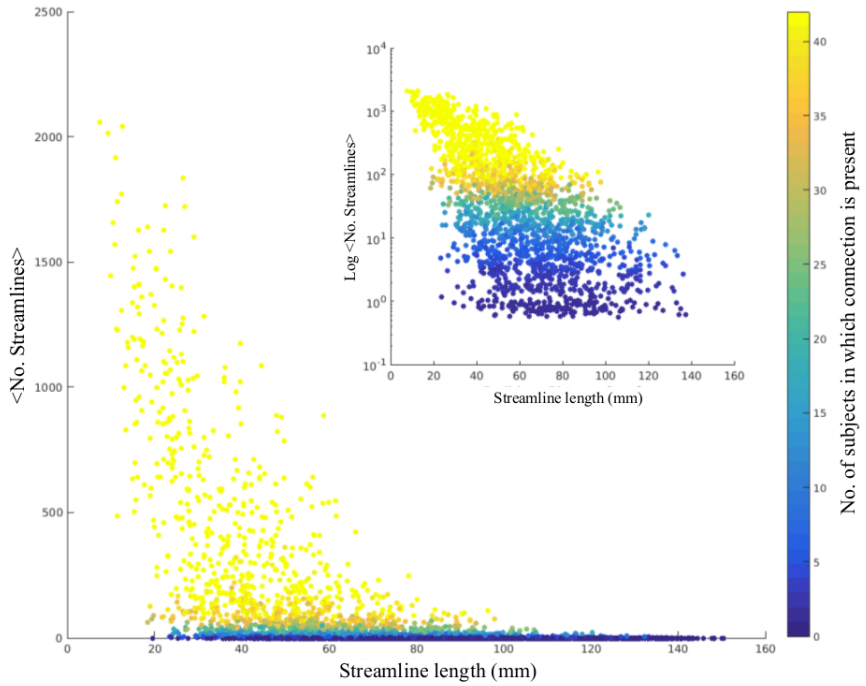

Figure 1.21: Tractography is affected by distance. We analyzed the relationship between the length and the number of reconstructed streamlines between 116 ROIs in 42 structural connectivity matrices obtained from DWI on healthy subjects, and computed the prevalence, across scans, of each reconstructed streamline, corresponding to the total number of scans in which it was detected (color coded in the panel). The figure well illustrates the tendency of tractography to favor shorter paths, as the number of reconstructed streamlines is larger for short distances, that are also the streamlines more frequently detected across scans. Remember that the number of reconstructed streamlines does not necessarily reflect the existence of a real bundle of axons (see text). It should be stressed that distance *per se* is *not* the primary cause behind this relationship, but it is rather a proxy for the inherent weakness of methods based on diffusion tractography in coping with paths that are not straight nor simple (Jones, 2010), features whose probability tend indeed to increase with distance. Adapted from Zamora-López et al., in preparation.

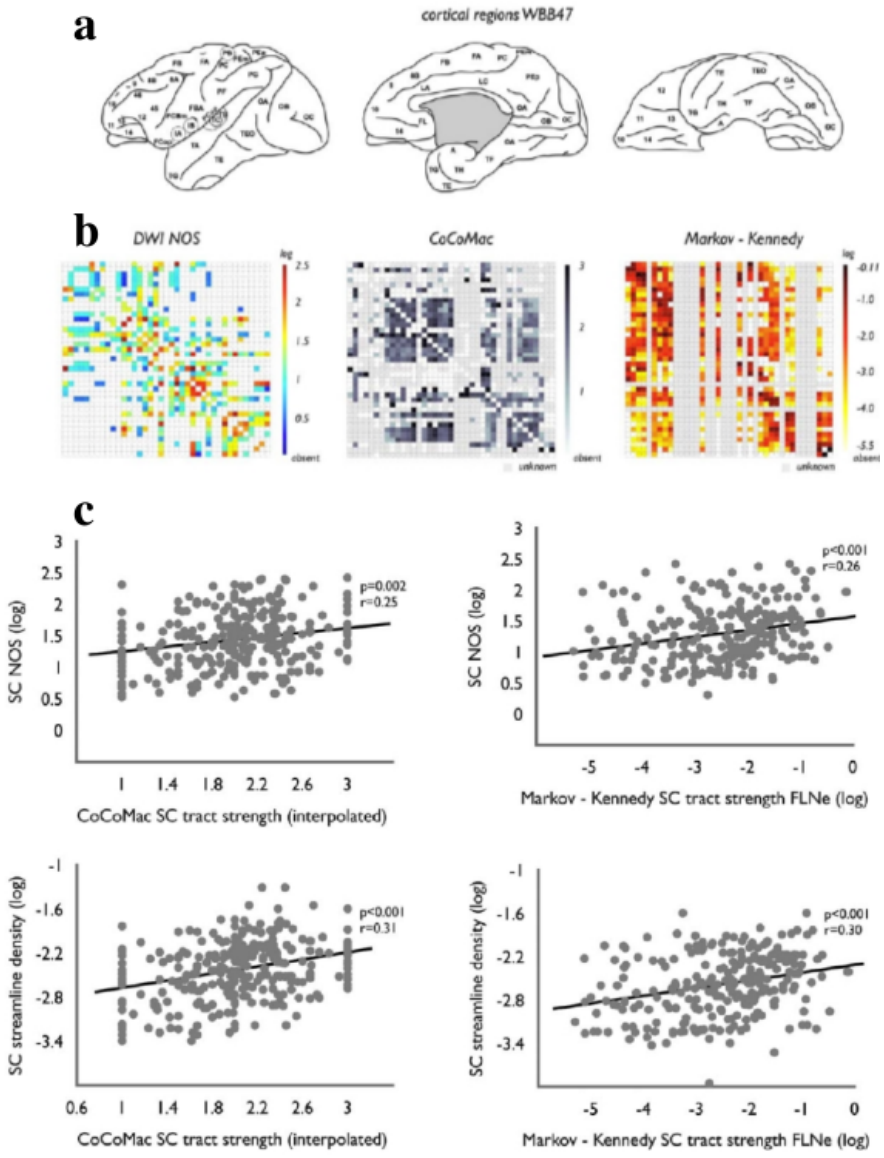

Figure 1.22: Comparison between tractography and tract-tracing. (a) 39 Cortical regions of the macaque atlas. (b) Connectivity matrix obtained from three datasets. DWI NOS, number of reconstructed streamlines using diffusion weighted imaging. The middle and right matrices are obtained using invasive and anatomically accurate tract-tracing methods. (c) Comparison of the three datasets. Panels adapted from van den Heuvel et al. 2015.

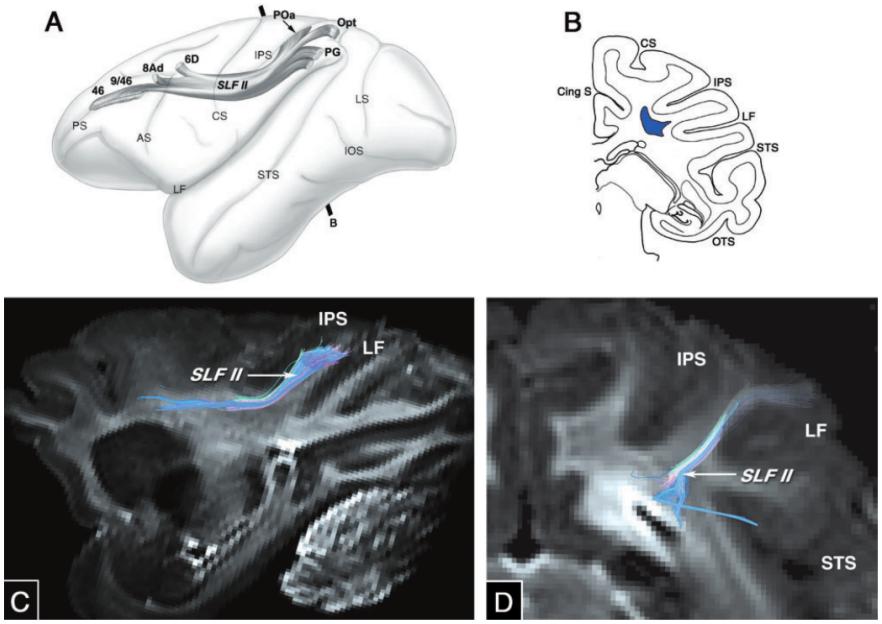

Figure 1.23: Tractography can detect important pathways. Illustrations of the second subcomponent of the superior longitudinal fasciculus (SLF II) of the rhesus monkey as determined with autoradiography (A,B) and DSI (C,D). Reproduced from Schmahmann et al. 2007.

straight and very simple orientations, thus making them easier to detect using diffusion tractography.

Indeed, it has been showed (van den Heuvel et al., 2009) that diffusion tractography can in fact reconstruct wide bundles of streamlines connecting areas belonging to different resting-state networks, and that the reconstructed fibers corresponded to existing axonal pathways (see Figure 1.24).

These encouraging result suggest that *in vivo* tractography can in fact be informative of at least some of the most dense fibers connecting even distant parts of the brain, and as such can thus be used to capture parts of the anatomical backbone underlying brain functionality.

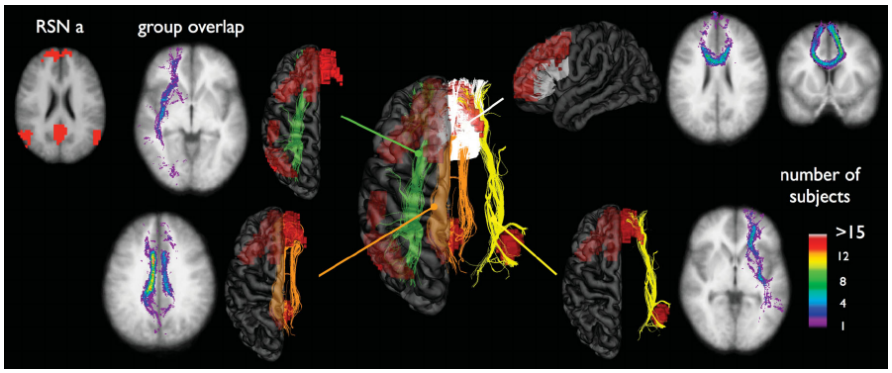

Figure 1.24: Reconstructed pathways underlying DMN. A subset of wide bundles of fibers connect remote brain regions whose spontaneous fluctuations tend to exhibit consistent temporal correlations in humans: due to their coherent collective activations during rest, and deactivations during many tasks, this set of areas have been referred to as "default-mode network" (Raichle et al. 2001, see Section 1.1 above). The corresponding anatomical fibers are the cingulum (orange), the left and right superior frontal-occipital fasciculus (green and yellow, respectively), and the genu of the corpus callosum (light grey). The color code correspondd to the number of subjects (n=26) in which the streamline was reconstructed after DTI. Adapted from van den Heuvel et al. 2009.

1.3 Brain Networks

> "All the organs of an animal form a single system, the parts of which hang together, and act and react upone one another; and no modifications can appear in one part without bringing about corresponding modifications in all the rest."
>
> George Cuvier (1789)

> "I have never had reason, up to now, to give up the concept which I have always stressed, that nerve cells, instead of working individually, act together, [...] through whole bundles of fibres. [...] However opposed it may seem to the popular tendency to individualize the elements, I cannot abandon the idea of a unitary action of the nervous system, without bothering if, by that, I approach old conceptions."
>
> Camillo Golgi (Nobel lecture, 1906)

At the end of the 19th century, Camillo Golgi and Santiago Ramón y Cajal proposed two different interpretations about the basic organization of the nervous system: Cajal argued that individual neurons should be its structural units, whereas Golgi believed in what he called "reticular" organization, which stated that neurons where all part of a single, continuous network. The so-called "neuron doctrine" proposed by Cajal was endorsed and strengthened by Charles Sherrington, who suggested that individual neurons were not only the structural units of the nervous system, but also its functional ones (Sherrington, 1906). Later discoveries (Porter et al., 1945) proved Cajal's hypothesis right: neurons were

indeed structurally separated units, as demonstrated by the existence of synaptic clefts (Palay, 1956). Nonetheless, after decades of striking discoveries and technological advances, the idea that individual neurons alone are alse the true, unique functional units of the brain is being refined.

It is certainly true that single neurons integrate incoming stimuli in very complex manners (Yuste, 2011), but on the other hand, individual neurons disconnected from one another have no possibility to perform complex functions such as proper pattern recognition, pretty much as a single gut cell alone cannot account for the whole digestive function. Furthermore, increasing evidences are suggesting that the complete connectivity profile of individual neurons are responsible for the actual function it exhibits (Song et al., 2014), and that changes in such connectivity are associated with changes in function (Newton and Sur, 2005; Majewska and Sur, 2006; Cheetham et al., 2008; Barnes and Finnerty, 2010). Single neurons are the structural building blocks of the nervous system, whose functionality is however determined by distributed processing carried by large ensembles of neurons (Hebb, 1949; Churchland and Sejnowski, 1994; Buzsáki, 2010; Izquierdo and Beer, 2013; Yuste, 2015).

As any other complex system, the brain can in fact legitimately be considered a network of interconnected and interacting elements, referred to as *nodes* (or *vertices*). The nodes of the brain web can either be individual neurons, larger populations or vast regions of the CNS, depending on the focus of the analysis and on the adopted techniques; the structural connections between these elements can thus be single synapses as well as wide bundles of axonal fibers (see Section 1.2.4 above), whereas the functional interactions between the activity of the elements can be summarized using any measure of pairwise co-variation (see Figure 1.25).

Over the last years, the analysis of brain structure and function as complex networks led to the emergence of a fertile new field of study, usually referred to as "connectomic" (Bullmore and Sporns, 2009; Hagmann et al., 2010; Sporns, 2014). It has been observed that anatomical brain networks, analogously to other

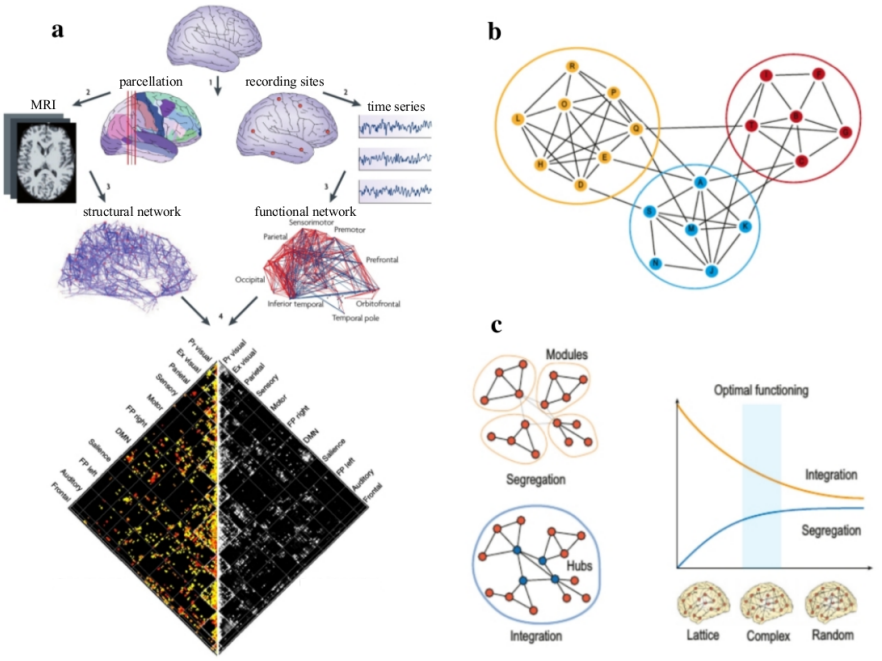

Figure 1.25: Analyzing brain networks. (a) Classic pipeline used to analyze structural (left side) and functional (right side) brain networks from MRI. The information is in the end summarized in a matrix, defining either the presence (or the "strength") of anatomical connections between a given pair of regions, or their correlation. The resulting structural connectivity (SC) matrix is typically obtained from diffusion tractography (after some preprocessing steps such as normalization and symmetrization), whereas the so-called functional connectivity (FC) matrix is computed from BOLD time series. Adapted from Bullmore and Sporns 2009 and (Sporns, 2014). (b) Brain networks can also be visualized using spring-embedded diagrams. The three circles correspond to three different network modules. (c) Left: Analysis of the high-order organization of the network (its *topology*) can reveal the presence of segregated modules and integrative nodes, referred to as *hubs*. Right: it has been proposed that optimal brain functioning is achieved when balancing the levels of integration and segregation. Panels (b,c) adapted from Deco and Kringelbach 2014.

natural and artificial systems, tend to exhibit specific topological properties thought to optimize network resiliency (*i.e.* resistance after structural perturbations) and large-scale communication while minimizing the overall wiring length of the axonal fibers; in addition, abnormal alterations of some of these topological properties have been linked with neuropsychiatric disorders (see Bullmore and Sporns 2012 for an extensive review).

As any other tool, graph measures have some limitations, some of them due to the fundamental arbitrariness encounterd when defining nodes and links in a network, other to the resolution of experimental measurements, or even to the theoretical metrics itselves, which may by definition be imperfect or computationally very expansive (Fornito et al., 2013; Sporns, 2014). Despite these challenges, the graph theoretic approach has revealed to be an extremely powerful framework to analyze and understand the intrinsic complexity of brain organization, and significant advances of both graph theory and of the technologies for sampling brain anatomical and functional organization promise to offer valuable knowledge in the future. For the interested reader, we reviewed some of the most important graph measures used to quantify topological properties of brain structural and functional networks in Appendix C.

In the last decades, great effort has been put to characterize the relationship between brain structure and function (Honey et al., 2009; Zhou et al., 2007; Zamora-López et al., 2016), with the aim of understanding the interplay and the relative contributions that the topology of the anatomical network and the dynamics governing neural activity exert on the complex correlation structure of intrinsic brain activity. In the next chapters, we will see how modulating global dynamics -through the use of anesthetic agents- and analyzing in detail the contribution of different network topologies could lead to a better understanding of their relative impact in shaping the overall spontaneous brain activity consistently observed in humans and other species.

Chapter 2

Modulating dynamics through anesthesia

"There is no better high than discovery."

E. O. Wilson

The organization of the central nervous system gives rise to a variegated range of possible activity patterns, constrained by the complex anatomical fabric and intimately moulded by the underlying physiology. Different regimes of neural activity are the physical substrate of the different behavioral and cognitive states that organisms exhibit. These global states can reflect physiological fluctuations triggered by the system's response to changes in the environment or by biological needs (such as conscious wakefulness or the different stages of sleep), or can result from non-physiological, abnormal or pathological factors (for example anesthesia, confusional states, mood disorders, coma). In all cases, changes in the overall activity regimes are determined by changes in some aspects of cellular function, *i.e.* in the microscopic or local dynamics.

In the present chapter, we will analyze how experimental manipulation of local dynamics, achieved using an anesthetic agent,

triggers significant changes in the arising functional structure, and how the progressive vanishing of the anesthetic effect corresponds to a gradual restoration of the organized spontaneous activity seen during the awake state. The chapter reproduces, with minor modifications, a paper published by Bettinardi et al. (2015).

2.1 Summary

Intrinsic brain activity is characterized by the presence of highly structured networks of correlated fluctuations between different regions of the brain. Such networks encompass different functions, whose properties are known to be modulated by the ongoing global brain state and are altered in several neurobiological disorders. In the present study, we induced a deep state of anesthesia in rats by means of a ketamine/medetomidine peritoneal injection, and analyzed the time course of the correlation between the brain activity in different areas while anesthesia spontaneously decreased over time. We compared results separately obtained from fMRI and local field potentials (LFP) under the same anesthesia protocol, finding that while most profound phases of anesthesia can be described by overall sparse connectivity, stereotypical activity and poor functional integration, during lighter states different frequency-specific functional networks emerge, endowing the gradual restoration of structured large-scale activity seen during rest. Noteworthy, our in vivo results show that those areas belonging to the same functional network (the Default-Mode) exhibited sustained correlated oscillations around 10 Hz throughout the protocol, suggesting the presence of a specific functional backbone that is preserved even during deeper phases of anesthesia. Finally, the overall pattern of results obtained from both imaging and in vivo-recordings suggests that the progressive emergence from deep anesthesia is reflected by a corresponding gradual increase of organized correlated oscillations across the cortex.

2.2 Introduction

The intrinsic complexity of brain organization allows the emergence of a wide range of different activity regimes, referred to as brain states. Ongoing brain activity during waking rest exhibits spontaneous dynamics that are characterized by highly structured patterns of correlated fluctuations known as Resting State Networks (RSN, Biswal et al. 1995; Greicius et al. 2003; Fox et al. 2005; Beckmann et al. 2005; Deco et al. 2011; Cabral et al. 2014a). In recent years, a growing number of studies have indicated the differences in spontaneous dynamics underlying different brain states, as during sleep (Horovitz et al., 2008; Larson-Prior et al., 2011), anesthesia (Kaisti et al., 2002; Boveroux et al., 2010), meditation (Brewer et al., 2011; Hasenkamp and Barsalou, 2012; Tang et al., 2012), psychedelic states (Vollenweider and Kometer, 2010; Carhart-Harris et al., 2012), and also at different states of brain development (Fransson et al. 2007; 2009). Ongoing activity observed during anesthesia and light sedation (Greicius et al., 2008; Stamatakis et al., 2010) shows intriguing similarities with slow-wave sleep (Horovitz et al., 2009). Moreover, it has been proposed that many mechanisms underlying anesthesia-induced loss of consciousness are also implicated in the fading of consciousness characterizing the descent to sleep (Franks, 2008; Brown et al., 2010). Many authors have investigated RSN in animals under general anesthesia (Lu et al., 2007; Pawela et al., 2008; Hutchison et al., 2010; Liu et al., 2011; Tu et al., 2011) and during wakefulness (Zhang et al., 2010; Liang et al., 2011), revealing the existence of intrinsic brain networks in primates (Mantini et al., 2011) and rodents (Becerra et al., 2011; Lu et al., 2012). The results obtained so far suggest that deeper stages of anesthesia tend to be characterized by diminished functional connectivity (Lu et al., 2007; Williams et al., 2010; Wang et al., 2011), and that the nature of such decrease is related to the anesthetic agent used (Pawela et al., 2008; Liu et al., 2011). Nonetheless, the modulation of large-scale connectivity during the spontaneous fading from a deep state of anesthesia to a lighter one is still unclear. Investigations of brain states have largely relied on the region-specific metabolic demands related to neural activity, which is at the ba-

sis of imaging techniques such as positron-emission tomography (PET, Raichle 1983) and functional magnetic resonance imaging (fMRI, Ogawa et al. 1992; Ogawa and Sung 2007), characterized by high spatial accuracy but limited temporal resolution. The application of high temporal resolution techniques such as electroencephalography (EEG), magnetoencephalography (MEG), electrocorticography (ECoG) and intracortical recordings such as local field potentials (LFP) have been crucial to elucidate the finer temporal structure of brain activity, revealing that different global states are linked to specific rhythms in humans and animals (Steriade et al., 1996; Buzsáki and Draguhn, 2004; Buzsaki, 2006). A significant portion of brain structural architecture is phylogenetically conserved in vertebrates (Striedter, 2004), with fundamental similarities among mammals (Hofman, 1989). This inter-species similarity in anatomical connectivity gives rise to the emergence of comparable patterns of organized activity, usually referred to as functional networks (for a review see Park and Friston 2013). The primary objective of this paper is to investigate how different brain states consistently modulate network functionality in the rat, both at the macroscopic (fMRI) and mesoscopic (LFP) scale, and by beans of comparing the connectivity between areas pertaining to the same or different network. Our results confirmed that different states of anesthesia are mirrored by broad changes in the underlying functional organization that occurs at different spatio-temporal levels, and that the state-related emergence of large-scale functional networks is sustained by interareal correlated oscillations at specific frequencies. Additionally, our findings suggest the existence of a frequency-specific association between correlated activity as measured with fMRI and LFP.

2.3 Materials and Methods

2.3.1 Animal preparation

Animals were deeply anesthetized by intraperitoneal injection of ketamine (60 mg/kg) and medetomidine (0.5 mg/Kg). Brain activity was recorded from the deepest phase of anesthesia up to

partial recovery. Descent and full recovery were not recorded, as they are experimentally demanding stages that often lead to artifacts. We excluded the possibility of recording full emergence from anesthesia also because the animal was not chronically implanted. The animals were continuously monitored by controlling the respiratory pattern in imaging and the heart rate during in vivo experiments. The animals were not paralyzed and the hind paw reflexes were regularly tested during electrophysiological recordings (see below). Atropine (0.05mg/kg) was injected subcutaneously to prevent secretions. Body temperature was maintained at 37C using a water-circulating heating pump (T/Pump, Gaymar, USA). Animal age, sex, weight and body fat are factors known to modify the anesthesia metabolism, thus animals were selected that exhibited similar characteristics (all adult Wistar males, 293 43g). All the procedures were carried out in compliance with the European Community Council Directive for the care and use of laboratory animals (86/609/ECC) and with the Generalitat de Catalunyas authorization (DOGC 2450 7/8/1997, Comite tico de Experimentacin Animal, Universidad de Barcelona).

2.3.2 fMRI recordings

MRI experiments were conducted on a 7.0 T BioSpec 70/30 horizontal animal scanner (BrukerBioSpin, Ettlingen, Germany), equipped with a 12 cm inner diameter actively shielded gradient system (400 mT/m). The receiver coil was a phased-array surface coil for the rat brain. Each anesthetized animal (n = 5) was placed in the prone position in a Plexiglas holder with a nose cone for administering a mixture of 30% O2 and 70% N2, and were fixed using a tooth bar, ear bars and adhesive tape. The animals were not paralyzed during the procedure. Tripilot scans were used to ensure the accurate positioning of the animal's head in the isocenter of the magnet. Echo planar imaging (EPI) sequence started 40 minutes after anesthesia induction and was continuously acquired over a period of around 2.3 hours with the following conditions: echo time (TE) = 50ms, repetition time (TR) = 3 s, field of view (FOV) = 25.6 x 25.6 x 7 mm, matrix size = 64 x 64 x 7 pixels,

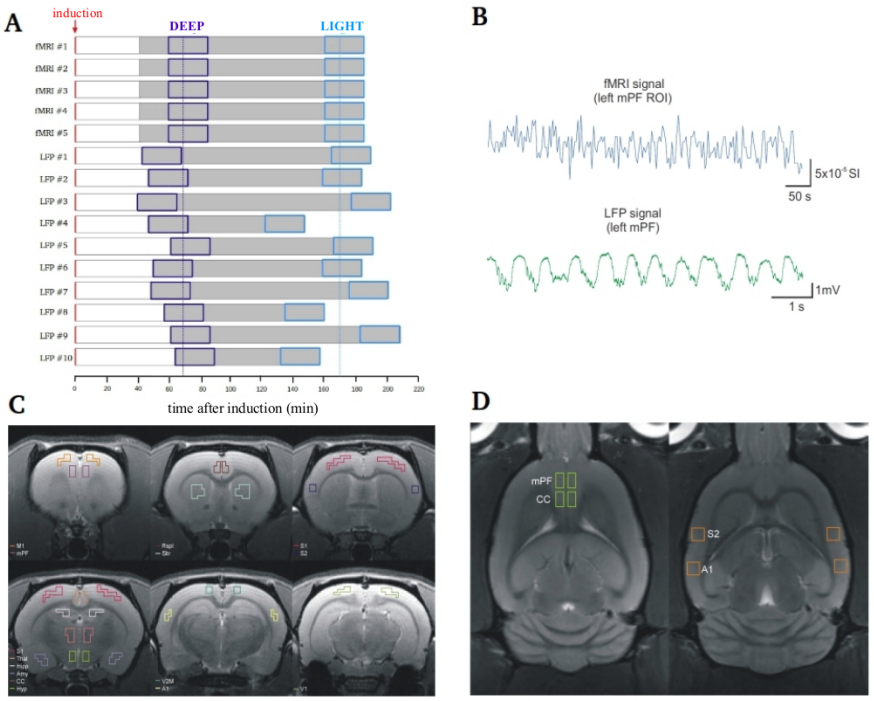

Figure 2.1: Experimental Protocol and recorded areas. (A) Schematic representation of the experimental protocol used in fMRI and LFP experiments (see Materials and Methods, 2.3). The red arrow indicates the moment of anesthesia induction, whereas the recorded intervals are highlighted in gray. Dark and light blue boxes indicate the intervals used as representative of deep and light anesthesia, respectively (see Identification of intervals corresponding to deeper and lighter states of anesthesia). Overall (fMRI and LFP), deep intervals were centered at 65.4 9.2 (mean SD) minutes, whereas light intervals were centered at 171 17.7 minutes after induction, as indicated by the dark and light blue dotted lines.(B) Examples of BOLD (Blood Oxygen Level-Dependent, blue) and extracellular local field potential (LFP, green) of the activity in medial prefrontal cortex (mPF). (C) Regions of interest (ROIs) used for BOLD signal extraction in imaging experiments.(D) Regions that were selected for LFP. MPF = medial prefrontal cortex; CC = cingulate cortex; S2 = secundary somatosensory cortex; A1 = primary auditory cortex.

resulting in a spatial resolution of 0.4 x 0.4 x 1 mm. Additionally, for recording purposes a T2 weighted anatomical image was acquired by using a RARE (Rapid Acquisition with Refocusing Echoes) sequence and the following parameters: TE = 11 ms, TR = 1.6 s, and same FOV, matrix size and spatial resolution as above. We obtained 7 coronal slices 2 mm thick. The resulting images were then treated in order to obtain the maximum number of isolated brain areas. Consequently, a given number of regions of interest (ROIs) were then obtained from each rat. Images were not treated for motion correction, as they presented stable positioning and alignment along the entire experiment. The selection of ROIs and corresponding spatial normalization was performed by comparing MRI images with a rat-brain atlas (Paxinos and Watson, 2004), taking into account the following criteria: first, the selected areas had to contain at least four voxels per image, but in no case could those in the limit of the area contain borders of brain or cortex or confounding limits between areas; secondly, the area had to be present in at least 80% of the voxels. The reference slices were the ones presenting medial prefrontal cortex area in the rostral side, the one presenting primary visual cortex (V1) in the caudal side, and one central slice where the hippocampal structures were identified. The intermediate slices were treated taking these previous three as a reference and identifying structures such as hippocampal formation, ventricles and corpus callosum as well as different subcortical structures. These two criteria limited the number of ROIs, which in every animal was the maximum number of regions that satisfied these objectives. Those criteria allowed the extraction of BOLD (Blood Oxygen Level Dependent) signal from 14 ROIs from each hemisphere, leading to a total of 28 ROIs in each of the 5 animals. The extracted ROIs were the primary motor cortex (M1), primary and secondary somatosensory cortices (S1, S2), primary and secondary visual cortices (V1, V2M), primary auditory cortex (A1), medial prefrontal cortex (mPF), retrosplenial cortex (Rspl), cingulate cortex (CC), thalamus (Thal), striatum (Str), amygdala (Amy), hippocampus (Hipp) and hypothalamus (Hyp). ROIs and average BOLD signals were extracted with homemade scripts implemented in Matlab (Mathworks, Natick, MA, USA). In order to

discard physiological ultra-slow fluctuations of the BOLD signal (Yan et al., 2009), while maintaining those that had been previously shown to be relevant for sampling low-frequency rat brain functional networks (Hutchison et al., 2010), we removed the best-fitting linear trend from the BOLD traces and band-passed them at 0.01-0.1 Hz. Obtained signals were then standardized.

2.3.3 In vivo LFP recordings

Lidocaine was administered at all pressure points and incisions prior to surgery. Approximately 30 minutes after induction, while the anesthesia was deepest, craniotomies were performed to record from the left medial Prefrontal cortex (mPF, 3.2mm AP, 0.8mm ML) and left and right cingulate cortex (CC, +1mm AP, +0.8mm ML) in 10 rats, and to record from the left primary auditory cortex (A1, -5.2mm AP, +6.5mm ML) and the left and right secondary somatosensory cortex (S2, -1.3mm AP, +5.6mm ML) in 6 animals. All coordinates are relative to bregma (following Paxinos and Watson 2006; see Figure 2.1). Extracellular slow-wave recordings were obtained with tungsten electrodes of impedances of 12 MΩ (as in Ruiz-Mejias et al. 2011). Electrodes were placed in infragranular layers (3mm deep in mPF, 2.4 mm in CC, 2.4 mm in A1 and 3.4 mm in S2). Recordings were amplified with a multichannel system (Multichannel Systems, Germany) and the signal was digitized and acquired at 10 KHz with a CED acquisition board and Spike2 software (Cambridge Electronic Design, UK). Local field potentials of the selected cortical areas were simultaneously recorded in the anesthetized rat, using the same anesthesia protocol as in imaging experiments. Extracellular recordings started 49 ± 9 (mean ± SD) minutes after induction (depending on the time needed for surgery) and continued until the animal exhibited weak withdrawal reflex after hind paw pinch. Recordings before and after hind paw stimulation were discarded to avoid artifacts, resulting in a total duration of LFP recordings of 135 ± 26 (mean ± SD) minutes. Obtained signals were down-sampled offline to 333 Hz, and a notch filter was then applied in order to remove 50 Hz electrical noise. At the end of the experiment the animals were administered a lethal dose of sodium pentobarbital

(800mg/kg).

2.3.4 fMRI data analysis

Preprocessed BOLD signal was divided in 90% overlapping sliding windows of 10 minutes (corresponding to 200 sample points each), each one shifting one minute in time with respect to the previous one. Indeed, in all the plots where the x-axis represents the time course of a given measure, the labels on the x-axis indicate the first minute of the 10-minutes sliding window used to compute the corresponding measure, unless otherwise stated. The use of sliding windows to evaluate time-varying changes in brain activity and connectivity have been successfully reported in some recent works, both on humans and on anesthetized animals (Keilholz et al., 2012; Hutchison et al., 2013; Thompson et al., 2013). BOLD signal variability over time of each individual ROI was evaluated computing the variance of the preprocessed time-series in each sliding window, whereupon the mean BOLD variability was calculated as the mean variance of each sliding window across all areas. The results were then averaged across rats. According to Friston and colleagues (Friston et al., 1993), functional connectivity (FC) was calculated using pairwise Pearson's correlation between each pair of areas of each sliding window. Since the sampling distribution of the Pearson's correlation coefficients is known to be non-normal, the values were converted to their corresponding Fisher's z-scores in order to be properly compared (Fisher, 1915). The mean correlation time course was then computed averaging all the 378 traces ($\frac{28\times(28-1)}{2}$) obtained from all area pairs. Similarly, we calculated the distribution of the correlation coefficients (and its standard deviation) in each sliding window. We then computed, for each sliding window, the mean Kuramoto order parameter χ, a measure that describes the degree of overall network synchronization in a system of coupled oscillators (Kuramoto 1975, see Supplemental Methods B). This measure quantifies the uniformity of the phases across all the nodes in the network at a given time, ranging from 0 for a fully incoherent network state and 1 for a fully synchronized one. In order to promote efficient information processing, the

outputs of different and highly specialized computations have to be coordinated and integrated into distributed but coherent neural activity. In the present work, we were interested in evaluating if the ability of the brain to integrate information across distant regions changed during the gradual fading of anesthetic effect. We can define functional integration as the transient binding of information across brain regions, a phenomenon that can be measured from the overall structure of correlations between areas in a given temporal window. To this aim we applied, on the correlation matrix obtained from each sliding window, a measure of functional integration based on the size of the largest connected component (see description below), thus obtaining a picture of the time-varying changes in functional integration taking place over the course of anesthesia. First, we binarized the Pearson's correlation matrix obtained from each 10-minute sliding window by applying a threshold T ranging from 0 to 1 with subsequent steps of 0.01 and following the criterion that if $|r_{ij}| <$ we set 0, and 1 otherwise. Thus for each sliding window we obtained as many binarized adjacency matrices $A_{ij}(T)$ as the number of applied thresholds. We then calculated the size of the largest component of each $A_{ij}(T)$. In this framework, a network component is defined as a sub-network in which the edges of all its are connected to each other by paths, but are not connected to any additional vertex of the supergraph. The size of a network component is given by the total number of its vertices. The size of the (largest) component is thus a measure related to the (upper bound in the) amount of correlated activity that is integrated within a set of connected vertices. In order to get a measure independent of the threshold, we then integrated that curve within the range of the threshold between 0 and 1.

2.3.5 Deep and light anesthesia

Imaging measurements robustly indicated the presence of a continuous and non-monotonic progression over time from a stage characterized by low BOLD variability and weakly correlated activity to one marked by higher BOLD variability and stronger and more heterogeneously correlated fluctuations. According to this

pattern, we were able to take as representative of a deeper phase of anesthesia the 15 sliding windows starting 60 minutes after induction, whereas the last 15 windows were selected as representative of light anesthesia. The sliding windows used to calculate the changes of a given measure over time all had same length (10 minutes), which means that the intervals used to statistically compare the two phases of anesthesia were 25 minutes each, i.e. long enough to sample substantial and reliable differences between brain states. In contrast to fMRI, during LFP experiments the level of anesthesia could be more precisely assessed by checking the absence of the withdrawal reflex tested with hind paw pinch (see In vivo LFP recording). On average, LFP deep intervals were centered at 61.8 ± 10 (mean $\pm$ SD) minutes after induction, whereas the light ones spanned a larger range, 171.7 ± 22 minutes (see Figure 2.1). Henceforth, we will refer to the above mentioned intervals as deep and light anesthesia, respectively.

2.3.6 Coupled and uncoupled area pairs

We used the BOLD signal corresponding to the two anesthesia intervals to compute stationary functional connectivity matrices and the corresponding correlation distributions. Results were then Fisher transformed (see Results 2.4). For further analysis we focused only on the correlations between those pairs of areas that simultaneously satisfied two constraints in all five rats: First, r_{ij} had to be significantly different from zero (with $p < 0.05$); secondly, such correlation had to have comparable values across rats, *i.e.*, the standard deviation (SD) of its average across all rats had to be smaller than 1, which means a maximum standard error (SE) of 0.4, being the usual SE value for biological phenomena below this threshold. We referred to the obtain subset of area pairs as Robust Coupled Nodes (RCNs). Area pairs that didn't show correlation significantly different from zero either in deep and light intervals were considered "uncoupled".

2.3.7 Detection of functional communities

We computed the community structure of RCNs sparse matrices obtained from light anesthesia applying a version of Louvain's community-detection algorithm based on a modularity function for weighted networks (Blondel et al., 2008; Gómez et al., 2009), implemented in the Brain Connectivity Toolbox (Rubinov and Sporns, 2010). Modularity Q is a cost function (see Supplemental Methods B) used to optimize community detection. It evaluates the "goodness" of a partition by counting the total number of edges falling within groups compared to the expected number of edges that may fall within the groups in equivalent networks whereby edges are placed at random (thus preserving the total number of edges in each node). Modularity optimization leads to graphs partitioned into densely intraconnected groups of nodes (referred to as "communities"), which are sparsely connected between them. Modularity can thus be considered a measure of segregation. Louvain's community detection method is stochastic, and its results can vary from run to run. For this reason we ran the method 10,000 times for each sparse RCN network, and then defined the most probable community to which each area pair belonged as the community to which it was most often assigned over the 10,000 repetitions. The community structure computed on individual rats' light RCN matrices always returned the same community partition, indicating inter-subject consistency and confirming the reliability of the selected RCN. We thus isolated two areas (mPF and CC) that, according to our analysis, belonged to same functional community, and considered them as an example of coupled regions, i.e. brain areas whose activities are reliably connected as they take part to the the same functional network. In order to capture the overall changes in communities' structure taking place during the gradual fading of anesthesia from the individual to the group level, we first iterated 10,000 times the community detection algorithm on the full (28 x 28) FC matrix obtained from each sliding window of each animal, and then computed the a posteriori probability that each pair of ROIs had of belonging to the same community across all iterations and all animals in each sliding window. We thus calcu-

lated, for each one of the obtained probability matrices, the mean a posteriori probability of belonging to the same community, in order to obtain a rather simple summary of the overall changes in the structural stability of different communities over the course of anesthesia. After that, we measured functional segregation over time computing the modularity index Q from the FC matrix obtained from each sliding window, and then average results across animals.

2.3.8 LFP data analysis

In order to evaluate the frequency-specific coupling between coupled (mPF-CC) and uncoupled (A1-S2) regions in deep and light anesthesia, we computed the correlation between the power envelopes of homologous band-limited signals obtained from two different regions, to which we refer to as band-limited correlations (BLCs). BLCs can be seen as an extension of the classical Functional Connectivity (Friston et al., 1993) in the frequency domain and can be used to quantify the degree of co-variation between neuronal oscillations of two distant cortical regions at a given frequency (Brookes et al., 2011; Hipp et al., 2012; Cabral et al., 2014a). To this aim, the continuous down-sampled data was bandpassed in 100 non-overlapping frequency bands (1 Hz width) from 0 to 100 Hz. After having calculated the Hilbert envelopes of the 100 signals obtained for each area and having applied a squared-log transformation in order to ensure normality of the estimates (as done in Hipp et al. 2012), we band-passed the resulting envelopes at the same resolution used in our previous imaging experiments (0.01-0.1 Hz) and down-sampled them at 1 second to account for the low-frequency components of the oscillations classically sampled in fMRI experiments. Then, for each animal we computed the Pearson's correlation coefficient between the resulting signals from each homologous frequency band between pairs of areas and converted it into the corresponding Fisher's z-score, resulting in 100 correlation values for coupled and uncoupled areas (one per frequency band). We then computed the difference between the BLCs of the two states (deep and light) for each 1 Hz-width frequency band for coupled and uncoupled area pairs (see

Supplemental Methods B). Subsequently, we divided the original preprocessed LFP signal in 90% overlapping windows of 10 minutes, as previously done for fMRI data. We then calculated BLCs in each sliding window. BLC time courses of the broader classical frequency bands were calculated analogously after having band-passed the preprocessed LFP signal according to the following frequency ranges: slow waves (0.01-1 Hz), low δ (1-2 Hz), high δ (2-4 Hz), θ (4-8 Hz), α (8-15 Hz), β (15-30 Hz), low γ (30-50 Hz) and high γ (50-100 Hz).

2.3.9 Frequency shift to higher frequencies

During BLC analysis we observed the presence of two shifts to higher frequencies in correlated oscillations during the gradual transition from deep to light anesthesia, the first shift around 1 Hz and the second around 10 Hz (see Results 2.4). To investigate this aspect, we computed the relative correlation in the two frequency bands of interest ($\sim$1Hz and $\sim$10 Hz) as the ratio between the higher and the lower component of a given frequency-band-of-interest over sliding windows for a given area pair (see Supplemental Methods B). This procedure quantifies how much the mean band-limited correlation in a given frequency range varies in relation to another frequency range, thus making it possible to measure their relative contributions in different intervals of time. Values greater than 1 indicate predominance of the higher frequency BLC component, whereas values smaller than one indicate the opposite (1 indicates perfect balance). For each animal, we calculated the relative correlation in deep and light intervals for the transition from <1 Hz to 1-2 Hz and that from 8-10 Hz to 11-15 Hz in both coupled ($n = 10$) and uncoupled ($n = 6$) areas, and then average across rats.

2.4 Results

2.4.1 Correlation increases as anesthesia fades away

We induced a state of deep anesthesia in rats and recorded brain activity while the level of anesthesia gradually decreased (see Materials and Methods 2.3; protocol scheme in Figure 2.1). Our first objective was to monitor BOLD signal changes over time that might correspond to different levels of anesthesia. To this aim, we first divided the continuous BOLD signals in 90% overlapping windows of 10 minutes and then analyzed, for each window, its variability for each region of interest (see Materials and Methods). Supplementary figure S1A illustrates the variance of the BOLD signal of each single ROI, whereas the average across all areas is depicted in Figure 2.2A. We observed a certain degree of heterogeneity depending on the ROI, but we also observed an overall increase in BOLD variability as the effect of anesthesia diminished in time. We then analyzed the time-varying changes of BOLD pairwise correlations over the entire duration of the protocol (see Materials and Methods 2.3) and obtained, for each time window, the value of the correlations between different regions (referred to as Functional Connectivity (FC); Friston et al. 1993) and their average across all area pairs. We observed the footprint of a progressive modulation between different brain conditions, being characterized by a first drop of the correlations (due to the gradual descent toward deeper stages of anesthesia) followed by a gradual increase toward the end of the recording (see Figure 2.2B and B.1B in Supplementary Material). As not all regions seemed to exhibit comparable correlation time courses, we also focused on the changes in pairwise correlation between the BOLD signal of each individual region and all other regions over sliding windows. This procedure gave us insights on the different functional connectivity pattern displayed by single cortical and subcortical areas as the effects of anesthesia gradually fade out over time (see examples of individual FC time courses of cortical and subcortical ROIs in Figures B.2 and B.3 in Supplementary Material). A complementary way to characterize the ongoing changes in FC across

all brain areas is to focus on the variability in the distribution of all correlation coefficients over time (Figure 2.2C and B.1C in Supplementary Material). We observed a change in the distribution of correlations, marked by a gradual spread toward higher positive values and a corresponding increase in its standard deviation (SD) as the effects of anesthesia diminished over time. All the obtained time-varying results showed a consistent tendency to increase over time, suggesting the presence of a modulation in the transition from deep towards light anesthesia. One plausible explanation for such a pattern of observations was that the shape of the underlying BOLD distribution changed over time according to the level of anesthesia. To check for this possibility, we took as representative four ROIs whose BOLD signals showed the highest correlation during the light period (mPF and CC, bilaterally) and then compared the corresponding BOLD distributions obtained from the two levels of anesthesia. The distribution of the signal in the two periods had comparable shape, confirming the possibility to rule-out a spurious origin of the observed pattern of findings. We thus tested whether BOLD variance, pairwise correlation and its standard deviation were significantly different in the two intervals taken as representative of deep and light anesthesia. The mean values of both levels demonstrated that the light interval was characterized by higher values in all measures, being the pairwise correlation the most significant (BOLD variance: $p = 0.0466$; pairwise correlation: $p = 0.0088$; standard deviation of the correlation distribution: $p = 0.0375$, one-sided paired t-tests, $n = 5$). These results confirmed that deep anesthesia largely reduces brain functional connectivity, which is in turn gradually restored as the effect of anesthesia vanishes over time. Another evidence of the presence of distinguishable brain conditions was obtained measuring and comparing the degree of overall network synchronization in the mentioned intervals. We investigated this aspect by calculating the Kuramoto global order parameter (see Materials and Methods 2.3), a measure that has been widely applied in neuroscience to investigate synchronization at different scales (Maistrenko et al., 2007; Cumin and Unsworth, 2007; Cabral et al., 2011). Our results indicate that intrinsic BOLD fluctuations transiently synchronize across many

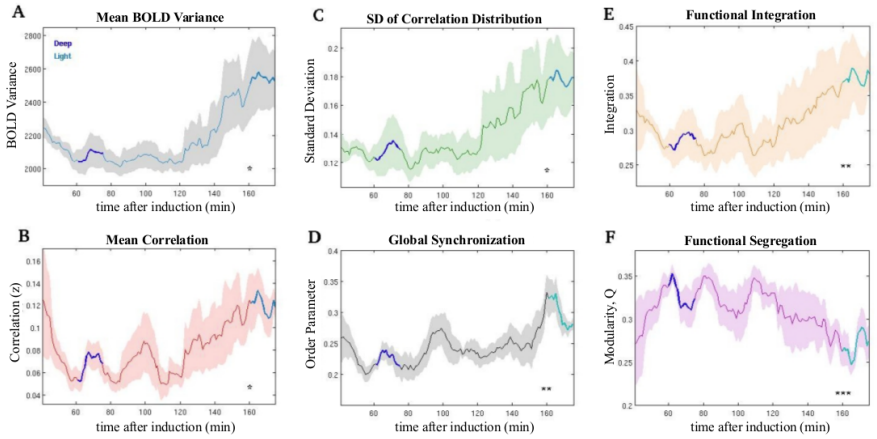

Figure 2.2: Fading of anesthesia associated with changes in brain activity. (A) Time course of the mean BOLD variance across all areas confirms that decreasing levels of anesthesia are mirrored by increased BOLD variability. (B) Mean correlation over time computed over all area pairs. (C) Standard deviation (SD) of the correlation distribution over time. (D) Mean global synchronization (Kuramoto order parameter,) over time. Not surprisingly, this metric resembles the mean correlation across all areas, suggesting that the level of anesthesia modulates the overall network's ability to synchronize. (E) Functional integration over time. (F) Change of modularity (Q) over time. Modularity is a measure of functional segregation and, as expected, follows an opposite behavior compared to functional integration (see Materials and Methods and Discussion). Dark- and light-blue lines superimposed over the time courses represent the intervals selected for statistical comparison of the mean values between deep and light anesthesia, respectively, and shaded areas indicate standard error of the mean (SEM). Deep and light intervals were statistically different for all measures (* indicates $p < 0.05$, ** stays for $p < 0.01$ and *** $p < 0.001$; see Results 2.4).

ROIs either in deeper and lighter phases of anesthesia, nonetheless the mean synchronization during light was significantly higher than during deep anesthesia (with $p = 0.0038$, one-sided paired t-test, $n = 5$; see Figure 2.2D).

2.4.2 Functional integration and segregation

Our results show that both correlation and overall networks' synchronization are globally reduced in deeper state of anesthesia. To further investigate the state-related changes in overall network properties, we quantified also functional integration and segregation (by means of the modularity index Q across different levels of anesthesia (see Materials and Methods 2.3). On one hand, we found that the progression from deep to light anesthesia implied a significant increase in functional integration, as shown when comparing the mean values obtained from the two intervals ($p = 0.0067$, one-sided paired t-test, $n = 5$; see Figure 2.2E); on the other side, each relative increase (decrease) in functional integration over time was mirrored by a corresponding decrease (increase) in modularity. In addition, mean modularity was found to be significantly reduced in light anesthesia compared to deep ($p = 0.00097$, one-sided paired t-test, $n = 5$; see Figure 2.2F). This pattern of finding is not unexpected, as the two indexes address complementary aspects of networks' organization: indeed, functional integration is related to the size of the largest connected component, whereas modularity, being a measure that quantifies network segregation, takes large values when a given graph can be partitioned in many scattered communities, which thus tend to be of relatively small size due to the finite size of the network.

2.4.3 Emergence of functional networks

FC matrices obtained from the two intervals showed distinct patterns and correlations' distributions, being the lighter period characterized by the presence of higher correlations and suggesting the emergence of structured patterns of brain activity (Figure 2.3A). Statistical comparison confirmed that the average distribution of correlation values in the two conditions was significantly different (with asymptotic $p = 7.5904 \cdot 10^{-15}$, Kolmogorov-Smirnov test). Due to the somewhat large variability among rats found in the correlation matrices of the light intervals, we selected only those area pairs that consistently showed robust correlations across subjects (RCNs; see Materials and Methods 2.3). Collectively, the

RCNs comprised less than 0.3% of all area pairs during deeper phases of anesthesia, indicating that the activity of the vast majority of areas during this state is generally less correlated with that of other areas, and less consistent across animals. Conversely, the number of RCNs showing consistent coupling between rats during lighter anesthesia was around 10% (Figure 2.3B). The connectivity pattern among RCNs obtained from light anesthesia suggests that segregated networks of connected nodes emerge as a consequence of the gradual fading of anesthetic effect. To check for this possibility, we calculated whether the resulting RCNs obtained during light anesthesia could actually be partitioned into distinct functional modules by applying a well known community-detection algorithm (see Materials and Methods 2.3). Consequently, five robust groups of functionally connected clusters of areas of different size were identified: The first RCN community comprised the first auditory and somatosensory areas (A1, S1), secondary visual cortex (V2M) and the retrosplenial cortex (Rspl); the second comprised primary visual (V1), medial prefrontal (mPF) and cingulate (CC) cortices; and the third was composed by the primary motor (M1) and the secondary somatosensory (S2) cortices. The thalamus (Thal) and the striatum (Str) appeared to form two distinct functional modules of contralateral areas (Figure 3C). The application of the same algorithm on the RCN found during deeper phases of anesthesia returned no community structure. In addition, the time-varying matrices of the pairwise a posteriori probability of pertaining to the same functional community (see Materials and Methods 2.3 and Figure 2.4) clearly indicate that the transition from deep to light anesthesia is marked by the gradual emergence of increasingly stabler patterns of structured activity. In fact, during deeper stages of anesthesia, the sets of community partitions that is possible to obtain across repetitions of the community detection algorithm are much less reliable, from the individual to the group level, than those obtained from light anesthesia. This indicates that deeper stages of anesthesia are dominated by a less structured pattern of co-activations than during lighter phases.

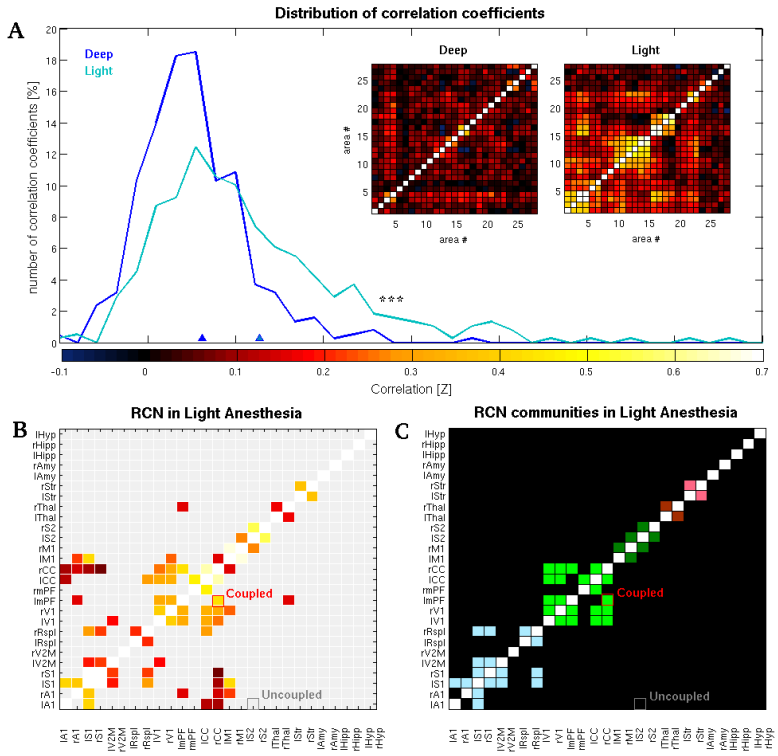

Figure 2.3: Different brain states are mirrored by different properties of the underlying functional networks. (A) Distribution of the correlation coefficients and corresponding average FC matrices obtained from deep and light intervals. The two distributions were statistically different (*** indicates $p < 0.001$, see Results). Dark- and light-blue triangles indicate the means of the deep and light distributions, respectively. (B) Average matrix of the Robust Coupled Nodes (RCNs; see Materials and Methods 2.3) obtained from light anesthesia. The color-code quantifies the average correlation coefficient of those area pairs that were classified as RCNs. Area pairs that were not classified as RCNs are highlighted in light gray. (C) Community structure of the light RCNs, where nodes of the same colors indicate areas belonging to the same community (see Materials and Methods 2.3). No community were detected in the deep anesthesia interval. In panels B and C, nodes that were selected as representative of coupled and uncoupled area pairs and used for further analysis are highlighted in red and gray, respectively.

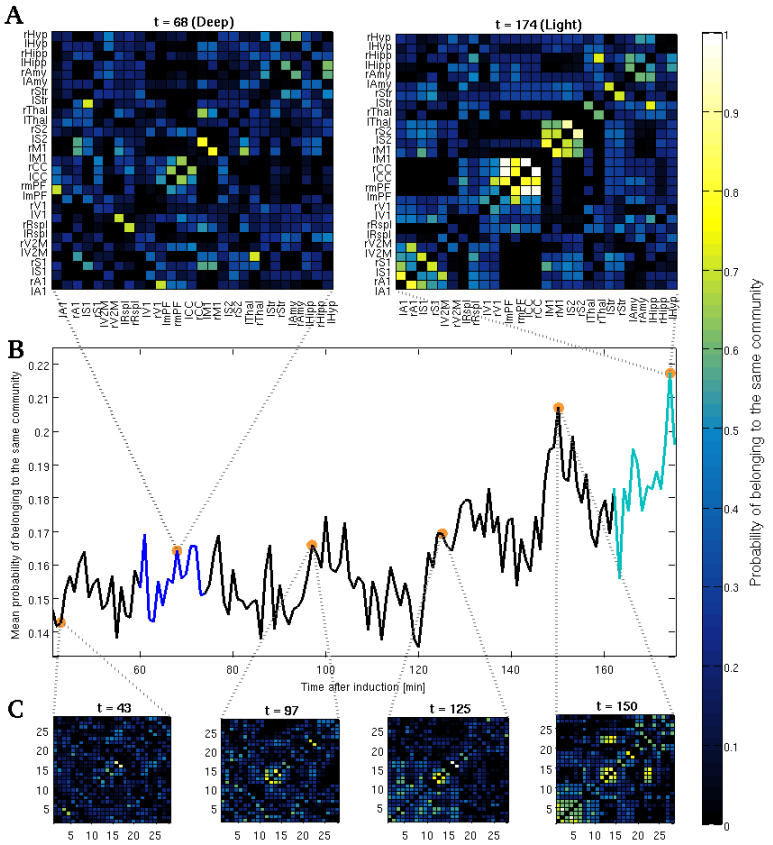

Figure 2.4: Networks' stability increases while anesthesia fades out. (A) Matrices of the ROIs pairwise a posteriori probability of belonging to the same functional community obtained from two sliding windows taken as representative of the deep (t = 68, left) and light (t = 174, right) anesthesia intervals. (B) Mean a posteriori probability of belonging to the same functional community over time. Superimposed dark- and light- blue lines indicate the deep and light anesthesia intervals, respectively. (C) Examples of the matrices of pairwise a posteriori probability that were used to compute the mean a posteriori probability depicted in panel B. During deeper phases of anesthesia the obtained community partitions are more variable both across iterations and animals, thus leading to sparser matrices and lower mean probabilities. Nonetheless, as the effects of anesthesia naturally decrease, BOLD fluctuations exhibit an increasing tendency to gradually stabilize in structured time-varying patterns of large-scale co-activations, as mirrored both by the increased mean probability of belonging to the same community as well as by the increasing consistency of the emerging communities. All a posteriori probabilities obtained for each sliding window were computed using all 10,000 iterations of the community detection algorithm over all animals (see Materials and Methods 2.3).

2.4.4 FC between areas of the same networks

We next focused on the correlation time courses of two subsets of area pairs: (1) those that were consistently and highly correlated across all rats (*i.e.*, were previously identified as RCNs; see above and Materials and Methods 2.3) during light anesthesia and, according to our community analysis, belonged to the same functional cluster (mPF and CC, henceforth referred to as coupled areas); and (2) those that showed no significant correlation ($p \geq 0.05$) across all rats in light and deep anesthesia (A1 and S2, referred to as "uncoupled" areas). It should be noted that mPF and CC have recently been identified as part of the rat's Default Mode Network (DMN, Lu et al. 2012). We analyzed the co-variation of the BOLD signals between the above mentioned ROIs including both ipsilateral and contralateral areas in order to control for possible differences in the co-activation pattern among areas belonging to the same or to the contralateral hemisphere. Comparisons of the mean correlation values obtained from deep and light intervals confirmed that there was no statistical difference between the two groups when considering uncoupled areas (A1-S2), whereas coupled ones (mPF-CC) showed a significant increase in correlation in the evolution from deep to light anesthesia (with $p = 0.0117$, one-sided paired t-test, $n = 5$, see Figure 2.6A). In addition, it is worth to mention that FC, functional integration and mean synchronization suggest clear associations between each other (see Figure Figure B.4 in Supplementary Material). This is not surprising when considering that, for example, some of them are actually functions of other ones, or that can reflect a common mechanism. Nonetheless, by definition each of these measures quantifies different (even if related) properties, thus the fact that they exhibit linear association does not necessarily imply that they carry the same information.

2.4.5 Frequency-specific changes in neural coupling

We thus selected the aforementioned coupled and uncoupled areas for further LFP recordings in order to determine the speci-

ficity of oscillatory patterns connecting distinct area pairs during the gradual fading of anesthesia. To that end we simultaneously recorded LFP from mPF, CC, A1 and S2 while using the same anesthesia protocol we had used in fMRI experiments. Comparison of the power spectra between deep and light intervals confirmed that ketamine-medetomidine anesthesia induced a modulation in the oscillatory activity. This modulation was characterized by a decrease in power at frequencies higher than 30 Hz in all areas and also by an increase in power in frequencies around α in mPF and CC ($p < 0.05$, paired t-test, see Figure B.4 in Supplementary Material). We then computed BLCs (see Materials and Methods 2.3) of the two different area pairs obtained from deep and light intervals and statistically compared the mean values within coupled (mPF-CC, $n = 10$) and uncoupled (A1-S2, $n = 6$) areas. Whereas for uncoupled areas the BLCs between different states differed only slightly, coupled areas showed a significant increase in BLCs during light anesthesia at different frequencies ($p < 0.05$, one-sided paired t-test, $n = 10$, see Figure 2.5A). This increase appeared selectively at 8-15 Hz and in the 30-50 Hz range. In addition to this, the non-overlap of the standard mean error intervals shows that coupled areas exhibit higher correlations than uncoupled ones in both anesthesia conditions continuously from 2 to 50 Hz (see Figure 2.5A). To further investigate this fact, we compared the correlations' distribution of coupled and uncoupled areas both during deep and light anesthesia for the two above-mentioned frequency ranges (8-15Hz and 30-50Hz), confirming that coupled areas showed significantly greater correlations in both comparisons (all $p<0.001$, Wilcoxon rank sum test , coupled $n = 10$, uncoupled $n = 6$). The frequency-specific increase from deep to light anesthesia seen in coupled areas became evident when the BLCs obtained during deep anesthesia were subtracted from that obtained during light anesthesia, as depicted in Figure 2.5B (see Materials and Methods 2.3). These findings not only demonstrate that areas belonging to the same functional network correlate at specific frequencies more than areas that do not participate in the same network even during deeper stages of anesthesia, but they also indicate that coupled areas exhibit a clear net increase in cou-

pling in these frequency ranges (8-15 Hz and 30-50 Hz) during the progression to lighter states of anesthesia. Subsequently, in order to analyze the evolution of neuronal coupling at different frequencies over time, we divided the original preprocessed LFP signal in sliding windows (as done for fMRI) and then computed the BLC in each window (see Materials and Methods 2.3). The resulting band-limited time courses confirmed that it is possible to distinguish between coupled and uncoupled nodes even during deeper phases of anesthesia, given that areas participating in the same network showed stronger correlations at approximately 10 Hz (see Figure 2.5C).

2.4.6 Shifts to higher frequencies

The evolution to light anesthesia in coupled areas was marked by a gradual shift toward higher frequencies of the correlation peaks at approximately 1 Hz, and another around 10 Hz. This fact prompted a more detailed investigation. We quantified these possible state-related shifts to higher frequencies calculating the relative correlation between higher and lower components of the frequency ranges of interest (see Materials and Methods 2.3). Statistical comparison of the mean relative BLCs in deep and light intervals showed that the shift from <1 Hz up to 2 Hz significantly accounted for the progression from deep to light anesthesia in both area pairs (coupled: $p = 1.7288 \cdot 10^{-8}$, $n = 10$; uncoupled: $p = 5.335 \cdot 10^{-9}$, $n = 6$; paired Wilcoxon signed rank test; see Figure 2.5D top). On the other hand, the increase in relative correlation from 8-10 to 11-15 Hz from deep to light anesthesia was significant only in areas that belonged to the same functional network (coupled: $p = 4.4988 \cdot 10^{-17}$, $n = 10$; uncoupled: $p = 0.8327$, $n = 6$; paired Wilcoxon signed rank test; see Figure 2.5D bottom). These findings suggest that the BLC shift from 8-10 to 11-15 Hz observed in the transition from deep to light anesthesia could be specific to areas participating in common functional networks.

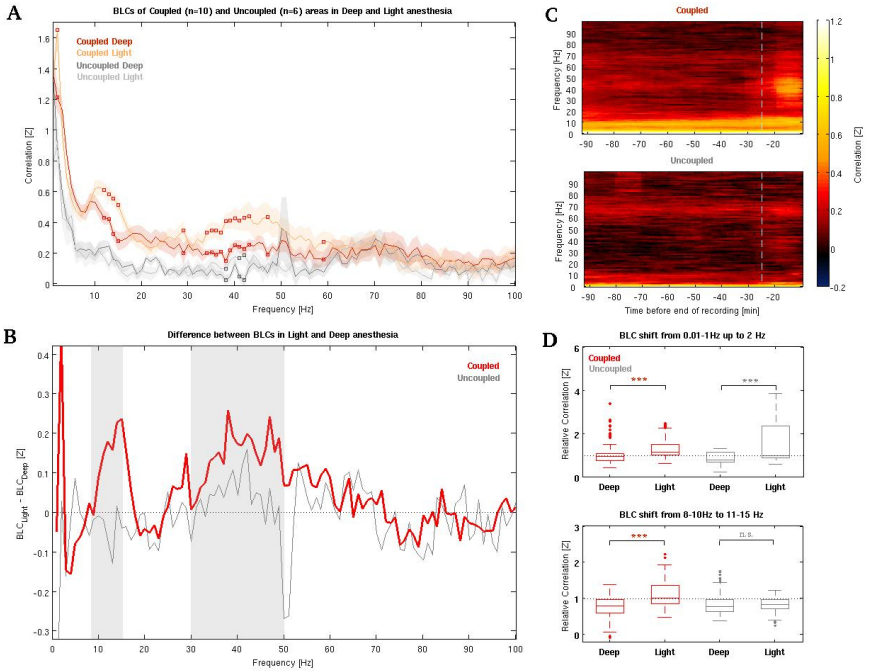

Figure 2.5: BLCs discriminate between network areas and different brain states. (A) Average BLCs obtained from the two sets of areas. Empty squares mark BLCs that exhibited significantly higher values in light anesthesia compared to deep anesthesia within coupled (red squares, n = 10) and within uncoupled (gray squares, n = 6) area pairs ($p<0.05$; see Results 2.4). (B) Difference between 1 Hz-width BLCs obtained in light and deep anesthesia intervals was calculated separately for coupled (red line, n = 10) and uncoupled (gray line, n = 6) area pairs (see Materials and Methods 2.3). (C) Average BLC time courses of the two pairs of areas (see Materials and Methods 2.3). Coupled areas (top) exhibit sustained correlations around 10 Hz that are preserved during all the recording session. These average BLC time courses are shown just for visualization purposes, as they resulted from individual recordings of slightly different length (see Materials and Methods 2.3). Averages have been obtained aligning each recording to its end point and equalizing it with respect to the shortest one. This procedure does not allow to show the actual deep interval that was used for statistical comparison for each recording (see Figure 2.1A). For this reason, only the onset of the 15-minute light interval is shown, being represented by a light-blue dashed line. (D) Quantification of the BLCs peak shift in the transition from deep to light anesthesia in coupled and uncoupled area pairs. Average relative correlations (see Materials and Methods 2.3) were statistically different in all cases except for the shift from 8-10 to 11-15 Hz in uncoupled areas. *** indicates $p < 0.001$, whereas n.s. Stands for 'non significant' (see Results 2.4).

2.4.7 Similarity of fMRI and LFP time courses

The obtained BLC time courses (Figure 2.5C) indicated that the progression to light anesthesia is characterized by an increase in correlation that is specific for the above-mentioned frequency ranges (8-15 Hz and 30-50 Hz), and can account for differences between areas belonging to the same or to different functional networks. Not surprisingly, statistical comparisons of the mean correlations of the BLC time courses obtained from both periods confirmed that only areas pertaining to the same functional network exhibit significant increase in correlations in the 8-15 Hz (α) and 30-50 Hz (low γ) bands during the transition from one state to the other as compared to other frequency bands (α band: $p = 0.0317$; low γ band: $p = 0.0287$; one-sided paired t-test, $n = 10$; see Figure 2.6B). Qualitative comparison of the BLC over time between all area pairs simultaneously recorded in LFP experiments and the corresponding FC time courses obtained from the same ROIs (mPF-CC and A1-S2) in imaging experiments outline the possible existence of a relationship between brain correlated fluctuations as measured with BOLD signal and coupled neural oscillation, especially in the γ range (see Figure 2.6 and Figure B.6 in the Supplementary Material).

2.5 Discussion

Neurons form relatively stable structural connections in the brain, but at the same time they participate in functional networks that change over time according to the brain state. Despite its relevance, few studies have focused on the ongoing changes between different brain states (Martuzzi et al., 2010; Tang et al., 2012; Lewis et al., 2012). To our knowledge, none has addressed this question by comparing measurements obtained with imaging techniques and intracortical recordings in order to investigate their consistency. The aim of the present work was to identify how the gradual evolution from deeper to lighter phases of anesthesia modulates the connectivity patterns between different areas at

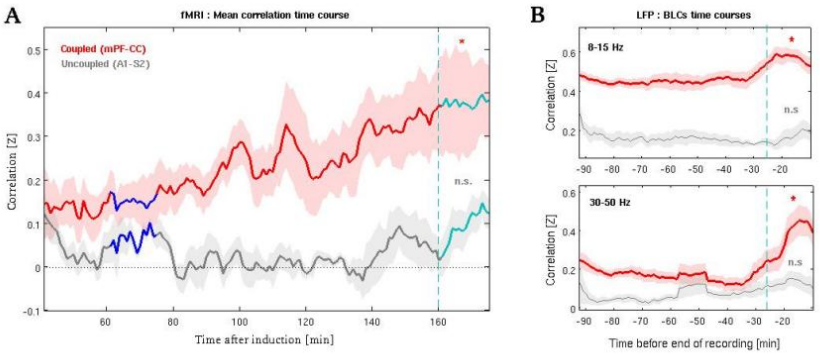

Figure 2.6: BOLD correlations and BLCs of specific frequency ranges exhibit comparable time courses. (A) Mean BOLD correlation time courses obtained averaging the activity of only those ROIs that were selected as being representative of areas that belong to the same (coupled, red) or to different (uncoupled, gray) functional networks (see Materials and Methods 2.3). (B) Examples of average BLCs time courses for two different frequency ranges for the two sets of area pairs (see Materials and Methods 2.3). Light-blue, dashed lines in panels A and B indicate the onset of the light interval, whereas * indicate significance ($p<0.05$) of the comparison deep versus light and n.s. indicates "not significant" (see Results 2.4). Due to the different duration of individual LFP recordings, deep intervals used for statistical comparisons are not shown in panels B (see legend of Figure 2.5).

the macro- (fMRI) and the mesoscopic (LFP) levels, and to determine whether such coupling motifs could distinguish between areas belonging to the same or to distinct functional networks. To that end, we compared results separately obtained with fMRI and LFP using a common experimental protocol. Having deeply anesthetized the animal, we recorded rat brain activity while the level of anesthesia progressively decreased over time.

As expected, our findings indicated that the induction of a deep state of anesthesia has dramatic effects on brain functionality. Indeed, the most profound phase of anesthesia is characterized by a significant reduction in the variability of intrinsic BOLD fluc-

tuations and their overall low-frequency synchronization. These phenomena can explain the observed weakening of long-range correlations between different regions and the transient breakdown of those differentiated networks that have previously been found in rats during light anesthesia (Pawela et al., 2008) and waking rest (Liang et al., 2011). Our findings are in agreement with the proposal that the induction of anesthesia is related with a reduction in the repertoire of distinguishable brain states (Alkire et al., 2008; Hudetz et al., 2014), as the decrease in variability of both the BOLD signal and the correlation distribution leads the system toward more uniform, stereotypical dynamics (Deco et al., 2009a). Spontaneous brain activity has been suggested to exhibits small-world network properties (Sporns and Zwi, 2004; Bassett and Bullmore, 2006), where a large number of densely clusterized local networks performing highly segregated computations are linked together by a relatively small number of connections, resulting in a complex structure of hierarchically nested networks (Meunier et al., 2010; Sporns, 2013). This complex architecture has been theoretically linked with efficient information processing and propagation, enabling to rapidly integrate the outputs from different specialized local networks (Watts and Strogatz, 1998; Latora and Marchiori, 2001). Our results suggest that during deeper stages of anesthesia these functional connections between communities get dramatically weakened. The resulting framework of scattered local connectivity is thus mirrored by an increase in functional segregation, and a corresponding reduction in integration. In this scenario, deep phases of anesthesia are characterized by a massive destructuration of the complex large-scale pattern of co-activations seen during light anesthesia (Keilholz et al., 2012; Lu et al., 2012) and waking rest (Zhang et al., 2010; Liang et al., 2011).

As the effect of anesthesia vanished, the coupling across distant brain regions is gradually restored, leading to the progressive flourishing of distinct functional networks, as was also indicated by the corresponding rise in functional integration. Taken together, these results indicated that the gradual emergence from anesthesia is marked by an increase in differentiated and struc-

tured large-scale brain activity. Indeed, during fading of anesthesia, intrinsic activity of different subsets of areas start to cluster, uncovering the presence of a non homogeneous correlation structure which reveals itself as the animal approach the wake state, and that likely reflects the progressive and dynamical emergence of different functional networks. After induction of a deep state of anesthesia, the precisely organized pattern of reliable coactivations that have been found to characterize resting brain activity undergo a dramatic reduction in their overall inter-areal synchronization, which in turn lead to the partial fragmentation of the large-scale brain networks into an highly variable mosaic of smaller clusters of areas exhibiting transients of weakly correlated activity.

It should be emphasized that even if small correlation coefficients indicate weaker statistical dependence, it does not mean that the vast anesthetic-induced net decrease in pairwise correlation would simply result in pure random brain activations: deeper stages of anesthesia seem to be rather described by a more volatile scenario where small subsets of areas belonging to common networks show reduced correlated fluctuations of the BOLD signal and present decreased probability of exhibit collective correlated oscillations, which in turn could explain the transitory breakdown of large-scale functional networks. Our *in vivo* results support this view, as they provide evidences for the preserved presence, even during profound phases of anesthesia, of a functional backbone consisting of highly correlated oscillations in the band that maintained linked to each other areas that belong to the same network. During the progressive fading of anesthesia, the rather scattered fragments of functional clusters seen during deeper stages exhibit a tendency to bind themselves together in an increasingly stabler fashion, giving rise to the gradual emergence of time-varying functional networks. It is worth to mention that subcortical structures exhibited a functional connectivity pattern that was very different compared to that of cortical regions, both quantitatively and qualitatively. In fact, subcortical areas displayed overall lower correlations with other areas than cortical ones, together with a less clear footprint of functional clusterization. Another note-

worthy feature is the temporal pattern of co-activations within and between the amydgalas and the hypothalami, which exhibited a peak during the deep phase and then decreased as the effect of anesthesia gradually vanishes, whereas most of the cortical areas (and to some extent the thalami) present increasing functional connectivity over time. These observations, together with recent results showing that local inactivations of wake-active subcortical areas enhance general anesthesia (Leung et al., 2014) suggest that cortical and subcortical structures seem to react to anesthetic in a different fashion, being cortical regions the first ones to recover from anesthetic-induced inactivations compared to subcortical ones.

Interestingly, some of the regions that, on a group level, first showed correlated patterns of BOLD fluctuations while decreasing the level of anesthesia are in fact part of the rat's DMN (Lu et al., 2012), namely mPF, CC, A2, V2M and retrosplenial (Rspl) cortex. Other areas were mainly primary cortices (M1, S1, V1), followed by S2, the thalami and the striatum. The DMN, first isolated in humans (Raichle et al., 2001), has been linked to functions ranging from conceptual processing to self-referential functions (Buckner and Carroll 2007,2008) and awareness (Horovitz et al., 2009), and has been found to be abnormally connected in neuropsychiatric disorders (Whitfield-Gabrieli and Ford, 2012). Interestingly, the DMN has also been found in lightly anesthetized humans (Greicius et al., 2008), chimpanzees (Rilling et al., 2007), macaques (Vincent et al., 2007) and rodents (Lu et al., 2012; Stafford et al., 2014), thus suggesting its evolutionary relevance and persistence in different states, such as during light sedation and the early stages of non-REM sleep (Sämann et al., 2011). Lu and colleagues (Lu et al., 2012) showed that the rat DMN is divided into two modules: one parietal and the other temporo-frontal. Notably, we found that the activity of mPF and CC, core areas of the DMN's temporo-frontal module, was tightly related, whereas V2M and Rspl both participated in another module. Collectively, these evidences indicated that the DMN is one of the brain networks that first emerges in the transition from deep to light anesthesia. Such a finding is not unexpected, given the vast

anatomical connectivity between DMN regions and other cortical and subcortical areas (Lu et al., 2012) that leads to the convergence of incoming activity from many other different regions. Indeed, in humans it has been found that the posterior part of the DMN is one of the most connected areas of the brain (Hagmann et al., 2008). Therefore, it is conceivable that this anatomical confluence of connections from distant areas, together with the dense connectivity within the DMN, could produce amplification in network synchronization, thus making the DMN one of the first networks to emerge in the transition from a state of decreased activity, as exemplified by deep anesthesia. These results are coherent with the finding that, in humans, the physiological, induced or abnormal reductions in the level of conscious awareness are linked with low metabolism in the precuneus and in the posterior cingulate cortex (Laureys et al., 2004), which is structurally homologous to the rat's retrosplenial cortex (Lu et al., 2012). Decoupling of the anterior and posterior components of the DMN has been found to characterize the descent to slow-wave sleep (Sämann et al., 2011) as well as Propofol-induced anesthesia (Boveroux et al., 2010), and decreased activity and connectivity between these regions are also seen in states of unconstrained cognition induced by psychedelic agents like psylocibin (Carhart-Harris et al., 2012). Taken together, all these evidences suggest that the overall integrity and coherency of DMN activity seems to plays an important role in the modulation of either the state and the content of consciousness.

Another noteworthy finding is that, in our data, the activity of the left and right thalami started to be robustly correlated only during the light phase of anesthesia (Figure 2.3C; see Results 2.4). This subcortical structure is the principal gateway of sensory information flowing from the periphery to the cortex (Steriade et al., 1993), and anesthesia-induced deactivations of the thalamus are commonly found in imaging studies (Franks, 2008). Thus the observation that the thalamic nuclei started to entrain in correlated co-activations during light anesthesia could be interpreted as a preliminary step for the gradual recovery from anesthesia-induced non-responsiveness.

Our results show that different regions exhibit different dynamics in recovering from deep phases of anesthesia, thus leading to a gradual patterns of increasing co-activations which likely end up in the progressive reconfiguration of resting state networks; indeed, in the transition from deep to lighter states of anesthesia we observed that the two principal cores of the rat's DMN start to show a strong and consistent pattern of within-core correlations, but our analysis indicated that the collective activity of the two main branches of the DMN seem to be still partially decoupled at this stage of anesthesia, thus suggesting that full network recovery from deep anesthesia fragmentation is a rather continuous but slow process, and in fact we couldn't observe full DMN recovery in our imaging experiments.

On a mesoscopic scale, our LFP results indicate a specific connectional footprint marking the transition from one state to the other. In fact, we found that local neural coupling between regions belonging to the same functional network seems to be preserved even during profound phases of anesthesia. In fact, these areas maintain larger correlated oscillations up to 50 Hz, exhibiting a peak in the α range. Areas belonging to different networks did not show such a strong and consistent correlation peak. This finding reveals the presence of a frequency-specific "functional bridge" that is preserved even during deeper states of anesthesia in areas belonging to the same functional network, and likely endowed by a consistent underlying anatomical connectivity.

As the animal approaches lighter stages of anesthesia, the frequency-coupling scenario became richer. Correlated oscillations in the α band shift toward higher frequencies, up to 15 Hz. It should be noted that recent MEG studies in resting humans have found that the correlations between areas pertaining to the same networks exhibit a peak between 10 and 20 Hz (Brookes et al., 2011; Pasquale et al., 2010; Hipp et al., 2012), and further computational evidence supports those results (Cabral et al., 2014b). More specifically, correlations between DMN areas have been shown to be mostly between 8 and 13 Hz in humans (Brookes et al., 2011). Another feature related to the evolution toward light anesthesia is the appearance of highly correlated oscillations in the low γ

range (30-50 Hz), which is particularly strong between areas belonging to the same functional network. It has been proposed that effective communication between neuronal ensembles is dependent on their ability to oscillate synchronously (Singer, 1999; Fries, 2005), and particularly the synchronization in the γ range is thought to serve as a core computational mechanism between local cortical networks (Fries, 2009). One could thus speculate that the significant drop of correlated γ oscillations seen during the most profound phases of anesthesia could mirror the cortex' inability of performing finely integrated neural computations; this phenomenon, together with the networks' fragmentation characterizing deep anesthesia, suggests some interesting similarities with the breakdown of cortical effective connectivity seen during NREM sleep (Massimini et al., 2005). Deep anesthesia and NREM sleep both are states dominated by local instead of propagating large-scale brain activity, and our results showed that deep anesthesia is indeed characterized by a significant reduction in functional integration. These evidences are in agreement with the hypothesis that the apparent absence of consciousness seen during deep anesthesia and NREM sleep could be linked with weakened or interrupted brain's ability to integrate information (Alkire et al., 2008; Tononi and Massimini, 2008). We believe that taken together, our findings could indicate that one of the global effects of anesthesia is that of reducing the overall dynamical complexity, as also suggested by findings indicating a decrease in EEG signal complexity in deep anesthesia (Bruhn et al., 2000; Zhang et al., 2001; Ferenets et al., 2007).

Finally, it should be noted that our imaging and in vivo results exhibited an interesting degree of qualitative consistency, as both point towards an increase in correlated activity during the progressive emergence from deep anesthesia. In particular, LFP band-limited correlations in the α (8-15 Hz) and especially in the low γ (30-50 Hz) ranges showed the highest similarity to the mean correlation time courses obtained from imaging experiments (Figure 2.6 and Figure B.6 in Supplementary Material). This observation is in accordance with the evidence that increases in the BOLD signal reflect increases in neural activity (Logothetis

et al., 2001; Viswanathan and Freeman, 2007), and that the power of LFP in the mentioned frequencies conveys information about the timing and the amplitude of the hemodynamic signal (Kayser et al., 2004; Niessing et al., 2005; Schlvinck et al., 2010; Pan et al., 2011; Magri et al., 2012). Future studies directly investigating the relationship between correlated BOLD fluctuations and BLCs at specific frequencies will be highly informative in shedding light on the neurophysiological basis of BOLD functional connectivity.

2.6 Limitations

The present study has some intrinsic limitations, thus the interpretation of reported results have to be done cautiously. We induced a profound state of anesthesia using a mixture of ketamine and medetomidine, a combination widely used to anesthetize animals. In fact, ketamine alone produces deep sedation but not surgical anesthesia, which is achieved combining it with medetomidine or xylazine, which supplements ketamine's effect with analgesic properties, muscle relaxation, and sedation. The two drugs have different and specific neurophysiological mechanisms and metabolic properties (ketamine is an NMDA antagonist, whereas medetomidine and xylazine are α-2 agonists, see Brown et al. 2010, 2011), thus the state of anesthesia and the recovery pattern they induce may not be generalized to those determined by other anesthetic agents. It should also be noted that, even though the animals had been treated under the same procedure conditions, other variables cannot be controlled, such as the stress of the animal at the moment of anesthesia induction, the body-fat percentage or the metabolic rate of each animal. The lack of control over these factors produces an individual variability in the time course of the anesthesia across different subjects. In addition to this, the lack of a direct assessment of the ongoing anesthetic concentration at any given time imposed us to use a post-hoc approach to find those protocol intervals that simultaneously showed significant differences in many measures across rats, and that most likely represented different anesthetic depths. This in turn ensured that the properties of the signals recorded from

the two chosen intervals were actually different, but did not imply that the activity recorded in the deep (light) interval represented exactly the same anesthetic depth among animals. However, the chosen intervals largely account for the individual pharmacokinetics of the two drugs (Sinclair, 2003; Brown et al., 2011; Quibell et al., 2011), and can thus be taken as representative of deeper and lighter phases of anesthesia. Despite this limitations, and given that fMRI and LFP weren't recorded simultaneously from the same animal and had slightly different durations, the overall consistency of the present results firmly demonstrates the differential modulation of intrinsic brain activity induced by naturally decreasing levels of anesthesia.

2.7 Conclusions

The progressive emergence from deep anesthesia is characterized by an increase in correlated large-scale low-frequency fluctuations, as well as by an enhancement in the local coupling of band-limited oscillations between areas participating to the same functional network. On the other hand, more profound phases of anesthesia are marked by a decrease in differentiated activity. Progressive fading of anesthesia is mirrored by the gradual flourishing of highly organized spontaneous brain activity, being the default-mode network one of the first networks to emerge. Nonetheless, we observed that local frequency-specific connectivity between areas participating to the same functional networks is preserved also during deeper phases of anesthesia, indicating a partial maintenance of brain functional organization even during states of deep sedation.

In this chapter, we analyzed in detailed the effects that modulation of local dynamics exert on the arising large-scale connectivity structure. In the next chapters, we will first review some of the most common models of mesoscopic brain activity, and later investigate the influence of brain topology in sculpting the emergent correlation structure.

Chapter 3

Modelling brain activity

"Occurrences in this domain are beyond the reach of exact prediction because of the variety of factors in operation, not because of any lack of order in nature."

Albert Einstein

"Essentially, all models are wrong, but some are useful."

George E. P. Box

3.1 Introduction

Our understanding of the world reflects our ability to describe it. Nonetheless, it is important to acknowledge that the same phenomenon can be described in several different ways. Prior to the development of chemistry, our understanding of matter was deeply contaminated by alchemy, based on esoteric concepts and supertitious practices. The alchemic description of matter satisfied many arbitrary and archaic beliefs, such as the existence

of "feminine" or "masculine" properties intrinsic to matter; furthermore, many alchemists explained the differences between elements as due to inherent tautological characteristics such as the "coldness" or the "dryness". With alchemy, we had a description of matter, but this description explained almost nothing: in fact, we didn't understand matter. The goodness of our descriptions depends on how well they *explain* a phenomenon, *i.e.* how well they capture the fundamental properties and laws governing the phenomenon under investigation. The advent of the scientific revolution lead to a progressive and ever-increasing awareness of the importance of *predictions* as the fundamental tools to understand any phenomenon, in that they could be used to test the accuracy of our explanatory hypotheses about the world. One of the fundamental ways to test an hypothesis is through *models*, formal representations of our hypotheses about some specific properties of phenomena, which allows for generating -and testing- specific predictions about them.

The study of the brain has ancient roots, but neuroscience is a young discipline. In fact, hypotheses about the functions of the brain date back to the ancient Egypt at least (see Figure 1 before the first chapter), but it is only with the introduction of more advanced surgical procedures and tools such as the microscope, electroencephalography and magnetic resonance imaging that the study of the nervous system and its relationship with behavior and thought progressively became a scientific discipline. The rather recent application of mathematical modelling to understand the activity and the functions of individual neurons and the nervous system led to significant advances in our understanding of the brain at different scales (Mcculloch and Pitts, 1943; Hodgkin and Huxley, 1952; Bienenstock et al., 1982). With the advent of digital technology, it became possible to test the goodness of our hypotheses through the use of numerical simulations. As mentioned in Section 1.2, it is possible to study the activity of the brain at different levels, from the microscopic (synapses or individual neurons) to the macroscopic (whole-brain) scale; it means that also our models of the brain will focus on different scales and different properties.

Large-scale simulations relying on microscopic description of the neurons have been shown to be possible in principle (Izhikevich and Edelman, 2008). Nonetheless, the complexity of these models makes the interpretation of the underlying mechanisms very difficult, and their microscopic description lead to very high computational costs.

As such, in this chapter we will review some of the most used mesoscopic models of large-scale brain activity, that have the advantages of significantly reduce the complexity of the parameter space and, due to their spatial resolution, allow to explore the goodness with which they approximate spontaneous brain activity as measured with current neuroimaging techniques such as functional magnetic resonance imaging (fMRI, Cabral et al. 2011; Deco et al. 2009b; Deco and Jirsa 2012; Ghosh et al. 2008; Honey et al. 2009), magnetoencephalography (MEG, Cabral et al. 2014a; Nakagawa et al. 2014) and electroencephalography (EEG, Hindriks et al. 2014).

Mesoscopic models describe the activity of large populations of neurons, assuming that their collective behavior can be modelled without the need of accounting for the individual activity of single neurons (Breakspear and Jirsa, 2007). This is in agreement with fundamental results from statistical physics, which have demonstrated that the behavior of macroscopic systems can also be described independently from their meso- or microscopic constituents (Haken, 1975). The models we will review describe each brain region as a node, and usually define the connectivity between different brain regions using information derived either from tract-tracing or diffusion tractography.

Most of the models that we will see are based on different assumptions about the local dynamics characterizing different brain areas, which is crucial to understand the elusive relationship between anatomical structure and the emergent activity pattern. At the same time, each model has its own intrinsic limitations, that have to be acknowledged when it comes to draw conclusions. A spiking network model (see Section 3.5) can for example help us identify the physiological mechanism underlying a given pattern

of emergent activity, whereas a simple oscillator model as the Kuramoto (see Section 3.6) can be used to study the synchronization properties of a system with a much higher computational efficiency but at the cost of sacrificing biophysical accuracy, as this model explicitly abstract population behavior from underlying biological mechanisms governing the activity of individual neurons.

3.2 Conductance-Based Models

One of the first large-scale descriptions of the interregional anatomical connectivity of primate brain was obtained using tract-tracing on the macaque cortex, leading to the CoCoMac database (Kötter, 2004). The information stored in the CoCoMac anatomical connectivity was then used to study the large-scale dynamical coupling between brain regions (Honey et al., 2007) using a biophysical neural-mass model proposed by Breakspear et al. (2003). The same model was then adapted to simulate spontaneous brain activity in the human (Honey et al., 2009) and the impact of lesions in human brain (Alstott et al., 2009).

The model is an adaptation of the formulation proposed by Morris and Lecar (1981), which models the voltage-dependent sodium (Na) and calcium (Ca) channels as well as the relaxation in potassium (K) channels in the neurons, coupled by ligand-based excitatory synaptic currents. In particular, the time evolution of membrane potential of an excitatory pyramidal cell, V, was defined as:

$$\begin{aligned} C\frac{dV}{dt} = &- g_{Ca}m_{Ca}(V - V_{Ca}) - g_{Na}m_{Na}(V - V_{Na}) \\ &- g_K W(V - V_K) - g_L(V - V_L), \end{aligned} \tag{3.1}$$

where C is the neural capacitance, g_{Ca}, g_{Na}, g_K are the conductances; V_{Ca}, V_{Na}, V_K are the Nernst potentials; and m_{Ca}, m_{Na}, and W are the fraction of open ion channels of the Ca, Na, and K

ions, respectively. The passive conductance and voltage of leaky ions are denoted as g_L and V_L.

For each ion, voltage-gates channels open when they exceed the threshold T_{ion}. The fraction of open ion channels m_{ion} for a large number of channels can be approximated as a sigmoid function based on the thresholds following Gaussian distribution with the variance δ_{ion}:

$$m_{ion} = 0.5(1 + tanh(\frac{V - T_{ion}}{\delta_{ion}})), \tag{3.2}$$

The fraction of open potassium channels, W, was approximated with an exponential decay function. Where ϕ is the temperature-scaling factor, and τ is the relaxation time constant:

$$\frac{dW}{dt} = \frac{\phi(m_K - W)}{\tau}, \tag{3.3}$$

Similarly, the average firing rates of excitatory (Q_V) and inhibitory (Q_Z) neurons were approximated over neural populations, assuming a Gaussian distribution with the variance δ, where Q_{Vmax} and Q_{Zmax} are the maximum firing rates of the excitatory and inhibitory neurons, respectively:

$$Q_V = 0.5Q_{Vmax}(1 + tanh(\frac{V - V_T}{\delta_V})), \tag{3.4}$$

$$Q_Z = 0.5Q_{Zmax}(1 + tanh(\frac{Z - Z_T}{\delta_Z})), \tag{3.5}$$

The firing of each cell population feeds back onto the ensemble, thus raising or lowering the membrane potential accordingly.

The synaptic interactions between excitatory and inhibitory populations were modeled as the mean firing rates propagated through synaptic factors for a_{ee} (excitatory-excitatory), a_{ei} (excitatory-inhibitory) and a_{ie} (inhibitory-excitatory) synapses. The excitatory-excitatory synapses were further modeled through the modulation of Na channels by AMPA receptors and of Ca channels by

NMDA receptors. The membrane potential of excitatory (V) and inhibitory (Z) populations are computed as:

$$\begin{aligned}\frac{dV}{dt} = &-(g_{Ca} + r_{NMDA}a_{ee}Q_V)m_{Ca}(V - V_{Ca}) \\ &-(g_{Na}m_{Na} + a_{ee}Q_V)(V - V_{Na}) - g_K W(V - V_K) \\ &- g_L(V - V_L) + a_{ie}ZQ_Z + a_{ne}I_\delta,\end{aligned} \tag{3.6}$$

$$\frac{dZ}{dt} = b(a_{ii}I_\delta + a_{ei}VQ_V), \tag{3.7}$$

where I_δ is the nonspecific noisy subcortical excitation with variance δ and r_{NMDA} is the ratio between NMDA and AMPA receptors.

Finally, to model an array of populations with long-range connectivity between the same NMDA and AMPA receptor targets on pyramidal neurons, the following equation describes the mean membrane potential for pyramidal neurons of node n:

$$\begin{aligned}\frac{dV^n}{dt} = &-(g_{Ca} + (1 - C)r_{NMDA}a_{ee}Q_V^n \\ &+ Cr_{NMDA}a_{ee}\langle Q_V\rangle)m_{Ca}(V^n - V_{Ca}) \\ &- g_K W(V^n - V_K) - g_L(V^n - V_L) \\ &- (g_{Na}m_{Na} + (1 - C)a_{ee}Q_V^n + Ca_{ee}\langle Q_V\rangle) \\ &(V^n - V_{Na}) + a_{ie}ZQ_Z^n + a_{ee}I_\delta,\end{aligned} \tag{3.8}$$

where $\langle\ \rangle$ represents spatial averaging over cell assemblies, resulting in "mean-field" variables. C weights the strength of long-range excitatory couplings, so that, if $C > 0$, interdependencies and complex spontaneous activity patterns arise (Breakspear et al., 2003). The model did not include delays and noise, and its activity is purely generated from nonlinear instabilities due to the complex connectivity and the chaotic dynamics of the neural massess. The model allows for neural interactions at multiple time-scales, and reflects spontaneously arising "self-organizing" activity patterns.

3.3 FitzHugh-Nagumo Model

The brain is a physical object, and as such it is legitimate to think that the time needed to travel along the axonal pathwasy will likely be affected by their length. In fact, the non-homogeneous anatomy of the brain not only determines the simple connectivity between different regions, but also constraints the spatio-temporal structure of the ongoing interactions. To the aim of investigating the effect of neural delays, Ghosh et al. (2008) modeled the spontaneous activity of the macaque using the FitzHugh-Nagumo model (FitzHugh, 1961; Nagumo et al., 1962), and introduced delays as proportional to the euclidean distance between the corresponding brain regions. In this two-dimensional simplification of the Hodgkin-Huxley model (Hodgkin and Huxley, 1952), local dynamics are goverened by the membrane potential u_i and the recovery potential v_i for each node i, as described by the following equations:

$$\frac{du_i(t)}{dt} = l(u_i, v_i) - g\sum_{j=1}^{N} C_{ij}u_j(t - \Delta t_{ij}) + \eta_u(t) \tag{3.9}$$

$$\frac{dv_i(t)}{dt} = h(u_j, v_i) + \eta_v(t) \tag{3.10}$$

$$l(u_i, v_i) = \tau[v_i + \gamma u_i - \frac{u_i^3}{3}] \tag{3.11}$$

$$h(u_i, v_i) = 1 - \frac{1}{\tau}[u_i - \alpha + \beta v_i] \tag{3.12}$$

being g a global scaling parameter, C the connectivity matrix, η additive Gaussian noise, and $\alpha = 1.05$, $\beta = 0.2$, γ =1.0, τ =1.25. In absence of connecions, the system showed damped oscillations, whereas structured fluctuations resembling the resting state networks arose for weak coupling values joint with realistic values of propagation velocity (5-10 m/s). Interestingly, the so-defined "spatio-temporal" connectivity of the network (*i.e.* the use of

distance-based delays on top of the empirical anatomical connectivity) produced slow band-limited power fluctuations at 10 Hz. When the authors converted the simulated signal to a surrogate BOLD signal using the Balloon-Windkessel model (Friston et al., 2003), they observed the existence of correlated fluctuations similar to those observed in resting subjects.

3.4 Wilson-Cowan Model

In 2009, Deco and colleagues (Deco et al., 2009b) studied the effect of delays on the emergence of spontaneous correlated activity using both anatomical and functional data obtained from humans. To this aim, they modelled each local node using two pools of coupled Wilson-Cowan units (Wilson and Cowan, 1972), representing excitatory and inhibitory neurons. Wilson and Cowan proposed that the average activity of a cortical region could be approximated using a mean-field reduction, leading to the use of just two coupled units, one for excitatory (E) and another for inhibitory (I) neurons, whose dynamics evolve according to the the following system of equations:

$$\tau_E \frac{dE(t)}{dt} = -E(t) + \Phi[I_b + w_E E(t) - I(t)] + \delta_E(t) \tag{3.13}$$

$$\tau_I \frac{dI(t)}{dt} = -I(t) + \Phi[w_I E(t)] + \delta_I(t) \tag{3.14}$$

Where τ_E, τ_I and δ_E, δ_I are the time constants and the additive noise of excitatory and inhibitory pools, w_E is the efficiency of the excitatory recurrence, w_I is the excitatory-inhibitory efficiency, I_b is the non-specific background activity and Φ is a non-linear sigmoid function that transforms the currents into firing rates as:

$$\Phi[x] = \frac{c}{1 - exp(-a(x-b))} \tag{3.15}$$

For the large-scale network, with N nodes, the Wilson-Cowan modules were coupled according the connectivity matrix C, with delays defined by the matrix D. The overall dynamics were then simulated as:

$$\tau_E \frac{dE_i(t)}{dt} = -E_i(t) + \Phi[I_b + g \sum_j C_{ji} E_j(t - D_{ji}) - I_i(t)] + \delta_E(t) \tag{3.16}$$

$$\tau_I \frac{dI_i(t)}{dt} = -I_i(t) + \Phi[w_I E_i(t)] + \delta_I(t) \tag{3.17}$$

The global coupling strength was denoted as g, and the recurrent connectivity strengths were set to w_E/g. The rest of the parameters were defined as $\tau_E = 1$, $\tau_I = 0.2$, $w_E = 1.5$, $a = 0.1$, $b = 40$, and $c = 100$.

Deco et al. (2009b) set the spontaneous background activity (I_b) and the efficiency of recurrent connections (w_E) at the edge of a Hopf bifurcation and then investigated the role of global coupling, time delays and noise level. They showed spontaneous gamma (40 Hz) oscillations in the modules that were organized into two competing functional networks. They also showed anti-correlated networks fluctuating in a low-frequency band (0.1 Hz) consistent with the empirical findings (Fox et al., 2005).

3.5 Spiking Neural Network Model

A more realistic description of local nodes was realized in 2012, when Deco and Jirsa (Deco and Jirsa, 2012), following the seminal work of Brunel and Wang (2001), modelled each node as leaky integrate-and-fire neurons arranged in two pools, one excitatory (characterized by AMPA and NMDA receptors) and the other inhibitory (characterized by GABA receptors). In this implementation, the strength of the input determine the system's tendency to exhibit stable patterns of firing activity, stationary states referred to as *attractors* (Deco and Rolls 2006, 2008), wheras the level of

intrinsic of externally applied noise can perturb the stability of those states, teherfore inducing spontaneous transitions between different stable attractors. The spiking activity of each neuron is governed by the dynamics of its membrane potential $V(t)$, which in turn are determined by a set of equations relating $V(t)$ to the leakage and synaptic activity I_{syn} as:

$$C_m \frac{dV(t)}{dt} = -g_m(V(t) - V_L) - I_{syn}(t) \tag{3.18}$$

with membrane capacitance C_m, leak conductance g_m, resting potential V_L and synaptic input current I_{syn}, where

$$I_{syn} = I_{AMPA,ext} + I_{AMPA,rec} + I_{NMDA} + I_{GABA} \tag{3.19}$$

$$I_{AMPA,ext}(t) = g_{AMPA,ext}(V(t) - V_E) \sum_{j=1}^{N_{ext}} s_j^{AMPA,ext}(t) \tag{3.20}$$

$$\frac{ds^{AMPA,ext}(t)}{dt} = \frac{s_j^{AMPA,ext}(t)}{\tau_{AMPA}} + \sum_k \delta(t - t_j^k) \tag{3.21}$$

$$I_{AMPA,rec}(t) = g_{AMPA,rec}(V(t) - V_E) \sum_{j=1}^{N_E} w_j s_j^{AMPA,rec}(t) \tag{3.22}$$

$$\frac{ds^{AMPA,rec}(t)}{dt} = \frac{s_j^{AMPA,rec}(t)}{\tau_{AMPA}} + \sum_k \delta(t - t_j^k) \tag{3.23}$$

$$I_{NMDA}(t) = \frac{g_{NMDA}(V(t) - V_E)}{1 + \lambda e^{-\beta V(t)}} \sum_{j=1}^{N_E} w_j s_j^{NMDA}(t) \tag{3.24}$$

$$\frac{ds^{NMDA}(t)}{dt} = -\frac{s_j^{NMDA}(t)}{\tau_{NMDA,decay}} + \alpha x_j(t)(1 - s_j^{NMDA}(t)) \tag{3.25}$$

$$\frac{dx^{NMDA}(t)}{dt} = -\frac{x_j^{NMDA}(t)}{\tau_{NMDA,rise}} + \sum_k \delta(t - t_j^k) \tag{3.26}$$

$$I_{GABA}(t) = g_{GABA}(V(t) - V_I) \sum_{j=1}^{N_I} w_j s_j^{GABA}(t) \tag{3.27}$$

$$\frac{ds^{GABA}(t)}{dt} = \frac{s_j^{GABA}(t)}{\tau_{GABA}} + \sum_k \delta(t - t_j^k) \tag{3.28}$$

with synaptic conductances g, excitatory and inhibitory reversal potantials V_E and V_I, respectively, the Dirac delta function δ, and synaptic weight parameter w_j (determining the connection strengths between and within neural populations). The gating variables s_j are the fractions of open ion channels of the neurons. Connections between excitatory and inhibitory pools were set to 1, and recurrent self-excitation to w_+=1.5. Synaptic parameters were V_E = 0mV, V_I = -70mV, τ_{AMPA} = 2ms, $\tau_{NMDA,rise} = 2ms$, $\tau_{NMDA,decay}$ = 100ms, τ_{GABA} = 10ms, α = 0.5kHz, β = 0.062, γ = 0.28. Once a neuron crosses V_{thr}, a spike is transmitted to connected neurons, and its membrane potential is reset to, and maintained at V_{reset} for refractory period τ_{ref}.

All neurons in the network received an external background input from N_{ext} = 800 external AMPA signaling excitatory neurons injecting uncorrelated poisson-distributed spike trains, representing the noisy fluctuations that are typically observed *in vivo*. Specifically, for all neurons inside a given population p, the rate v_{ext}^p of the resulting global spike train is described by:

$$\tau_n \frac{dv_{ext}^p(t)}{dt} = -(v_{ext}^p(t) - v_0) + \sigma_v \sqrt[2]{2\tau_n} n^p(t), \tag{3.29}$$

where τ_n = 300ms, v_0 = 2.4kHz, σ_v is the standard deviation of $v_{ext}^p(t)$, and $n^p(t)$ is normalized Gaussian white noise. Negative values of $v_{ext}^p(t)$, that could arise due to the noise term, are rectified to zero. After applying the mean-field reduction to the above

spiking model (Deco et al., 2013), the activity can be described as:

$$\frac{dS_i(t)}{dt} = -\frac{S_i}{\tau_S} + (1 - S_i)\gamma H(x_i) + \sigma \upsilon_i(t), \tag{3.30}$$

$$H(x_i) = \frac{ax_i - b}{1 - exp(-d(ax_i - b))}\,, \tag{3.31}$$

$$x_i = wJ_N S_i + GJ_N \sum_j C_{ij} S_j + I_0, p \tag{3.32}$$

where $H(x_i)$ and S_i denote the population rate and the average synaptic gating variable for each local cortical area, C_{ij} is the anatomical connectivity matrix containing the link strengths between brain areas i and j, and local excitatory recurrence w is 0.9. Parameter values for the inputoutput function are $a = 270$ (VnC), $b = 108$ (Hz), and $d = 0.154$ (s). The kinetic parameters are $\gamma = 0.641/1000$. (The factor 1000 is for expressing everything in ms), $\tau_S = 100$ (ms). The synaptic couplings are $J_N = 0.2609$ (nA) and the overall effective external input is $I_0 = 0.3$ (nA). In equation (3.30), υ_i is uncorrelated standard Gaussian noise and the effective noise amplitude at each node is $\sigma = 0.001$ (nA).

The mean-field approximation was evaluated for different initial conditions, necessary step to confirm wheter neuronal populations lies within the inactive or the active states, characterized by oscillation ar 3 Hz or 10 Hz, respectively. The system was simulated using different values of global coupling, each time counting the total number of resulting attractors (*i.e.* the number of different activity states). This procedure allowed for a characterization of the so-called attractor landscape of cortical large-scale activity, and suggested the existence of a critical value of global coupling for which the system became unstable, *i.e.* dynamically moved from one stable state to the other. Remarkably, this model showed the greatest similarity with empirical data just before this critical point, suggesting that brain activity seems to lie at the

edge of the instability, region where it can exhibit different stable states.

3.6 Kuramoto Model

Cabral et al. (2011) proposed a simplified model of the spontaneous regional interactions based on the Kuramoto formalism. This formalism approximates the activity of interacting units considering them as coupled oscillators described by their phases (Kuramoto, 1984). Given N regions, where the phase of the oscillator i ($i = 1, ..., N$) at time t is denoted by ϕ_i, the time evolution of the phases is defined by:

$$\frac{d\phi_i(t)}{dt} = \omega_i + \xi_i(t) + g \sum_{j=1}^{N} C_{ij} sin(\phi_j(t - \tau_{ij}) - \phi_i(t)) \quad (3.33)$$

Here, ω_i is the natural frequency of each oscillator, g is the global coupling parameter, C_{ij} is the effective connectivity between nodes i and j, and ξ_i is uncorrelated Gaussian noise with zero mean and standard deviation σ. In their work, Cabral and colleagues introduced also delays between different nodes i and j, τ_{ij}, using conduction velocity and distance between two nodes.The natural frequencies of each region were set to oscillate in the gamma frequency range (30-80 Hz), being drawn from a Gaussian distribution with 60 Hz mean and f standard deviation. The authors explored for different values of global coupling g and average delay $\langle\tau\rangle$. The simulated neuronal activity was then transformed into a BOLD signal using the Balloon-Windkessel model (Friston et al., 2003), and computed the simulated functional connectivity between brain regions. The maximal similarity between simulated and empirical functional connectivity corresponded to a point between fully synchronized and asynchronous regimes. The nonlinear interactions between oscillators generated non-stationary correlation patterns.

3.7 Hopf Normal Model

A novel formalism, adopted by Deco and colleagues (Deco and Kringelbach, 2016), promises to reconcile noise-based approaches with models based on oscillators. This formalism is based on the normal form of a Hopf bifurcation (Freyer et al. 2011, 2012). In the study of dynamical systems, *bifurcation* refers to the abrupt change in the qualitative behavior of a system after trespassing the critical value of one or more parameters; in particular, a *Hopf bifurcation* occurs when a system characterized by a stable fixed point loses its stability by exhibiting oscillations. As such, this model allows transitions between asynchronous noise activity and oscillations, thus making it a good candidate to reproduce empirical data as observed either with EEG, MEG or fMRI. Within this model, the temporal evolution of the activity z of node j is given in the complex domain as:

$$\frac{dz_j}{dt} = [\alpha_j + i\omega_j - |z^2|] + \sigma\eta_j(t) \tag{3.34}$$

$$z_j = \rho_j e^{i\theta_j} = x_j + iy_j \tag{3.35}$$

Where ω is the node's intrinsic frequency of oscillation, α is the local bifurcation parameter (local because the model allows the possibility to assign a different value of α for each node in the network) and η is additive Gaussian noise with standard deviation σ.

This system above shows a supercritical bifurcation at $\alpha = 0$. Specifically, if α_j is smaller than 0, then the local dynamic has a stable fixed point at $z_j = 0$, while for α_j values larger than 0 there exists a stable limit-cycle oscillation of frequency $f = \omega/2\pi$. Whole-brain dynamics are described by the following coupled equations:

$$\frac{dx_j}{dt} = [\alpha_j - x_j^2 - y_j^2]x_j - \omega_j y_j + g\sum_{i=1}^{N} C_{ij}(x_i - x_j) + \sigma\eta_{xj}(t) \tag{3.36}$$

$$\frac{dy_j}{dt} = [\alpha_j - x_j^2 - y_j^2]y_j - \omega_j x_j + g\sum_{i=1}^{N} C_{ij}(y_i - y_j) + \sigma\eta_{yj}(t) \tag{3.37}$$

Where C_{ij} is the anatomical connectivity between nodes i and j, g is the global coupling factor and the standard deviation of gaussian noise is $\sigma = 0.02$. In this model the simulated activity corresponds to the BOLD signal of each node. The intrinsic frequency of each node was estimated as the peak frequency in the associated narrowband (*i.e.*, 0.04 - 0.07 Hz) of the empirical BOLD signals of each brain region (see Figure 3.1).

The authors showed that empirical and simulated FC matrices showed higher correlation when the local bifurcations parameters were set to critical point ($\alpha = 0$, see Figure 3.1d), suggesting that the spontaneous co-activitations of the brain likely derive from an underlying activity characterized by noisy oscillations.

In the next chapter, we will use the Hopf model to explore how simple topologies shape the correlation between given pair of nodes in a network, and then we will apply this model to try to reproduce empirical spontaneous brain correlations obtained from resting-state fMRI.

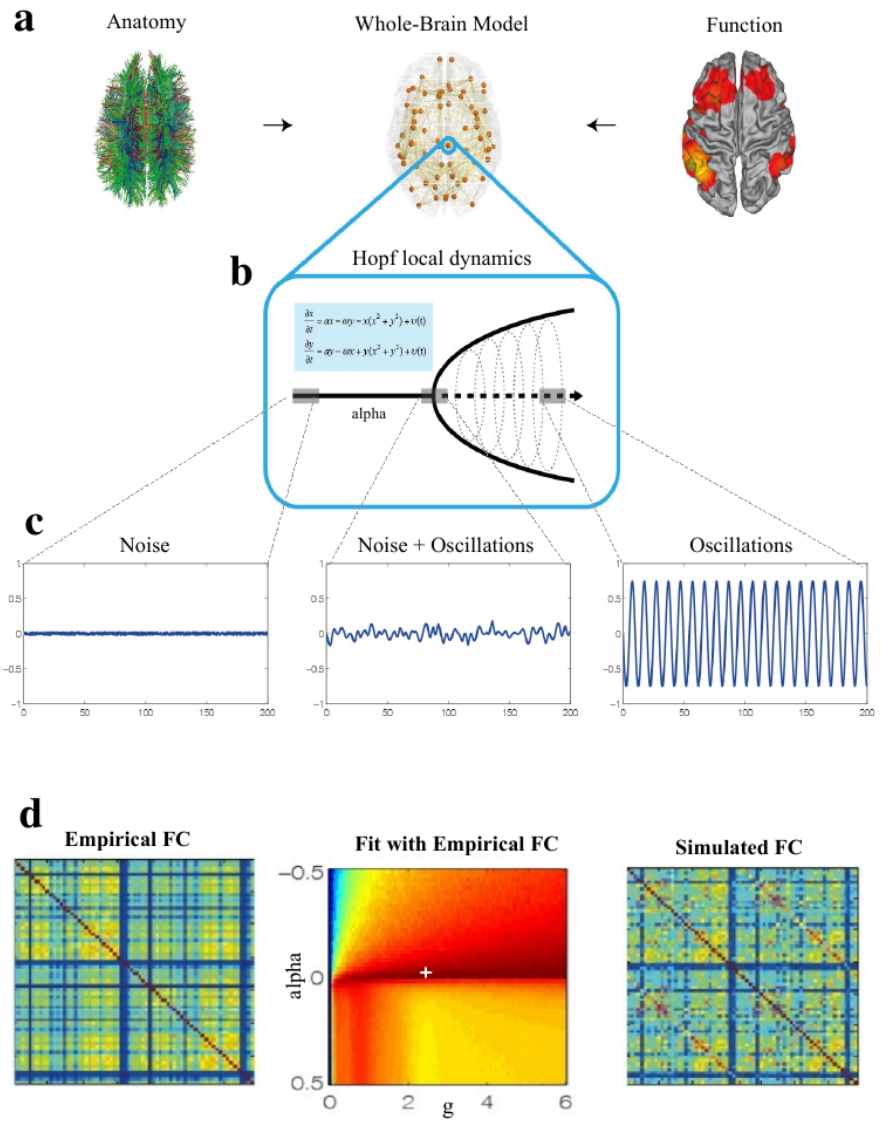

Figure 3.1: Overview of the Hopf model. (a) The whole-brain model was based on DTI (left) between the 68 regions of the Desikan-Kahilly parcellation (middle). The control parameters of the models were tuned using the grand average FC derived from BOLD (right). (b) Local neural masses were modelled using the normal form of a Hopf bifurcation; (c) depending on the bifurcation parameter *alpha*, the local model generates signal of different types. (d) Average functional connectivity (FC) matrix (left), correlation between empirical and simulated FC matrix for different combinations of global coupling g and the bifurcation parameter α (alpha) (middle), best-fitting simulated FC (right), obtained in the region marked by the white cross in the middle panel of (c).

Chapter 4

How topology sculpts interactions

"What I cannot create, I don't understand"

Richard Feynman

"In science it is possible to learn the greatest things by studying what seem to be the smallest ones"

Marvin Minsky

4.1 Introduction

The brain is a complex system and as such, the dynamics of its components cannot be fully understood without taking into account the rich patterns of interactions into which they are inherently embedded into.

It is already well established that the relationships between all elements of a system can be better understood when considering

both the local dynamics and the organizational principles underlying them, in other words the local and global topological properties of the network describing those relationships (Zhou et al., 2007; Newman et al., 2011; Zamora-López et al., 2011; Deco et al., 2013; Cabral et al., 2014a).

Many models can be (and have been - see Chapter 3) used to explore the non-trivial relationship between local brain dynamics and network structure, in order to explain the complex emergent pattern of interactions and associations empirically observed between different brain regions.

In Chapter 2, we addressed how a gradual modulation of the local dynamics (through anesthesia) could lead to a corresponding change in the strength of the observed covariation pattern exhibited by distant areas. In this chapter, we will try to close the circle focusing on the contribution of the precise structure of the relationships between individual brain regions (determined by their underlying anatomical connectivity) in sculpting the whole pattern of correlated activity they tend to show. How much of the observed coupling can be understood just in terms of circumscribed local interactions, and how much of it is instead shaped by the ongoing activity of the entire network?

To answer these questions, we will first use numerical simulations to analyze how simple topological motifs determine the correlation between different nodes, and then apply this knowledge to properly quantify the contribution of topology in the correlation patterns observed in empirical data.

4.2 Exploring simple topologies

The topologies that we will present in this section (see Figure 4.1 for a schematic overview) are just a small fraction of all possible "topological units" forming the building blocks of larger and more complex networks; nonetheless, we believe that this network motifs can be considered both representative of the most frequent topological primitives found in real networks, and relevant to un-

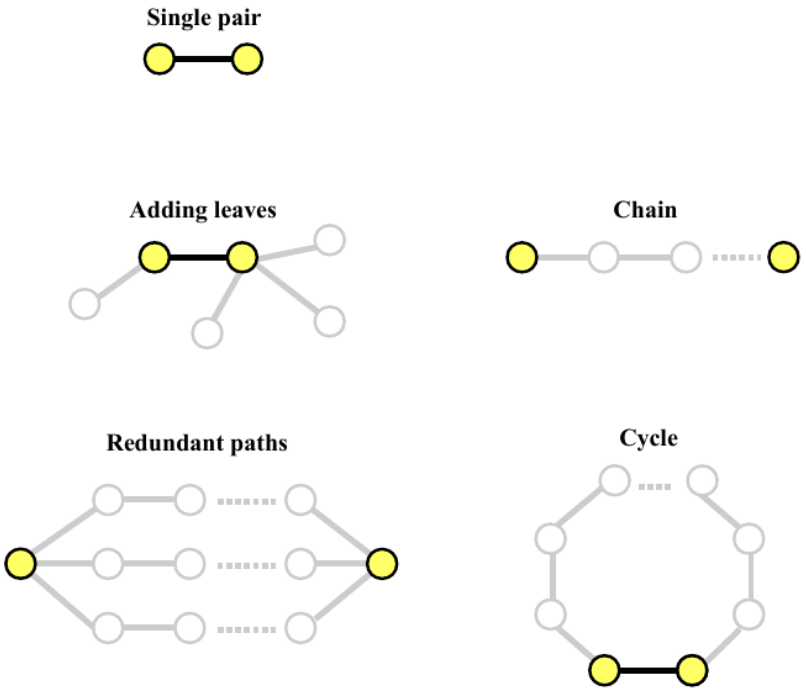

Figure 4.1: Simple network topologies. Examples of the five topological primitives that will be analyzed in the present section. In all cases, we will focus on quantifying the influence that variations of these five motifs exert on the correlation between the activity of the *reference nodes* (highlighted), while ignoring the interactions between all other nodes.

derstand the emergence of local and diffuse whole-network interactions.

The behavior displayed by the selected network models was estimated using the Hopf model, in order to be able to more easily translate, in a later section, the obtained insights to more complex scenarios based on empirical data and modelled using the same dynamical model. In fact, as already mentioned in Section 3.7, the Hopf model is capable of reproducing in a rather accurate way many features of real brain dynamical activity and co-activations

(Deco and Kringelbach, 2016), making it a good candidate for our purposes.

The Hopf model rely on the choice of two parameters, namely g, the global scaling of the strength of all the links in the network, and α, the parameter controlling the dynamical regime of each node. Throughout the current chapter, both g and α will be set to the values returning the best fit with empirical data. The bifurcation parameter α will be set to 0 (meaning that all nodes lie at the bifurcation working point, see Section 3.7), and we will thus optimize for g. In our case, the best-fitting global coupling value corresponds to 1.262 (see Section 4.4 below). As mentioned above, this optimization has been motivated by the desire of being able to ease the interpretation of the following sections, aimed at understanding the topological determinants underlying the correlation pattern observed in empirical data. Different values of g and α may of course determine quantitative differences in the correlations exhibited by the topological primitives we will analyze; nonetheless, the general patterns of results should not vary qualitatively (with the trivial exception of extreme values, uninteresting for our purposes). The set of connection weights we will use in the following network models is analogous to that of the normalized empirical structural connectivity matrix (SC), which ranges from 0 to 0.2. The remaining simulation parameters were also set accordingly to those later used for the following simulations based on empirical data, namely the simulation length (t_{sim} = 330000 points), integration step ($dt = 0.01$), standard deviation of additive gaussian noise ($\sigma = 0.02$) and the intrinsic frequencies of the nodes (ω, that ranged from 0.04 to 0.07 Hz, according to Glerean et al. 2012, see also Figure 1.13 in the first chapter).

Note that the intrinsic frequencies of the nodes were randomly extracted for each simulation repetition, in order to control for possible biases in the results due to specific differences in the frequencies of the two reference nodes. Each parameter configuration of each network model was simulated 100 times, and the results averaged.

4.2.1 Single pair of nodes

The first step is evaluating the simplest possible two-node topology, that formed only by the two reference nodes and the direct connection between them (in the network models that we will analyze, self-connectivity of nodes will always be set to zero). To obtain a more complete picture, we not only evaluated how the strength of the direct connection between the reference nodes, w_0, determines the resulting correlation between their activity, r_0, but also how different values of the global coupling parameter g modulated the relationship between the underlying structure and the strength of the covariation it generates (note that this will be the only case in which we varied g, as in all other cases it will be set to 1.236, see Section 4.2 above). Results are depicted in Figure 4.2.

In a simple framework like this it is possible to appreciate the fundamental functional isomorphism existing between the global coupling g and the strength of the links, w_0. This is not surprising, as the explicit role of the global coupling in the model we use is that of scaling the values contained in the matrix defining the connectivity structure of the network, and as such its influence on the final correlation between pair of nodes is virtually analogous to that of the links' strength, thus eventually governed by the dynamical model in use (the Hopf model in this case). Small values of both generated relatively small linear increases in the level of the correlation exhibited by the reference nodes, whereas as far as w_0 increases (through g), the relationship deviates from linearity, approaching saturation at increasing rates.

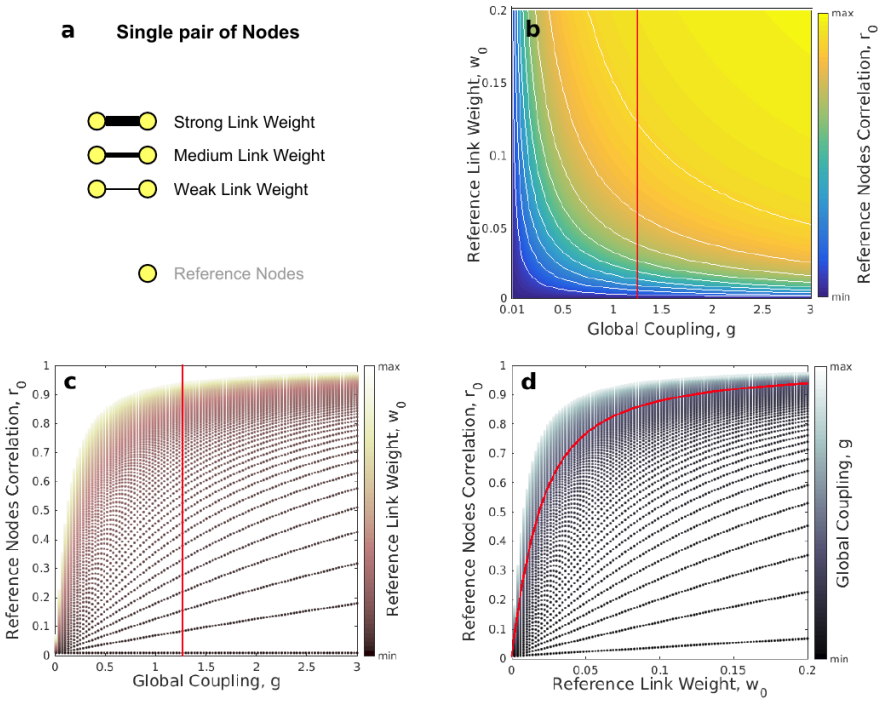

Figure 4.2: Single pair of nodes. The simplest network topology we analyze is that formed by the two reference nodes and the direct connection between them (if present). (a) Schematic representation of three instances of the network model. (b) Parameters space of the network topology under scrutiny. (c,d) Different representations of the same parameter space, illustrating the substantial isomorphism between global coupling and connection weight. The correlation between the reference nodes, r_0, is a function of the strength of their connection, w_0, being the global coupling g a scaling factor of w_0; the actual strength of the link between the reference nodes for any combination of w_0 and g is in fact given by gw_0. Beyond a given connection strength, the function saturates. In panels (b-d) the red line corresponds to the value of g that best fitted the empirical correlation matrix obtained using the empirical structural matrix (see section 4.4 below). This is the value of g that we will use in the following network topologies.

4.2.2 Adding leaves

Understanding the factors behind changes in the correlation between the activity of single pairs of nodes is fundamental to understand the behavior of any larger network, as it describes the simplest possible interaction (with the exception of self-connections). Nonetheless, this situation is also the less interesting: pure two-nodes topologies are in fact virtually absent in nature, as nodes tend to have more then one connected neighbor.

In this section, we will analyze how additional nodes, connected with one and only one of the two reference nodes, modulate the correlation displayed by the reference nodes, r_0. In graph theory, nodes connected with exactly one other node in the network are called either *leaves* or *hairs* (Bang-Jensen and Gutin 2008, see Figure 4.3 for a schematic representation). In the following, we will adopt the former term.

We will summarize only two extreme cases, namely when only one leaf is added, and when $N = 50$ leaves are added to the same reference node. The range of values that any individual link w in the network can have is $[0, 0.2]$, as such the maximal total weight W for 50 leaves is 10. As mentioned in the caption of Figure 4.3, in the second scenario we varied the total strength of the independent links W by setting that, for each combination of w_0 and W that we analyzed, the strength of all the leaves was identical, corresponding to $w = {}^{W}/_{N}$. A possible measure of the influence that additional leaves exert on the level of correlation between the reference nodes r_0 can be provided by computing the difference between r_0 obtained when both the connection between the reference nodes, w_0, and those with the leaves, W, are present (*i.e.* when $w_0 > 0$ and $W > 0$), and r_0 obtained when there are no leaves at all (*i.e.* when $w_0 > 0$ and $W = 0$). It is legitimate to believe that, if the reference nodes are not connected between them (*i.e.* when $w_0 = 0$), their correlation will fluctuate around zero in all cases, and thus will not be affected by adding extra leaves. As such, we can denote the change in r_0 due to the extra link(s) weight(s) W as

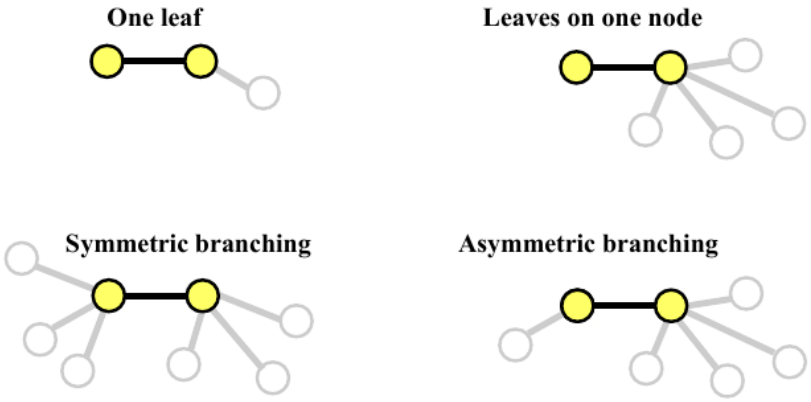

Figure 4.3: Adding leaves. Examples of the four type of simple branching analyzed. The simplest case is given by the presence of only one leaf, connected with either one of the two reference nodes. In the second case, we connected multiple leaves with either one of the reference nodes, and none with the other. The other two scenarios are when the number of leaves connected with the two reference nodes is identical, and when there is an asymmetry in the number of leaves connected to the two reference nodes. By definition, each leaf is connected with one and only one other node, *i.e.* the degree of each leaf is 1 (see Appendix C.2). In the present section, we will analyz simple networks where each leaf is directly connected only with one of the two reference nodes. No leaf is ever connected with both the reference nodes, nor with another leaf. For each of these four cases, the only parameters that we will manipulate are the weight of the reference nodes, w_0, the total number of leaves, N, and the weight of the connection between the leaf and the reference node, w. To ease the interpretation of the results, we set that, when $N > 1$, the weights of all leaves are identical. The total weight of all leaves, W, thus corresponds to $W = wN$. In every case, we are interested in the resulting correlation r_0 between the reference nodes (highlighted). Results obtained from the four scenarios are qualitatively identical for identical values of W, demonstrating the substantial additivity of the influence of each individual leaf. For simplicity, in the following we will show only two extreme examples: when only one leaf is added, and when 50 leaves are added to the same reference node.

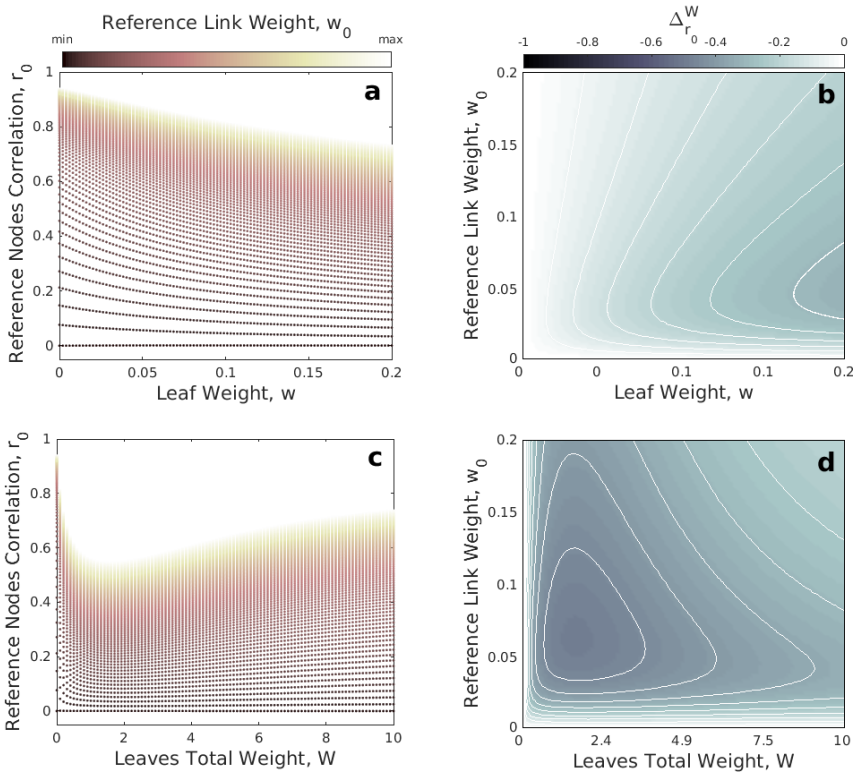

Figure 4.4: Effect of adding leaves to the reference nodes. (a) Correlation between the reference nodes, r_0, for different combinations of w_0 and the weight of the unique added leaf, w. (b) Change in r_0 due to the weight of the unique added leaf, w. (c) Correlation between the reference nodes, r_0, for different combinations of w_0 and the total weight of the 50 added leaves, W. (d) Change in r_0 due to the total weight of the 50 added leaves, W.

$$\Delta_{r_0}^{W} = (\, r_0 |\, W > 0) - (\, r_0 |\, W = 0), \tag{4.1}$$

which approximates the contribution of adding extra leaves in determining the correlation between the reference nodes. Results for the two cases are shown in Figure 4.4.

Interestingly, the effect of extra leaves on the covariation between the reference nodes is not as intuitive as one could have

guessed. As expected, when the reference nodes are disconnected ($w_0 = 0$) adding extra leaves have no effect on their correlation, which remains null. Nonetheless, when the reference nodes are connected ($w_0 > 0$) their correlation decreases until a given value of W, beyond which it slowly raises up. The $\Delta^W_{r_0}$ landscape (Figure 4.4d) shows that the maximal decrease in the correlation between the reference nodes seems to be achieved when $w_0 \approx 0.06$ and $W \approx 0.2$. Why r_0 does not decrease monotonically with the increasing strength of leaves weights? There are two possible (not necessarily alternative) explanations: one is that the system, based on the Hopf model, exhibits stochastic resonance, as suggested by the presence of a clear global minimum; the other is that the homogeneous increase in w has the effect of enhancing the statistical dependence between the leaves, that are all indirectly connected through the same reference node, a phenomenon known as *remote synchronization* (Nicosia et al., 2013; Gambuzza et al., 2013).

4.2.3 Chains

The following scenario is given by simple chain structures, *i.e.* networks of N nodes where $N-2$ nodes are connected with exactly two other nodes, and the remaining 2 nodes (the two ends of the chain) are connected with only one node. It follows that in a chain of N nodes the total number of links is $L = N - 1$ (see Fig.4.5a for a schematic representation of chain structures). In graph theory and applied network science, chains are also referred to as *paths* (Bang-Jensen and Gutin, 2008), term that we will use interchangeably with chain throughout the current chapter.

In order to quantify the influence that chain structures have on the correlation r_0 between the reference nodes (posed at the two extremities of the path), the most relevant topological features to manipulate are on one hand the total length of the chain, L, corresponding to the the number of links separating the two reference nodes, and on the other hand the weights of all L links in the path, each one denoted as w. Nonetheless, trying to systematically evaluate all possible combinations of w for different lengths L is computationally expensive, and its relevance in determining the correlation between the nodes at the two ends is likely small compared to, for example, the mean weight of the whole path. As such, as a first approximation and to reduce the complexity of the model, we chose to assign equal weights w to all L links in the chain, and then exploring for different values of both w and L. According to the choice we made, namely that $w_k = w_j$, where $k \neq j$, for all L links in a chain, the following relationship holds

$$\langle w \rangle = \frac{1}{L} \sum_{k=1}^{L} w = w, \tag{4.2}$$

Where $\langle w \rangle$ denotes the mean weight of the links in the chain. We thus simulated chains of varying length, L, and strength, w, and computed the correlation between the reference nodes at the two extremes of the chain, r_0. Results are illustrated in Figure 4.5.

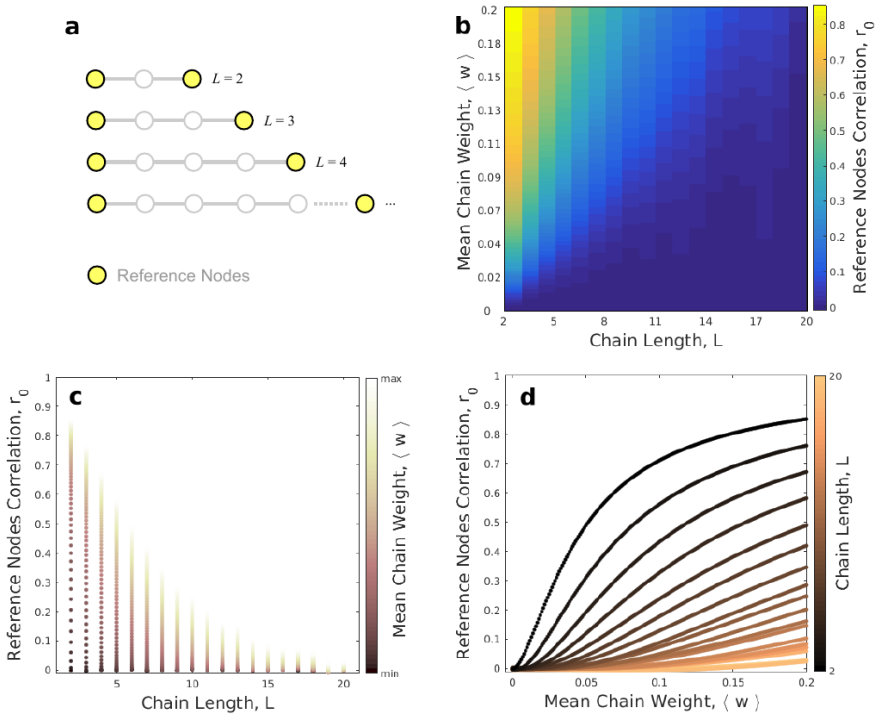

Figure 4.5: Effect of chain length and strength. (a) Schematic representation of chain topologies of varying length, L. We are interested in evaluating how the path length, L, and the mean weight of all links in the path, $\langle w \rangle$, affect the correlation between the reference nodes, r_0. (b) Reference nodes correlation, r_0, for different combinations of chain length, L, and mean chain weight, $\langle w \rangle$. (c) Focus on the relationship between L and r_0 for different values of mean path weight, $\langle w \rangle$. (d) Focus on the relationship between $\langle w \rangle$ and r_0 for different values of path length, L. In general, the correlation between the two reference nodes is higher for shorter chains, whereas the mean path strength appears to play a secundary modulatory role.

It is possible to appreciate that the length of the chain and its mean strength differentially modulate the correlation of the reference nodes: as expected, for identical chain lengths, stronger links' weights always correspond to larger r_0, whereas for identical $\langle w \rangle$, the increase in the correlation between the reference nodes is much larger for shorter chains. Nonetheless, the length of the chain plays a dominant role, as even very strong chains have little effect on r_0 if they are too long. This pattern of results demonstrates that the size of the correlation between two nodes placed at the extremities of a chain will approximately depend on the inverse of the path length, only modulated by its mean strength. This finding is is in accordance with both the formalization of the notion of network efficiency, and the observation that many real networks (as brain ones) tend to show small average path lengths and small-world architectures (Watts and Strogatz 1998; Latora and Marchiori 2001; Sporns et al. 2002; Sporns and Zwi 2004; Bullmore and Sporns 2009, see Appendix C).

4.2.4 Path redundancy

Within a simple chain topology, the size of the correlation between the end nodes is mainly determined by the number of links separating them, and modulated by the mean weight of the path. Nonetheless, the number of paths connecting two nodes are usually more then one. To be precise, it is well known that the number of paths of length L between any pair of nodes in a network is given exactly by the powers of the adjacency matrix defining the non-zero links of that network, A^L (Biggs 1993; Bang-Jensen and Gutin 2008, see Appendix C.5); this implies that the theoretical total number of paths of *any* length between each pair of nodes is indeed infinite. Nonetheless, the observations reported in the previous section (4.2.3) demonstrate the decay of the influence exerted by long paths on the nodes at its ends and, as such, it is legitimate to restrict our analysis to relatively short paths. The inherent existence of multiple alternatives paths of different length demonstrate that the connectivity between nodes always tend to display some degree of *path redundancy*. We thus focused on quantifing the effect of such redundancy on the correlation r_0 between a given pair of reference nodes (see Figure 4.6 for a schematic representation).

To this aim, we built chain networks with paths of different length, L, and different mean chain weight $\langle w \rangle$ (as in Section 4.2.3), and systematically evaluated how adding paths of the same length (*i.e.* increasing path redundancy) influenced the correlation between the nodes at the two ends of the path. Results are shown in Figure 4.7.

In accordance to the previous findings, the path length L seems to play a major role in determining the correlation between the reference nodes, as evident from the bottom-rightest panel in Figure 4.7: if the chain is too long, the correlation between the reference node will be low, independently on the strength of the chain and its redundancy. The mean path weight $\langle w \rangle$ and path redundancy though modulate r_0 iin similar manners, amplifying it when the path is short enough.

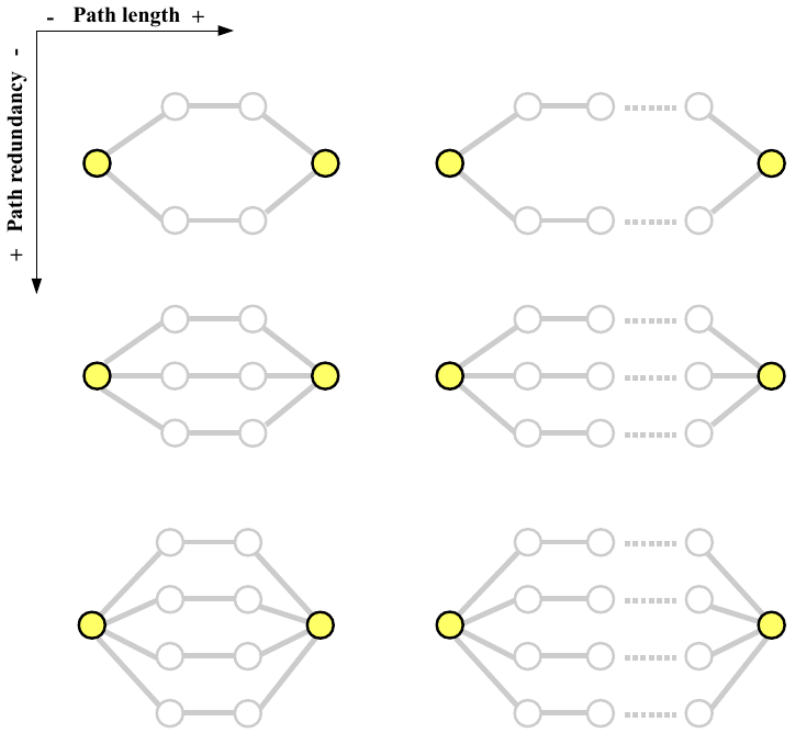

Figure 4.6: Redundant paths of different length. Examples of the framework we used to analyze the joint effect of path redundancy and path length in the correlation between the two reference nodes (highlighted). On the horizontal axis are examples of chain topologies of increasing path length, whereas in the vertical axis of increasing path redundancy (from top to bottom). In the current section, we will analyze also the effect that a third factor, namely the mean weight of the links in each path, $\langle w \rangle$, exerts on the resulting r_0. For simplicity, different mean path weights are not shown in the present figure.

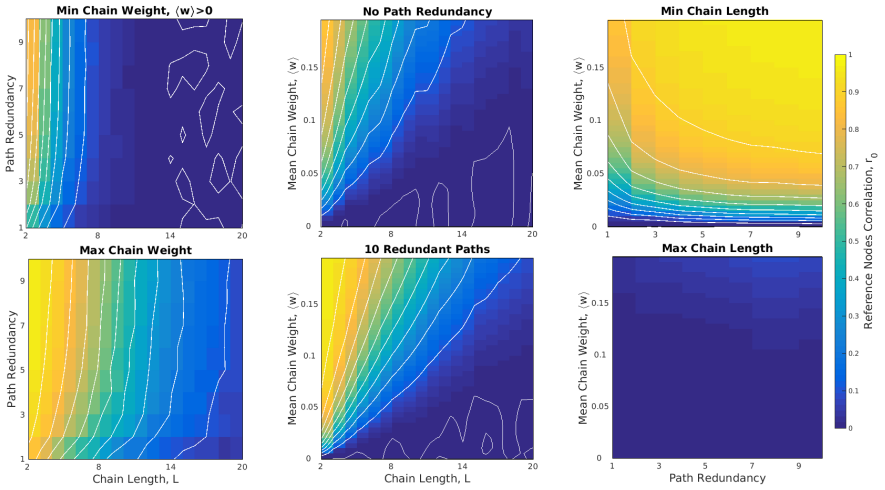

Figure 4.7: Effect of Redundant paths. Selection of different combinations of mean chain weight, path redundancy and chain length in determining the correlation between the reference nodes, r_0 (represented using the color code). The panels summarize the most informative regions of the three-dimensional space we explored. (First column) Top: correlation between the reference nodes, r_0, as a function of both chain length L and path redundancy (*i.e.* number of paths of length L connecting the reference nodes), for mean chain weight $\langle w \rangle = 0.05$ (in fact, when $\langle w \rangle = 0$, obviously $r_0 = 0$). Bottom: r_0 when the mean chain weight is maximal, $\langle w \rangle = 0.2$. (Second column) Top: correlation between the reference nodes, r_0, as a function of both chain length L and mean chain weight, $\langle w \rangle$, when there is no redundancy (*i.e.* there is only one path connecting the two reference nodes). This situation corresponds to that displayed in Figure 4.5. Bottom: r_0 when there are a total of 10 paths connecting the reference nodes (which corresponds to the maximal path redundancy we analyzed). (Third column) Top: correlation between the reference nodes, r_0, as a function of both path redundancy and mean chain weight, $\langle w \rangle$, for the shortest chain length, $L = 2$. Bottom: correlation between the reference nodes for the maximal chain length analyzed, $L = 20$.

4.2.5 Cycles

The last topological primitive we will analyze are cycles, that can be obtained connecting the two ends of a chain. In a cycle (also called *ring* or *polygon*, see Figure 4.8), every node's degree equals 2, and the cycle perimeter P (*i.e.* the total number of links) corresponds to the number of nodes N. Cycles and chains show analogous synchronization properties, with the trivial exception, in chains, of that between the nodes at the two extremities. Indeed, chains can be seen as special cases of cycles where exactly one link equals zero.

In the following, we will analyze how the correlation r_0 between two adjacent nodes embedded in a cyclic network varies depending on the weight of their connection w_0, the mean strength of the chain, $\langle w \rangle$, and its length, L. The smallest possible cycles are triangles, and the relevance of triangular motifs has been widely

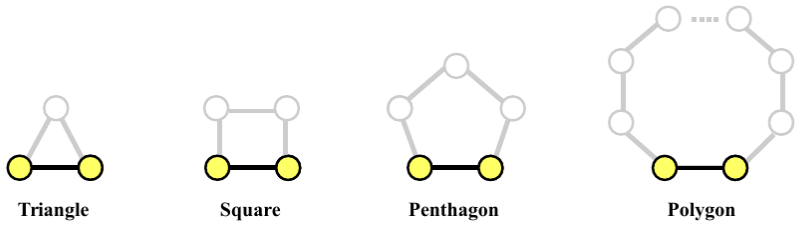

Figure 4.8: Cyclic topologies. Four examples of cyclic graphs. In this section, we will analyze how cycles of different perimeter P affect the correlation r_0 between the reference nodes (highlighted), that will be connected both by a direct link (the black line) and through a chain of length L (in grey), whose length will thus correspond to $N-1$ (which by definition corresponds to $P-1$). The parameters we will manipulate will be the weight of the direct link between the reference nodes, w_0, the mean weight of the remaining links forming the chain, $\langle w \rangle$, and the length of the chain, L. Following the same procedure than that adopted for the analysis of chains (Section 4.2.3) and redundant paths (Section 4.2.4), all the individual links in the chain will have identical weight, w.

studied both theoretically and in real networks (Milo et al., 2002; Sporns and Kötter, 2004). As such, we will first focus on considering triangular networks (results summarized in Figure 4.9), and then analyze cycles of increasing perimeter.

As expected, the correlation between the reference nodes embedded in triangular topologies is mainly affected by the strength of the direct link connecting them, whereas the effect of the other two links is mainly that of facilitating the correlation between the reference nodes. These findings corroborate observations showing that two nodes that are not directly connected can synchronize their activity by virtue of a third node acting as relay (Milo et al., 2002; Arenas et al., 2008), which is the simplest case of remote synchronization. Results for cycles of increasing perimeter are summarized in Figure 4.10.

Not surprisingly, the effect of cyclic topologies is a product of those observed for single pair (Section 4.2.1) and chain structures (Section 4.2.3). Indeed, when $w_0 = 0$, the pattern recapitulates that obtained for chain topologies (compare also with first column of Figure 4.9, corresponding to the shortest possible path between two nodes). When the weight of the link between the reference node is either $w_0 = 0$ or $w_0 > 0$, the facilitation in the correlation between the reference nodes r_0 depends on the mean chain weight $\langle w \rangle$, and inversely on its length L, where the latter bounds the size of the influence that even strong paths can exert.

The results of the present section demonstrate the fundamental role that topology plays in sculpting the correlation exhibited by a given pair of nodes, and points to the crucial relevance exerted by the path length. In fact, the minimum number of links separating two nodes inherently constraints the strength of the co-variation they can exhibit, regardless of their strength or redundancy.

In the following, we will employ the knowledge gained so far to construct a novel measure of the strength of the covariation that one can expect between any pair of nodes in a network, based only on their global topological properties.

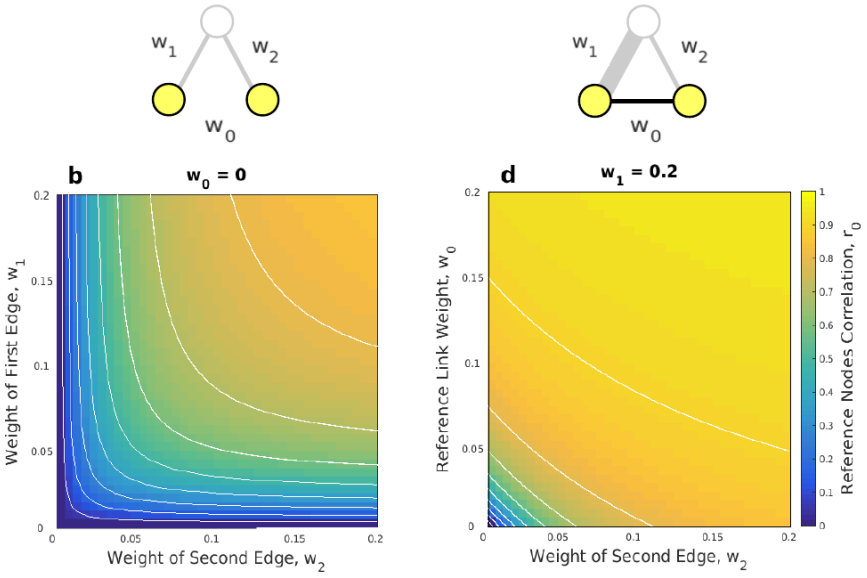

Figure 4.9: Triangular networks. We systematically varied the weight of links forming the three edges of the triangle in order to evaluate how they affect the correlation between the reference nodes, r_0. The weights of the three edges are denoted as w_0, w_1 and w_2, being w_0 the link connecting the reference nodes (highlighted in the two schematic representations at the top of the figure). The panels above represent the two most informative instances of the whole 3D parameter space we analyzed, sufficient to understand the complete relationships between w_0, w_1 and w_2 in determining r_0. Even if the first case (first column) does not actually correspond to a cycle (in fact it is the shortest chain, see Section 4.2.3), it is useful to understand the general behavior of triangular motifs: in absence of a direct connection between the reference nodes, r_0 is driven by the third node, whose influence increases as a function of the strength of the two existing links, being maximal when $w_1 = w_2$. The second column illustrates a proper example of triangular topology, where it is possible to appreciate the facilitating effect of w_2.

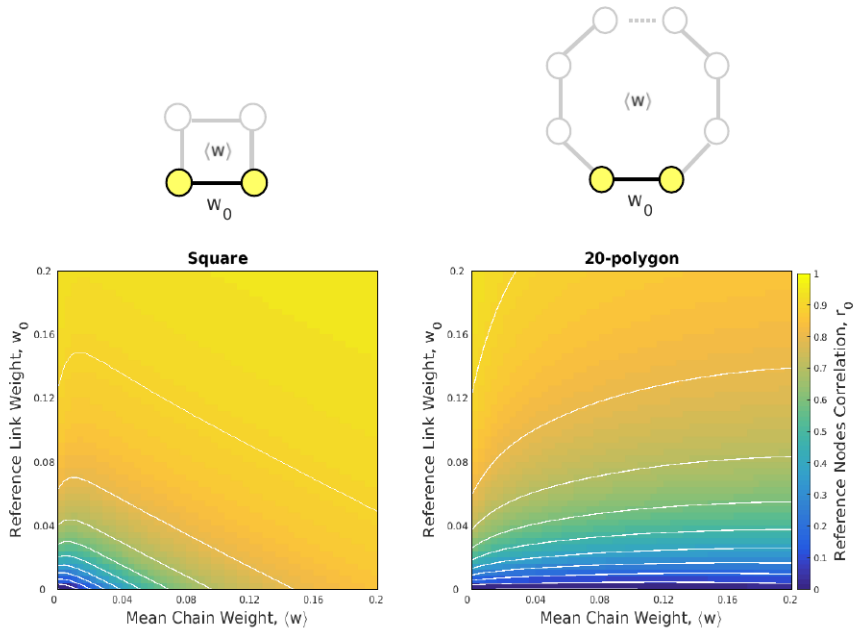

Figure 4.10: Effect of cycles. In order to evaluate the effect that cycles of increasing perimeter exerts on the correlation r_0 between the reference nodes (highlighted in the schematic representation in the top row of the figure) we systematically varied the reference nodes weight, w_0, the length of the chain connecting them, L (in grey), and the mean weight of the links forming the chain, $\langle w \rangle$. All links in the chain will be assigned identical weight, and thus $\langle w \rangle = w$. As for the case of triangular motifs (see Figure 4.9), the panels represent the two most informative examples of the whole 3D parameter space we analyzed, sufficient to understand the complete relationships between w_0, L and $\langle w \rangle$ in determining the correlation between the reference nodes, r_0. The first column represents the effect of a square topology, whereas the second one that of a polygon of 20 edges. The length and strength of the cycle affect r_0 in opposite ways: the stronger the chain, the larger the facilitation in the correlation between the reference nodes (bottom-left panel), which nonetheless dramatically decays when the chain is very long (bottom-right panel).

4.3 Expected covariation

In the previous section we analyzed how very simple network architectures could affect the resulting pattern of correlations observed between a given pair of nodes. Nonetheless, it is important to remember that the network models presented above are nothing more than highly schematic examples, useful to develop an intuition of the covariations they can produce and sustain. To some extent, these are amongst the simplest kind of interactions one can expect in weighted, undirected networks having more than two nodes. In fact, real networks are made of interweaved assemblies of those (amongst others) "topological units", which together form intricate architectures and determine the emergence of complex patterns of interactions. As such, understanding the basic properties of such topological units can be highly informative when it comes to try to understand data obtained from real networks.

According to the results so far, the length of the path connecting two nodes, together with paths redundancy, seem to be two major factors in determining the magnitude of their covariation. Recent work in graph theory (Estrada and Hatano, 2008; Estrada et al., 2012) resulted in determining an accurate measure of the total *influence* exerted by a given node over another node in the network through all possible paths of all lengths, assigning more relevance to shorter ones; this measure of pairwise *communicability* relies on an exponential decay of the influence exerted by longer paths, and can be seen as a generalization of the concept of distance (see Appendix C.7 for a proper description of this measure, denoted as $\mathcal{C}$ throughout the entire thesis). The information summarized by this measure can thus be used to build an estimate of the strength of the covariation that one could expect between two nodes by taking into account the overall similarity of their communicability profiles. To be more specific, if two nodes are connected in similar ways -both with respect to inputs and outputs- with all other nodes in the network, through paths of any lengths (*i.e.* they have similar communicability profiles), it is legitimate to expect that their chances to display similar behaviors will be high; on

the other hand, if the topology of the whole-network communicability between two nodes is very diverse (*i.e.* they have distinct communicability profiles), their expected coupling will likely be weak.

We propose here a novel measure of the *expected covariation* between any pair of nodes in the network, based only on their topological similarity. This measure, that we denoted $\mathcal{T}$ (see Appendix C.8 for a complete description of this measure), compares the similarity of the communicability profiles of different nodes, and as such returns the whole-network topological similarity due to all interweaved paths of any length between every pair of nodes: this measure can thus be reasonably used as a first approximation of the magnitude of the average covariation they will likely exhibit.

A quantification of the topological expected covariation $\mathcal{T}_{ij}$ between node i and node j can be obtained computing the the cosine similarity between the entire i-th and j-th column vectors ($\mathbf{c_i}$ and $\mathbf{c_j}$ respectively) of the communicability matrix $\mathcal{C}$ as

$$\mathcal{T}_{ij} = \frac{\mathbf{c_i} \cdot \mathbf{c_j}}{\|\mathbf{c_i}\|\|\mathbf{c_j}\|}; \tag{4.3}$$

it should be noted that the use of the cosine similarity is not the only possible way to measure the topological expected covariation matrix $\mathcal{T}$, which can in fact be quantified using *any* other measure of similarity between vectors, such as the Pearson correlation coefficient, measures of distance or overlap, as well as more complex derivations. The expected covariation $\mathcal{T}$ can in fact be implemented in different ways, depending on the properties of the network under study (binary, weighted, directed, undirected) and on the particular purpose of the analysis. Being based on the communicability matrix $\mathcal{C}$, this particular formalization of the expected covariation, $\mathcal{T}$, assumes a very simple diffusive process (see Appendix C.8), and as such differences in this measure are mainly determined by differences in the topological similarity between the two nodes of interest. However, it is important to stress that the original idea behind the concept of topological

expected covariation is in no way bounded to a given formulation of communicability: $\mathcal{T}$ can in fact be obtained from any measure quantifying the influence that one node exerts over another node through all paths of all lengths; furthermore, this measure can in principle be applied on any type of system that can be represented as a graph, making the topological expected covariation $\mathcal{T}$ an extremely powerful tool to characterize the whole-system pairwise interactions.

In the following, we will use this measure to try to understand how much of the complex pattern of spontaneous BOLD correlations empirically observed during rest can be actually explained just by the topology of the underlying anatomical structure, and compare the results with a more complex model (the Hopf) which explicitly introduces local node dynamics, in order to gain insight about the contribution of both.

4.4 Understanding empirical data

As stated above, our goal here is to elucidate the contribution that both topological and dynamical factors may have in determining the overall correlation structure observed in canonical resting-state studies. With this in mind, we will now use information about the anatomical structure underlying cortical and subcortical connectivity to obtain, through numerical and analytic procedures, an estimate of the overall pairwise covariation between different brain regions, and then compared these results with the average empirical correlation matrix (R^{emp}) obtained from resting-state fMRI scans of 25 healthy subjects. We will numerically simulate the activity of 68 individual brain regions applying to each of them the local dynamic described by the Hopf model (reviewed in Section 3.7). The connectivity between the 68 regions of interest (ROIs) will be defined using the empirical structural connectivity matrix (SC) obtained through DTI, and we will thus compute the correlation matrix (R^{Hopf}) from the simulated time series. We will use the same empirical SC matrix also to analytically derive the expected covariation matrix

$\mathcal{T}$, that we will employ to quantify the main contribution of the whole-network topology to the pattern of correlations observed in empirical data. It is important to stress that in both cases, we will explicitly interpret the number of reconstructed streamlines between ROIs (stored, after normalization, in the empirical SC matrix), as proportional to the *strength* of their interaction (note that this interpretation of the structural connectivity matrix is not necessarily correct, see *e.g.* Section 1.2.4). The empirical structural connectome, the corresponding correlation matrix and their relationship are depicted in Figure 4.11.

As briefly reviewed in Section 1.3, there exist many graph-measures that can be computed from brain networks, each of them focused on quantifying a particular aspect of their topological structure. Nonetheless, the capacity of those metrics to effectively capture the relationship between the underlying network and the type of interactions that it can generate and sustain varies to a large extent. As an example, we depict in Figure 4.12 the joint clustering coefficient and the weighted assortativity (see corresponding paragraphs in Appendix C) of all nodes' pairs.

Despite their conceptual simplicity, these two measures have been proven to be highly informative of both global and local properties of brain networks (Bullmore and Sporns 2009; Rubinov and Sporns 2010, see also Section 1.3). Indeed, it is possible to appreciate that this measures are clearly able to reveal a structure underlying the organization of overall anatomical connections; on the other hand, the information carried by these metrics is not sufficient to explain the observed pattern of correlations between ROIs. In fact, as we have seen in a previous section (Section 4.2), pairwise correlations are influenced by the overall path structure between the nodes, something that the joint clustering coefficient and the nodes' assortativity are inherently unable to capture. As such, motivated by the informative results obtained from the analysis of different topological motives, we will analyze the influence that the extended path structure underlying the anatomical connectivity exerts on the emerging pattern of correlations, and compared that results with those obtained using the Hopf model, in order to account for the differences that network topology alone

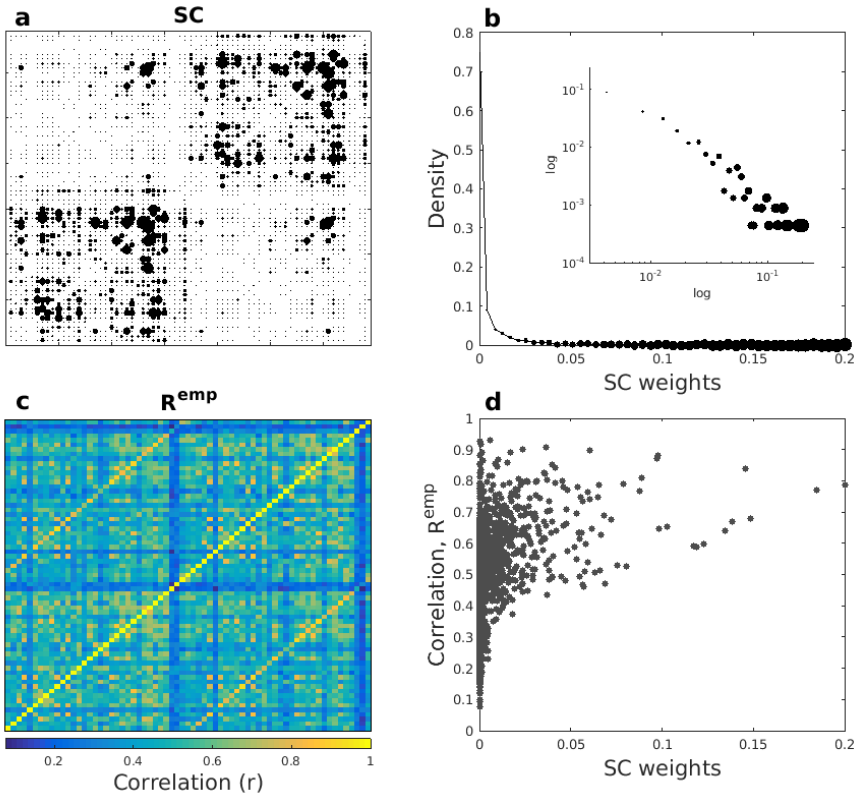

Figure 4.11: Empirical structural and functional data. (a) Structural connectivity matrix obtained from DTI; the size of the dots corresponds to the weight of the connection. (b) Distribution of structural weights. The insert shows the corresponding log-log distribution. (c) Empirical correlation matrix, averaged over resting-state scans of 25 subjects (each scan lasted 10 minutes). (d) Relationship between structural weights and observed correlation coefficients. It is possible to appreciate that the distribution of anatomical links derived from DTI approximate a power-law, meaning that the number of links that are associated with small weights is disproportianlly higher than that of strong ones. In addition, the relationship between the direct anatomical connections and the overall correlation structure is not a simple one: strong anatomical links tend to correspond to high correlation coefficients, but small ones are associated with both small or large correlations. Empirical data kindly provided by Petra Ritter.

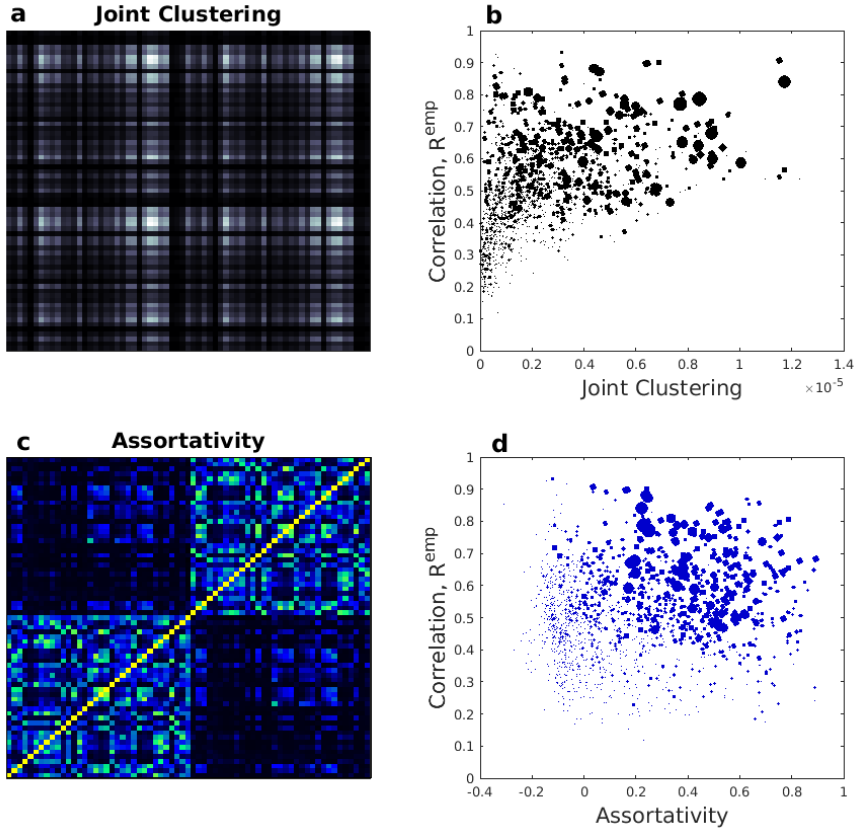

Figure 4.12: Joint clustering coefficient and assortativity. (a) Joint clustering coefficient and (b) its relationship with the empirical correlations between all regions of interest. (c) Node pairs' weighted assortativity and (d) its relationship with the empirical correlations between all regions of interest. The size of dots in both (b,d) corresponds to the weight of the structural link between the corresponding ROIs as determined by tractography. The weighted clustering coefficient is a local measure quantifying the intensity of triangular motifs around a given node, and as such it can be considered as a measure of local integration; the joint clustering coefficient is instead a pairwise measure, obtained multiplying the individual clustering coefficients of the nodes of interest. On the other hand, assortativity measures the similarity of the first neighbors (*i.e.* nodes directly connected) of pairs of nodes, than can be seen as a first rough approximation of their topological similarity; in more precise terms, the assortativity quantify the similarity of the first layer of nodes around two given nodes.

and local dynamics can display in determining the spontaneous co-activations of different brain regions.

The Hopf model and the expected covariation matrix were both optimized according to the global coupling parameter g in order to put the two models in the working regime that best explained the empirical data (see Appendix C.8 for extensive motivations of this optimization procedure). To this aim, we searched for that value of g that returned the smallest Euclidean distance between the values stored in R^{emp} and both R^{Hopf} and $\mathcal{T}$ (which can in fact be treated as a correlation matrix, see C.8). Results are displayed in Figure 4.13, and 4.14.

Both the Hopf model and the expected interaction are able to explain the general structure of empirical correlations with a good degree of accuracy. Indeed, the two models confirmed the existence of a relationship between the size of R^{Hopf} and $\mathcal{T}$ and the strength of the anatomical link defined by the structural connectivity matrix. This relationship closely resembled that displayed by empirical data (compare panel (d) in Figure 4.11 with panels (a,b) in Figure 4.14). It can be also noted that the errors made by the Hopf model are slightly smaller than that obtained from pure topological information (*i.e.* through $\mathcal{T}$), and that these errors also seem to be preferentially localized to controlateral areas (see caption of panels (d,h) in Figure 4.13). Despite the subtle differences, the two models behave very similarly (see panel (c) in Figure 4.14). Other than the inherent incompleteness of the two models, it should be stated that some of the discrepancies between the modelled correlations and the empirical ones could be in part due to intrinsic limitations of the method used to obtain anatomical connectivity: in fact, it is well-known that DTI tend to miss crossing fibers, as inter-hemispheric axons (Jones 2010; Thomas et al. 2014, see also Section 1.2.4), and these weaknesses could lead to accumulate errors.

The results obtained so far indicate that the general pattern of correlations between brain regions observed in empirical data can indeed be explained up to a good extent by explicitly taking into account the information carried by the overall communicability

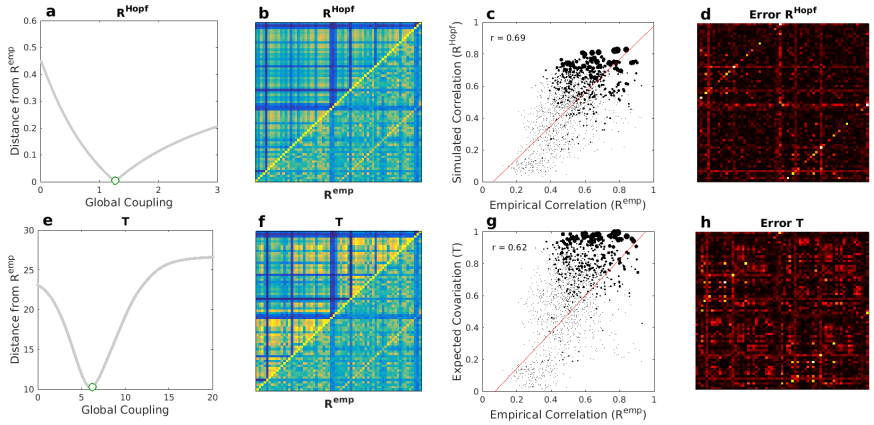

Figure 4.13: Fit between models and empirical data. (a,e) Global coupling g *vs.* euclidean distance between R^{emp} and R^{Hopf} and R^{emp} and $\mathcal{T}$, respectively. The marker corresponds to the value of g that best fits empirical data. (b,f) Comparison of the empirical correlation matrix R^{emp} (lower triangles) with R^{Hopf} and $\mathcal{T}$ (upper triangles) obtained at the best fitting g. (c,g) Scatter plots of empirical and simulated/analytic results. The size of the dots corresponds to the weight of the corresponding links in the empirical structural matrix. (d,h) Matrices of the errors between simulated/analytic results and empirical correlation coefficients. In both cases, errors have been computed as $E = (\hat{y} - x)^2$, where $\hat{y}$ corresponds to either the simulated correlation coefficient r^{Hopf} or the expected covariation $\mathcal{T}$, and x to the empirical correlation coefficient r^{emp}. Homotopic controlateral ROIs corresponds to the second diagonals, clearly visible in (d). Compared to E^{Hopf}, $E^{\mathcal{T}}$ is more homogeneously distributed across the entire network. Nonetheless, globally both models show comparable fits with empirical data.

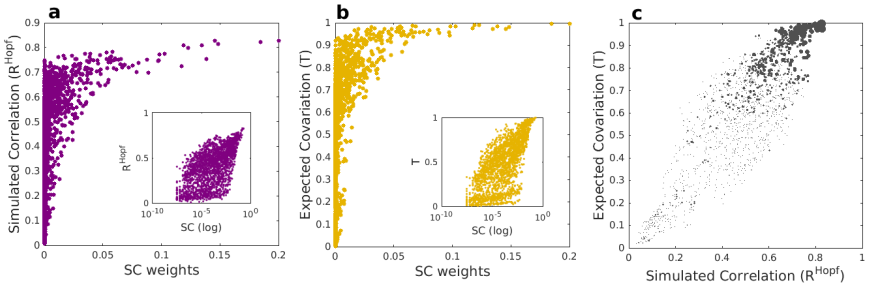

Figure 4.14: Comparison between numerical and analytic results. (a) Relationship between simulated correlation coefficients (R^{Hopf}) and weight of the structural connectome. (b) Relationship between expected covariance ($\mathcal{T}$) and weight of the structural connectome. (c) Comparison between R^{Hopf} and $\mathcal{T}$. The size of the dots corresponds to the weight of the corresponding links in the empirical structural matrix.

sustained by the topological structure of the underlying anatomical connectivity. As such, it would be interesting to ask wheter it is possible to quantify the actual contribution that the whole network exerts on a given pair of nodes, and compare it with that of smaller sub-networks into which that pair is embedded. This would help us understand whether the observed correlation between brain regions is mainly affected by local or by global network effects.

A possible strategy to address this question is to evaluate how the covariation between a pair of nodes changes as a function of the local and the overall topology of the network into which they are embedded. To this aim, we will first select two given nodes (that we will call either *reference nodes* or *reference pair*) and their connection, and evaluate (either numerically or analytically) their pairwise correlation when disconnected from all the other nodes in the network. This corresponds to the simplest two-nodes topology (see Section 4.2.1). After that, we will add one link at a time, accordingly to the empirical anatomical connectivity matrix, untill all links are added. At each step, we will compute the corresponding r^{Hopf} and $\mathcal{T}$ of the two reference nodes selected at the beginning of the procedure: this strategy would allow us to

quantify how very simple and controlled changes could alter the overall topological communicability around a given reference pair as well as their correlation simulated using a dynamical model. As mentioned above, we will use the empirical structural connectivity matrix to select, at each step, the single link that will be added to the previous sub-network, starting from the two reference nodes until all links are added, thus finally leading to the complete empirical SC matrix. This corresponds to adding links according to the "layer" they belong to with respect to a given reference pair (see Figure 4.15 for a schematic representation of the relative layer hierarchy).

The order of links to be added will be set as the following: the first links to be added (one at a time) will be those connected with at least one of the two reference nodes (*i.e.* those belonging to the first layer), from the strongest to the weakest; than, those directly connected to any of the first layer (*i.e.* the second layer's nodes), again from the strongest to the weakest. This procedure will be repeated until all connected links are added (see Figure 4.16 for an illustration of this procedure).

Obviously, this is not the only possible set of rules that can be used to add links. Any particular procedure used to add single links would by definition determine the sequence of links, and thus the change in topology around a given reference pair. We will use the one described above because our aim is to add nodes that are progressively more "distant" from the reference nodes, boths in terms of path length and in terms of exerted influence.

The time needed to perform each individual numerical simulation using the Hopf model makes a complete exploration of all steps for all possible area pairs intractable at the moment, so we will focus on a small but representative subsets of reference pairs. With this in mind, we will select 10 pairs of areas, each of them representative of a different combination of anatomical link weight and quality of the fitting between empirical and simulated correlations; the latter criterion has the advantage of both reducing the probability to focus on just an unrepresentative subset of "good" instances (*i.e.* avoiding "cherry-picking") and, by virtue

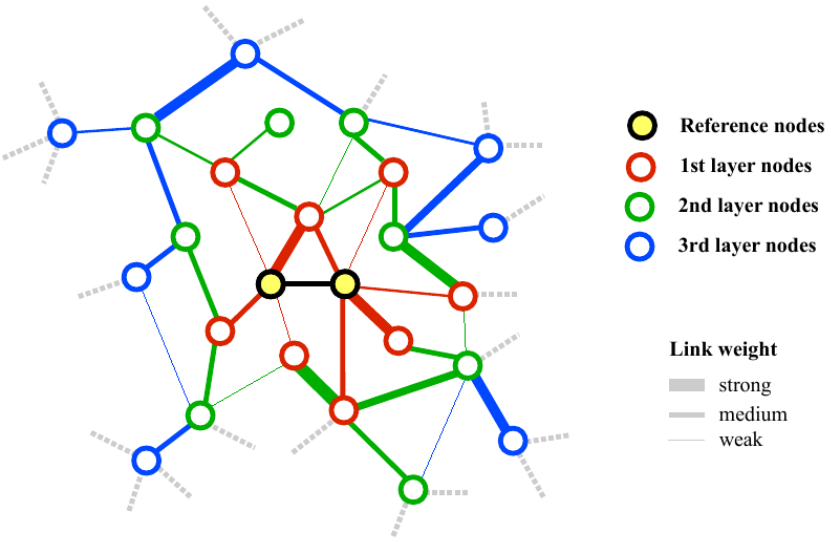

Figure 4.15: Relative network layers. Each node (and each pair) is sorrounded by a different subset of nodes (and links). This subset can be subdivided in layers, depending on the length of the path connecting them with the reference node(s). All the layers of a given node (or pair) determine its extended connectivity profile, *i.e.* the connectivity that it has with all other nodes in the network, both directly and indirectly through paths (where each node and link is visited only once per path, and the maximal path length is $N-1$, being N the number of nodes in the network). As such, each node (or pair) has an associated extended connectivity profile, corresponding to the hierarchy of its sorrounding layers. Two nodes can have identical extended connectivity profiles only if the connection between them (and with themselves, if present) is discarded or identical. In the figure, nodes are marked with different colors according to the layer they occupy with respect to the reference nodes. Nodes in the first layer have direct connections with at least one of the reference nodes (red), nodes (or links) belonging to the second layer are directly connected to nodes on the first layer (green), whereas the third layer is formed by nodes (or links) that connect with nodes of the second layer. The strength of the link is represented by the width of the line connecting two nodes.

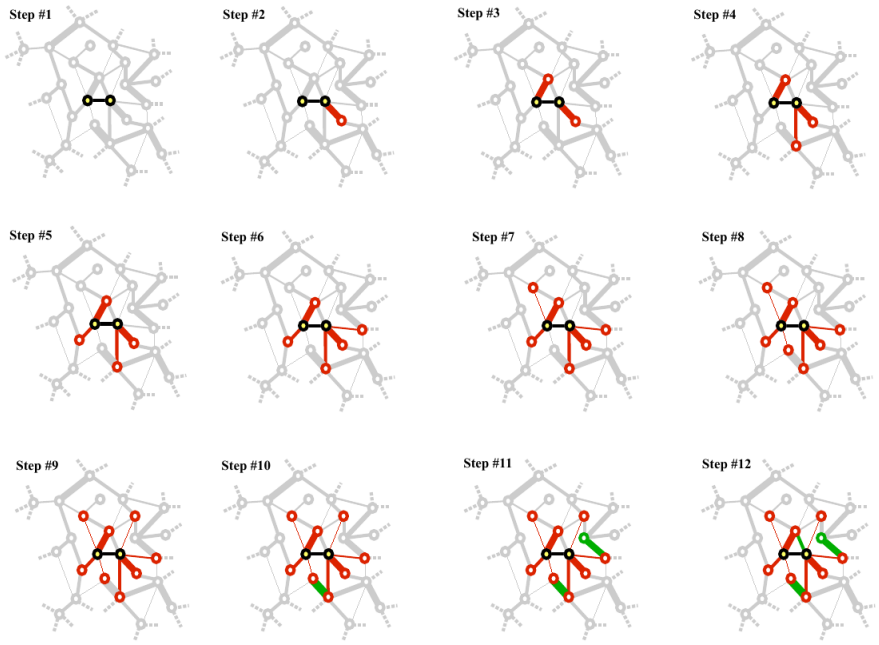

Figure 4.16: Adding link procedure. The figure represents the first twelve steps of the adding procedure explained in the text, adopting the same network architecture used in Figure 4.15. The first step (top-left) corresponds to the simplest topology, the one that considers only the two reference nodes (highlighted), without taking into account all the other nodes in the network (in grey). Each next step is achieved by adding just one link at a time with the corresponding node (unless the node has been already added in a previous step), following the rule that links belonging to inner layers are added first, from the strongest to the weakest (in the figure, steps #2 to #9 correspond to the links in the first layer, in red). When all the links belonging to a given layer are added, links of the following layer are added, one at a time, from the strongest to the weakest (steps #10 to #12, green, in the figure). This procedure continues until all connected links are added. In the present section, we will use this procedure to evaluate how controlled changes in the underlying network topology could affect the correlation between the reference nodes, approximated, at each step, both numerically using the Hopf model and analytically through the expected covariance $\mathcal{T}$. The use of two different methods (the Hopf model and the expected covariance) to approximate the correlation between the seed nodes is motivated by the fact that in the former case the model is based on both the underlying topology and on local dynamics but gave no direct clue about their relative contributions, whereas in the latter case virtually all the information used to approximate the correlation between the seed nodes is based on specific assumptions about the underlying whole-network topology alone.

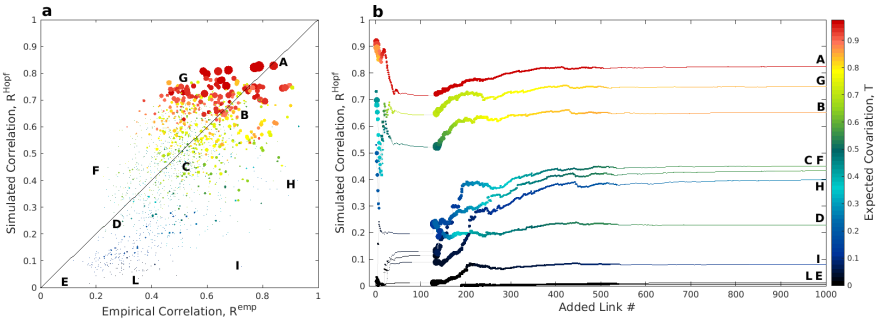

Figure 4.17: Effect of varying topology. Adding individual links affect the resulting correlation between selected pairs of ROIs. (a) scatterplot of the empirical and simulated correlation obtained at the best-fitting global coupling value using the original SC matrix, with highlighted the values corresponding to the 10 selected reference pairs [A-L]. (b) Plot of the simulated pairwise correlations of the 10 reference pairs in (a), computed from networks of increasing size (see text for a description of the link-wise adding procedure). Note that the panel shows just up to the 1000^{th} added link, as the corresponding values of r^{Hopf} do not change anymore after that. In both panels, the size of the dots is proportional to the weight of the corresponding link in the structural matrix, whereas the color indicates the corresponding value of expected covariation ($\mathcal{T}$, see colorbar).

of this, being able to gain insight on the possible sources behind the discrepancies (similarities) between the empirical correlations and those badly (well) predicted by each model. In all cases, numerical and analytical results will be obtained fixing the global coupling value g that gave best-fitting results using the complete original SC matrix (see Figure 4.13). Results are illustrated in Figure 4.17.

All the selected reference pairs converge to their final (simulated) correlation value between the 500^{th} and the 1000^{th} added link: the following added links had practically no effect either on the simulated correlation or on the value of expected covariation. This pattern is due to the adding procedure: we first added links with stronger weights, clearly visible also from the varying size of the dots forming the lines (see captions of Figure 4.17), and as such

it is expected that the last ones to be added would be the weakest, and thus the less influent ones (see general results from the analyzed network models in the previous part of the chapter, Section 4.2). The same reason lies behind the sudden re-appearance of strong links (with associated increase in simulated correlation and expected covariance) around the 120^{th} added link: here is when links of the second layer start to be added. It is impressive to note how tight is the relationship between the simulated correlation and the expected covariation at each step: when added links reduce the topological similarity, $\mathcal{T}$, between the reference nodes, the corresponding simulated correlation , R^{Hopf}, also decreases, and vice versa. This result strengthens the relationship between the two models, and highlights the importance of topological organization in shaping the pattern of co-variation displayed by different areas. Probably the most interesting observation is that not all area pairs behave the same: the correlation between some of them is mainly affected by the presence of a strong direct link between them (*e.g.* A) or by their first neighbors (G,B); on the other hand, that between other pairs is mainly determined by an indirect connectivity sustained by diffuse collective interactions (C-I), wheras the covariation between some other pairs (L,E) remains unaffected (and non-existent, according to both numerical and analytical results).

The present finding confirms that the correlation exhibited by different pairs of nodes is crucially determined by the relative topology sorrounding them, whereas local dynamics seem to play a minor role, at least in this context; furthermore, it indicates that the pairwise correlation between some nodes is largely dependent on more diffuse, peripheral paths shared by both nodes and causing remote synchronization, whereas the correlation between other area pairs is mainly sustained by direct or more local connectivity. As such, is it possible to quantify the relative influence exerted by the network as a whole, and that mainly due to a direct interaction between the two nodes of interest?

A first approximation to answer to this question can be obtained by computing the difference, Δ, between the correlation of the reference nodes obtained when they are disconnected from the

whole network (corresponding to the step #1 in Figure 4.16) and the correlation obtained with the complete network comprising of all nodes and all links. A schematic representation of this measure is given in panel (a) of Figure 4.18.

This measure has both the advantages of being very simple in its implementation, and of requiring only two points per area pair to be computed, thus dramatically reducing the time needed to compute it for all area pairs when each instance has to be simulated several times with models whose execution time is relatively long, as the Hopf model. Furthermore, the interpretation of this measure is also very simple: area pairs with small Δ would be less affected from whole-network effects than pairs having a larger difference. We thus computed ΔR^{Hopf} and $\Delta\mathcal{T}$ for all area pairs. The main results are shown in panel (b,c) of Figure 4.18.

The first observation is that, in general, area pairs with large increase in Δ are those that have weak anatomical connection, as it is possible to appreciate when comparing the two matrices in panel (b), Figure 4.18, with the empirical anatomical connectivity matrix, panel (a) in Figure 4.11. This finding is not surprising, but at the same time not necessary, as there are area pairs that have very small or absent anatomical connection and however are almost unaffected by peripheral diffuse paths (see for example the E^{th} reference pair in Figure 4.17). In addition, the distributions of both ΔR^{Hopf} and $\Delta\mathcal{T}$ suggest a possible bimodality, showing that in general there seem to be two main type of sources of covariation: one is determined by strong direct structural connections (small or negative Δ), the other is instead sustained by diffuse collective effects (large Δ); in the latter case, apparently the two areas can be connected by either weak or stronger links. This findings confirmed that one of the most important factor in determining the strength of the correlation between two nodes is indeed the presence of a strong structural link connecting them; nonetheless, they also highlight the crucial relevance of indirect influences and paths redundancy to understand the overall pattern of covariations observed in empirical data.

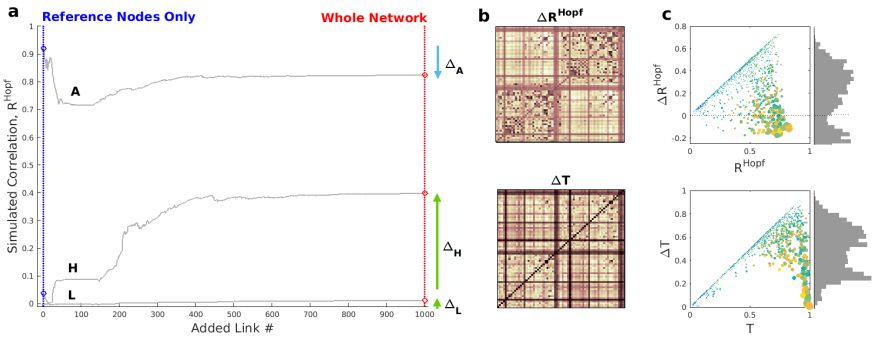

Figure 4.18: Quantification of whole-network contribution. (a) Schematic representation of the logic behind Δ, exemplified on the R^{Hopf} of three reference pairs characterized by different behaviors [A,H,L]. Δ_A show that whole-network influence has the effect of decreasing the strength of the correlation that the two nodes of the reference pair would have displayed alone; The H^{th} reference pair shows a big dependence on whole-network effects, as mirrored by the substantial increase in Δ_H, whereas that of L is minimal. The whole-network effect, Δx, of a given reference pair is computed as $\Delta x = x^1 - x^{end}$, being x either the simulated correlation r^{Hopf} or the expected covariation $\mathcal{T}$, obtained at the first (x^1) and last (x^{end}) steps of the adding link procedure. It should be noted that $\Delta\mathcal{T}$ took only positive values, whereas ΔR^{Hopf} displayed both positive and negative ones. (b) Δ matrices obtained from R^{Hopf} (top) and from $\mathcal{T}$ (bottom). Lighter color corresponds to a larger whole-network dependence of the corresponding seed nodes correlation. (c) Relationship between the simulated correlation R^{Hopf} computed from the full-network and its corresponding ΔR^{Hopf} (top), and the expected covariance $\mathcal{T}$ computed from the full-network and its corresponding $\Delta\mathcal{T}$ (bottom). In both panels, the size of the dots is proportional to the weight of the corresponding link in the anatomical connectivity matrix, whereas the color to the corresponding empirical correlation. The diagonal cut in the two figures in panel (c) correspond to the upper bound of each Δx, given by $max\Delta x = 1 - x^1$.

4.5 Conclusions

In the present chapter, we analyzed the contribution that whole-network topology exerts on the emerging overall correlation structure. The analysis of the correlation generated and sustained by distinct topological units, the building blocks of larger networks, helped us elucidating what are its main determinants, highlightening the importance of short paths and redundancy.

This step was fundamental to conceive and construct a novel measure, that we called topological *expected covariation*, $\mathcal{T}$, reflecting the size of the pairwise covariation that one could expect just by virtue of the similarity between the communicability profiles of any pair of nodes in a network. This measure builds upon the findings that shorter paths tend to drive larger covariations, but that the final covariation between the activity of any pair of nodes does not necessarily depends on just the shorter paths between then, but have to be understood in terms of all the interweaved paths crossing and interacting with each other, forming the fundamental topological skeleton of any network. This intrinsic property generate a cascade of mutual interactions that, despite their complexity, can be estimated analytically through simple formalizations, thus making $\mathcal{T}$ a powerful tool to summarize and understand the higher-order interactions emerging from even simple topologies.

We finally applied this measure to empirical data, finding that pure topological information can in fact predict the spontaneous correlation structure observed during rest as good as a more complex phenomenological model based on both the anatomical connectivity and local nodes dyamics. Finally, we were able to demonstrate that not all pairwise intrinsic correlations are driven by the same factors: in fact, despite the larger correlations are, as expected, mainly due to strong anatomical connections, other brain areas tend to correlate due to more general network effects determining remote synchronization, and that could mirror polysinaptic routes.

As always, any answer leads to new questions, and open new

doors. For example, can we use the information obtained with $\mathcal{T}$ to make some informed guesses about false positive and false negative fibers detected (or not) using diffusion tractography? In addition, it is likely that the information used to obtain $\mathcal{T}$ should in principle be used to detect network modules, or to determine the functional roles that different nodes play both on the global network level and on local interactions. The expected topological covariation can also be used to evaluate how different states modulate the structure-function relationship, in terms of how far the influence of different nodes spread through the network; this can in principle be explored also using different models, but the advantage of $\mathcal{T}$ is that it is explicitly based on clear assumptions about the structure-function relationship, which in turn allows both to test specific hypotheses, and to ease interpretations. Ultimately, another aspect that we will investigate is about the capacity of this measure to predict global and local responses to network structural perturbations, which can in turn be extremely useful both in clinical neuroscience as well as in other field of applied network science.

Chapter 5

General discussion

"Apparently, the isomorphisms of laws rest in our cognition on the one hand, and in reality on the other."

L. von Bertalanffy

"The ideal scientist thinks like a poet and works like a bookkeeper."

E. O. Wilson

What have we learned so far? After reviewing the state-of-the-art findings and tecnhiques focused on the study of brain spontaneous activity (see Chapter 1), we demonstrated how a transient manipulation of the regional dynamics, obtained through anesthesia, massively alters the overall landscape of spontaneous activity (see Chapter 2). Induction of a deep state of anesthesia not only determines a global net decrease in the correlation between brain areas (as measured with fMRI), but also the destructuration of those large-scale networks classically found during light sedation

and the awake state. In the anesthetic mixture used, medetomidine acted primarily as an analgesic -whose concentration was in fact maintained constant during all the recording-, whereas the concentration of ketamine progressively decreased due the ongoing metabolism. The anesthetic effect of ketamine is mainly (but not uniquely) due to its antagonistic binding to NMDA receptors (Quibell et al., 2011), which interfers with their normal functionality. This in turn obstacles proper synaptic efficacy and inter-neuronal coupling, thus decreasing the probabilities of forming larger assemblies displaying sustained co-ordinated activations. On a macroscopic scale, this drives the entire system toward more uniform and stereotypical dynamics, corresponding to a dramatic reduction in functional complexity. The widespread effects of anesthesia, despite affecting the integrity of the general correlation structure, does not lead to pure stochastic activity: in fact, local connectivity seems to be partially preserved, exemplified by sustained power correlations in the α range between areas belonging to the same functional network, and possibly mirroring the existence of strong underlying anatomical connectivity. The progressive fading of the anesthetic effect is associated with the gradual restoration of synaptic function, reflected in increased structured co-activations and leading to the progressive re-appearance of intrinsic functional networks.

The findings of the second chapter, whose detailed analysis is to date unique of its kind, illustrate the enormous effect that experimental manipulations of the local dynamical properties alone can exert on the behavior exhibited by the entire system. We thus moved to the next question.

How much does the topology of the underlying anatomical connections determine the spontaneously emergent correlation structure? To try to answer this question, we simulated brain spontaneous activity while manipulating its topology, and evaluating how much these changes affect the observed correlations. As such, we first briefly reviewed different models of brain activity (see Chapter 3), from biophysically realistic to phenomenological ones, and introduced the Hopf model, that has been recently shown to approximate the pattern of spontaneous correlations

seen during rest (Deco and Kringelbach, 2016).

In the last chapter (Chapter 4), we used the Hopf model to evaluate the effect of network topology in shaping the emerging functional structure. With this in mind, we started quantifying how simple topologies affect the correlation between a given pair of nodes embedded in that network, and we isolated a few, simple factors determining the emerging correlations and able to generate non-trivial behaviors, such as remote synchronization. Our results, in accordance with the previous literature, showed that these factors are the strength of the connections, their number, the distance between nodes and the presence of redundant paths, being the relative importance of each one of them dependent on the topology of the overall network to which they participate (Watts and Strogatz, 1998; Barabsi and Albert, 1999; Gómez-Gardeñes et al., 2007; Arenas et al., 2008; Goñi et al., 2014). Recent work showed how the presence of multiple paths of varying length -referred to as *path ensembles*- increases brain network resiliency (Avena-Koenigsberger et al., 2016), thus demonstrating the crucial importance of path redundancy. In the fourth chapter, we moved forward and used the information gained from these toy networks to build a simple function that links topological information (derived from the underlying structure of the network) to the emergent correlation structure. We denoted this function of the *expected covariation* based on topology as $\mathcal{T}$, and used it to predict, with good accuracy, the average correlation structure observed in empirical resting-state data. This function quantifies the similarity between the complete topological profiles of any pair of nodes, incorporating all the interweaved paths existing between them, and has revealed itself to be a very good indicator of the arising average co-variation, hence its name. Indeed, this novel function can be used to approximate the total "influence" that any node in the network exerts on any other node through all possible paths of any length, thus offering a clear understanding of the extraordinarily strong bond between structure and function. We finally applied this novel analytical measure, together with numerical simulations obtained using the Hopf model, to assess how small changes in the topological structure around given nodes

affect their covariation, discovering that the pairwise activity of different brain regions is determined by either local interactions, or driven by diffuse whole-network effects.

It is important to remember that both the Hopf model and the expected covariation make use of the topological information carried by the anatomical connectivity matrix, whereas only the Hopf model explicitly introduces non-trivial local dynamics. The topological covariation, even if conceptually based on the approximation a simple decay process (through the use of the communicability matrix $\mathcal{C}$, Estrada and Hatano 2008), cannot be considered a dynamical model, and does not generate simulated signals. Therefore, the finding that, in general, both models appear to explain empirical data equally well, suggests that the average correlations computed across subjects seem to be mainly driven by the underlying brain topology. Nonetheless, as mentioned in the end of Section 1.2.2, the correlation between distinct area pairs is not a static object, but exhibits time-varying fluctuations, whose mechanism can only be captured through the use of dynamical models.

Altogether, our findings demonstrate that both local dynamics and network topology shape ongoing brain activity, but what is their precise relationship? It is indeed very tight. Interpreting Aristotles' views, medieval philosopher Tommaso d'Aquino (1225-1274) wrote that "the container shapes the content" (*quidquid recipitur ad modum recipientis recipitur*). More recent works (Strogatz, 2001; Wang, 2002; Boccaletti et al., 2006; Newman et al., 2011) together with the results presented in this dissertation, suggest that even if structure is indeed a major determinant, the information it provides alone is not sufficient to fully explain the particular behavioral state that a system display in a specific moment; putting it simply: the normal transition from sleep to wake is not triggered nor explained by structural changes. In fact, *the geometrical properties of a system bound the space of the possible emergent activity patterns that it could sustain, whereas the dynamical local properties of its elements determine the actual region of this space in which the system lies.* Global state chages, such as the transition from deep to light anesthesia, or

from NREM sleep to the awake state, can thus be viewed as system excursions to different regions of this space, driven by changes in the local dynamics; global state transitions can also be due to changes in the topological properties of the underlying network, that will shrink or expand the space of possible behaviors that the system can display, as for example after a stroke or, on the other hand, during normal development and learning: in either case the system has undergone structural -thus, topological- changes with respect to its previous state.

As mentioned above, our analysis of how much anatomical topology sculpts the emerging correlation structure of ongoing brain activity led us to develop an original function, $\mathcal{T}$, that quantifies the similarity of the whole-network communicability profiles between any pair of nodes in a graph (see Section 4.3 and Appendix C.8). By definition, this measure is based on the *structure* defining the graph, and expresses the affinity between the complete patterns of structural interactions that two elements of the system have with all the rest of the network in which they are embedded. What is remarkable is that this simple measure of structural similarity has revealed itself to be a very good approximation of the average correlation structure displayed by the analyzed empirical data, as good as a more complex dynamical model. During the next months, we will further investigate in deeper detail this very interesting aspect, and try to analytically explicit the relationship between $\mathcal{T}$ and the average correlation, $\langle R \rangle$. If proven true, this would imply that knowledge about the topological structure of a network should in principle be enough to predict its average correlation structure.

To save a few lines for speculations, this would also be in accordance with the classical observation that, in biology, structure largely determines function, as exemplified by RNA or proteins (Monod, 1974). If we consider *structure* as the entire pattern of direct bonds between all the elements of a system, it does not seem unreasonable to believe that this tight link we repeatedly observe between structure and function should mirror some kind of logical necessity, a simple but fundamental universal principle underlying any emergent property. In fact, could we even think

of a case in which the emerging function of an object is entirely independent of its structure?

Part I

Appendix

Appendix A

Notes on the origins of spontaneous brain activity

> "Everything is what it is because it got that way."
>
> D'Arcy Wentworth Thompson

As we repeatadly advised, one should be careful when trying to interpret the spatio-temporally organized fluctuations spontaneously emerging during rest (see Chapter 1), especially with respect to their putative function. Do intrinsic activity as measured at different spatial and temporal scales reflect different functions? And if it is the case, what functions? Is it possible that certain frequencies do reflect genuine neuronal computations, whereas other mirror more widespread systemic processes (either neuronal or not)? To understand the functional role of the ongoing modulation of intrinsic brain activity it is vital to study its origins. What are the endogenous physiological processes driving spontaneous activity? Following a reductionsit approach, it is legitimate to search for the origin of spontaneous fluctuations observed in

ongoing activity in the properties of both single neurons and neuronal circuitry.

Soon after the seminal work of Hubel and Wiesel (Hubel and Wiesel, 1959), it was shown that neighboring neurons having similar receptive fields tend also to exhibit spontaneous correlated activity, whereas neighbors with complementary receptive fields don't (Arnett, 1978). The presence of an organized functional architecture was observed also in a computer compartmental model of the CA3 region of the hippocampus, where the emergent rythmic activity was produced and sustained by intrisic cellular properties and the connectivity and strength of excitatory and inhibitory synapses (Traub et al., 1989). Observation of spontaneous depolarizations of subthreshold membrane potential (Steriade et al., 1996) and the presence of alternating activity due to intrinsic membrane properties (Wilson and Kawaguchi, 1996) were followed by experimental and computational evidences demonstrating that neural assemblies are able to synchronize their subthreshold activity, leading to fixed shared states that allow for rapid collective state transitions (Makarenko and Llinás, 1998). With the aim to understand the generation of spontaneous low frequency (<1 Hz) oscillations observed during sleep, Timofeev and colleagues (Timofeev et al., 2000) simultaneously recorded, in the anesthetized cat, the ongoing activity both from neurons in small deafferented cortical slabs and from adjacent intact sites outside the isolated region, finding that slow oscillations where preserved only in the latter; however, isolated slabs exhibited short periods of activity separated by long silent periods. Interestingly, the authors found that enlarging the isolated region increased the probability of initiating large-scale activity within the deafferented slab, in accordance with computer models and supporting the hypothesis that intrinsic currents could amplify incoming signals, more frequent in larger networks. Similarly, Cohen et al. (2008) showed the emergence of spontaneous network activity in hyppocampal neurons grown in cultures. The size of the neural assembly was a major determinant of its collective properties: large networks became rather unsensitive to the firing activity of a single neuron, and as such spontaneous synchronous

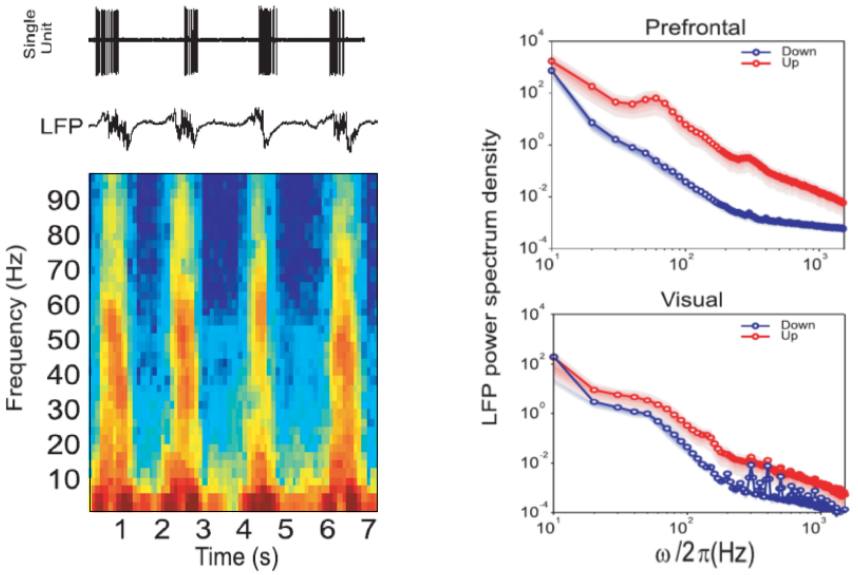

Figure A.1: Up and Down states observed in the anesthetized mouse. (Left) Single-unit recording, LFP trace and spectrogram showing the alternation between fast activity ("Up") and silence ("Down") in prefrontal cortex. (Right) Power spectra of prefrontal and visual cortex after separation of "Up" and "Down" periods. Panels adapted from Ruiz-Mejias et al. 2011.

bursting could be triggered only by at least several local subthreshold synaptic events. On contrary, small networks did not displayed spontaneous bursting, but experimental manipulation of the activity of a single neuron could indeed produce a network discharge. Furter studies demonstrated that the slow alternation (<1 Hz) between periods of activity and silence (referred to as "Up" and "Down" states, respectively. see Figure A.1) observed *in vivo* on the cortex both during sleep and under anesthesia (Ruiz-Mejias et al., 2011) is in fact generated through recurrent excitation, and modulated by inhibitory networks (Sanchez-Vives and McCormick, 2000; Compte et al., 2003).

Multineuronal recordings often reveal the presence of synchronized spontaneous spiking activity in different neurons. Through

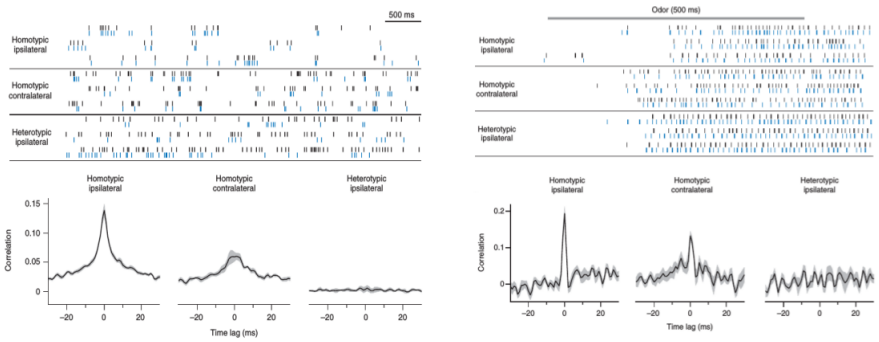

Figure A.2: Spike correlations in spontaneous and evoked activity. (Top) Raster plots of three different groups of neurons and (Bottom) corresponding cross-correlograms. Panels on the left represent correlated spike timing observed during spontaneous activity, whereas panels on the right that measured during the presentation of an olfactory stimulus. Homotopic ipsilateral neurons are monosynaptically connected, homotopic contralateral are not connected but receive input from the same population of neurons, whereas neurons belonging to different functional pools (heterotopic) do not connect directly with each other. Panels adapted from Kazama and Wilson 2009.

genetical labelling of olfactory neurons of the Drosophila antennal lobe, Kazama and Wilson (2009) demonstrated that both direct anatomical connectivity and incoming projections from a common source determined the correlation strength of their ongoing spiking activity: as such, some neurons exhibited spontaneous correlated activity, while others don't. Interestingly, the actual presence of a stimulus increased the correlations between those neurons that previously exhibited spontaneous coupling, but not those of spontaneously uncoupled ones, highlightening the tight relationship between anatomical connectivity and functionality (see Figure A.2).

Anatomical connectivity in fact plays a crucial role on intrinsic activity, as demonstrated by the finding that regions linked by long-range monosynaptic connections exhibited correlated hemisphere-wide patterns of spontaneous and sensory-evoked depolarization

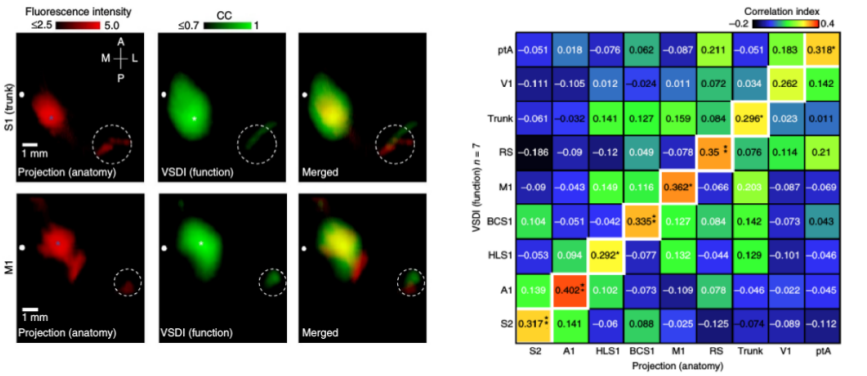

Figure A.3: Axonal projections and spontaneous cortical correlations. (Left) First column: axonal projection maps (pixel intensity is logarithmically scaled). Second column: seed-pixel correlations obtained from VSD imaging. Third column: spatial colocalization of axonal projection and seed-correlation maps. Blue and white stars correspond to the site of the tracer injection and the pixel used as seed, respectively. (Right) Matrix of the similarity between VSD correlations and axonal projection maps for nine cortical regions. $*$ <0.05, $**$ <0.01 one-way ANOVA. Panels adapted from Mohajerani et al. 2013.

(Mohajerani et al. 2013, see Figure A.3): the authors suggested that the intracortical monosynaptic connectome can thus shape the flow of spontaneous cortical activity.

Recent evidences, to date uniques of their kind (Richiardi et al., 2015), showed that the spatial organization of brain tissues expressing similar pools of genes resembled that of four RSN rather well characterized in the imaging literature (Figure A.4).

Despite the high complexity of the whole procedure, which has to be aknowledge in cautiously interpeting the results, the authors found that tissues of brain samples obtained from regions that have been associated with the same functional network exhibited higher genetic correlation than samples obtained from regions assigned to distinc networks. After having obtained a consensus list of 136 genes responsible for the relationship between

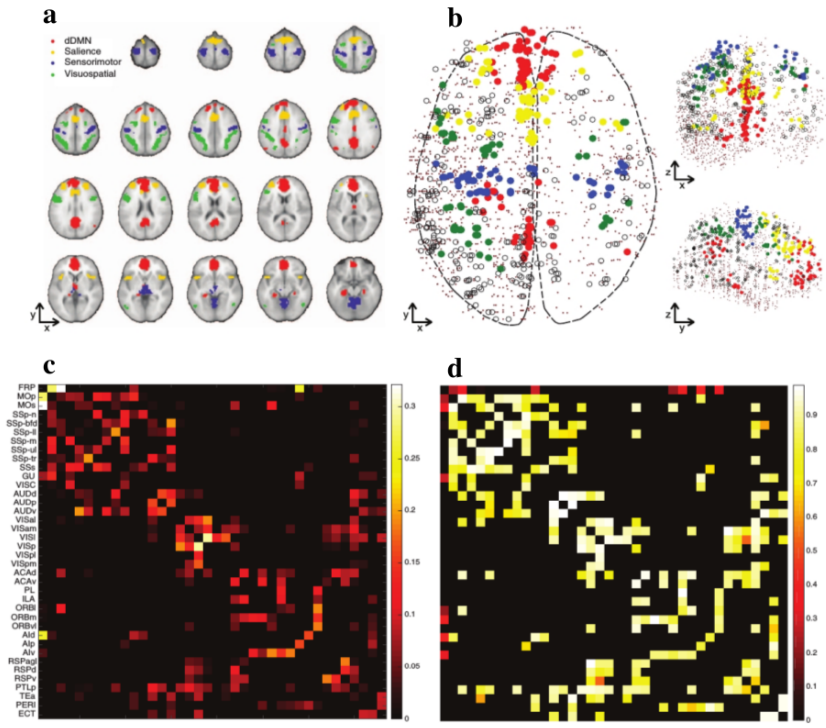

Figure A.4: Genetic contribution to anatomical and spontaneous connectivity. (a) The four functional networks used to compare with genetic data. (b) Human brain tissue samples assigned to their corresponding functional networks. Coloured circles are samples assigned to the four networks used in the analysis, open circles those assigned to other networks, dots corresponds to samples left unassigned. Only four networks were used in the analysis, as the other nine did not have enough samples each to make statistically meaningful claims. Samples were assigned to a certain network both depending on their spatial location and due to the transcriptional similarity of the tissues sampled. The subdivision of all samples in the presented groups (13 in total, one *per* functional network) was that returning the highest within-group transcriptional similarity (significance was assessed randomly reshuffling the sample-to-network assignment). (c) Ipsilateral axonal connectivity matrix derived from the Allen Mouse Brain Connectivity Atlas. (d) Transcriptional similarity (genetic correlation). Panels adapted from Richiardi et al. 2015.

gene co-expression and functional networks, the authors demonstrated that common polymorphisms (*i.e.* variants of the same gene) in the consesus genes were related to the individual variability of the strength of functional networks measured on 259 subjects. The authors then extracted from the consesus list 57 mouse orthologs (*i.e.* genes whose function is the same in different species), and then computed the transcriptional similarity of this subset of genes in 38 brain samples obtained (ipsilaterally) from the mouse brain. This procedure allowed Richiardi and colleagues to show how the resulting overall genetic correlation matrix between the selected brain samples matched with the information about anatomical connectivity between the corresponding regions and derived from retrograde tracers. The similarity between the two maps suggests that brain regions expressing similar genes also tend to be anatomically connected through monosynaptic pathways. When analyzing the ontology (*i.e.* the function(s) of the protein a gene codes for) of the genes in the consensus list, the authors found that their principal functions were related to molecular mechanisms of ions transport and cellular components. The remarkable observations made by this study shed light on some of the putative mechanisms behind the generation of the highly organized pattern of intrinsic fluctuations systematically observed in humans and other animals, and suggest the existence of a general "assortativity principle" based on the similarity between the membrane properties of neurons and guiding their anatomical connectivity to form functional networks.

Spontaneous fluctuations are not only exhibited by the mature CNS, but growing evidences underline the fundamental implications of spontaneous activity in scaffolding the proper functional architecture of the developing brain. In fact, ongoing spontaneous neuronal activity has been observed in many parts of the developing nervous system. Of special relevance are the high excitability of developing networks with recurrent connectivity and the presence of transient depressions induced by activity (O'Donovan, 1999). Intrinsic rhythmic activity of developing networks plays in fact an important role in the organization of mature circuitry.

In 2004, Yvert and colleagues (2004) demonstrated that during the development of the mouse spinal cord, spontaneous activity became progressively more complex (*i.e.* exhibiting an increasing repertoire of ryhthms) as the embryo grows. The long and diffuse spontaneous events characterizing early stages of the spinal cord development get substituted by more irregular and localized ryhthms, until the originally fully synchronized network progressively segregates into more locally specialized sub-networks, an exemplary feature of topological complexity (Zamora-López et al., under review). This propagating waves observed during early stages of development tend to be generated by the spontaneous activity of multiple neuronal populations which are widely distributed across the entire CNS, although the spinal cord seems to play a predominant role at this stage (Momose-Sato et al., 2007). In rat, intrinsic activity of neurons in the early auditory system is triggered by supporting cells that spontaneously release ATP, which in turn depolarize nearby neurons increasing the probability of localized bursts of activity between neighbors, thought to be responsible for the maintenance and refinement of tonotopic maps (Tritsch et al., 2007). In a recent study, Ahrens and colleagues (2013) genetically modified zebrafish larvae to express an indicator of calcium activity, and recorded the spontaneous activity of the entire organism using ligh-sheet microscopy, which allowed to record more than 80% of all neurons at single cell resolution (Figure A.5). The authors were able to identify two neural populations exhibiting correlated spontaneous activity, thus revealing the progressive differentiation of neural activity during development.

The evidences reviewed so far suggest that spontaneous brain activations are an inherent feature of brain functioning, mirroring both the intrinsic properties of individual neurons and their connectivity. Furthermore, they seem to be functionally relevant, associated to very fundamental principles of brain development and organization. It has indeed been shown that intrinsic neural activity during development lies at the basis of network formation and homeostasis (Katz and Shatz, 1996; Turrigiano and

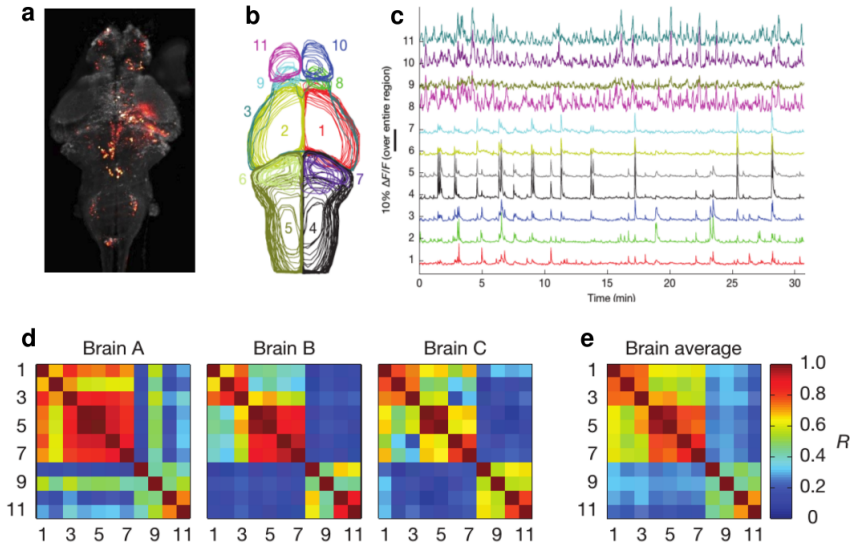

Figure A.5: Spontaneous activity in the zebrafish larva. Correlations and spontaneous activity patterns across brain regions of the zebrafish larva. (a) Whole-brain calcium imaging of neuronal activity at cellular resolution. (b) Manual segmentation of brain regions. (c) Fluorescence ($\Delta F/F$) traces in each brain area of (b). (d) Correlation matrices of brain area activity for three fish (Brains A, B and C). (e) Average correlation coefficients (R) of six fish. Adapted from Ahrens et al. 2013.

Nelson, 2004; Sur and Rubenstein, 2005), and that spontaneous activity is able to modulate dendritic spines number and structures, pretty much as evoked activity does (Trachtenberg et al., 2002; Sur and Rubenstein, 2005). In addition, experimental evidences demonstrated that a lack os spontaneous activity tend to lead to a progressive decrease in the number of dendritic spines connecting neurons, which in turn determine the triggering of apoptotic processes ending with neuronal death (Fishbein and Segal, 2007). Coordinated intrinsic activations may thus be (at least in part) related to the establishment and the maintainance of synaptic connectivity, crucial to sustain proper functionality of the individual neurons and, as such, of the entire organism.

Being so fundamental, it is thus to expect that these principles should be conserved across species, with rather small differences between phylogenetically closed species. It is also not surprising that such spontaneous activations are not completely suppressed in different states such as sleep or anesthesia, but simply modulated. It is thus legitimate to think that substantial deviations from the highly conserved core of spontaneous co-activations, triggered by many possible factors, could be associated with (or even lead to) a diverse range of pathological conditions, that have in fact been linked with abnormal resting-state properties (Greicius et al., 2007; Kennedy and Courchesne, 2008; Whitfield-Gabrieli et al., 2009). On the other hand, it is reasonable to think that physiological variability should also be present on top of an overall preserved functional skeleton, and that slight changes in that may be associated with normal individual differences.

Appendix B

Supplementary Materials

This chapter reproduces the Supplementary Materials of the published paper Bettinardi et al. (2015), presented in chapter 2.

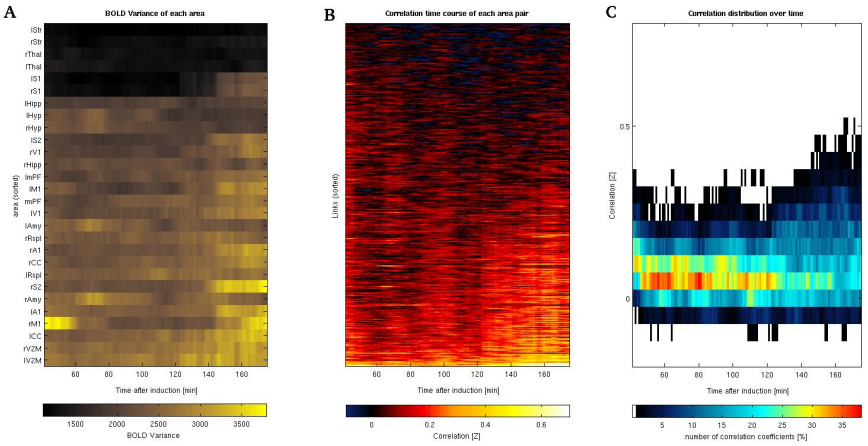

Figure B.1: fMRI: Gradual changes in signal variability and FC as anesthesia naturally fades out. (A) BOLD variance over time in each area. All areas has been sorted depending on their mean value across time. (B) Correlation time course of each link (*i.e.*, each pair of areas) under different levels of anesthesia. Links has been sorted depending on their mean value across time. Pearson's linear correlations were converted to the corresponding Fisher's z-score (see Materials and Methods 2.3). (C) Distribution of all correlation coefficients over time. First phases of anesthesia are characterized by more symmetrical distributions centered around low correlation values, whereas while the effect of anesthesia progressively decreases, the percentage of links showing higher correlations raises.

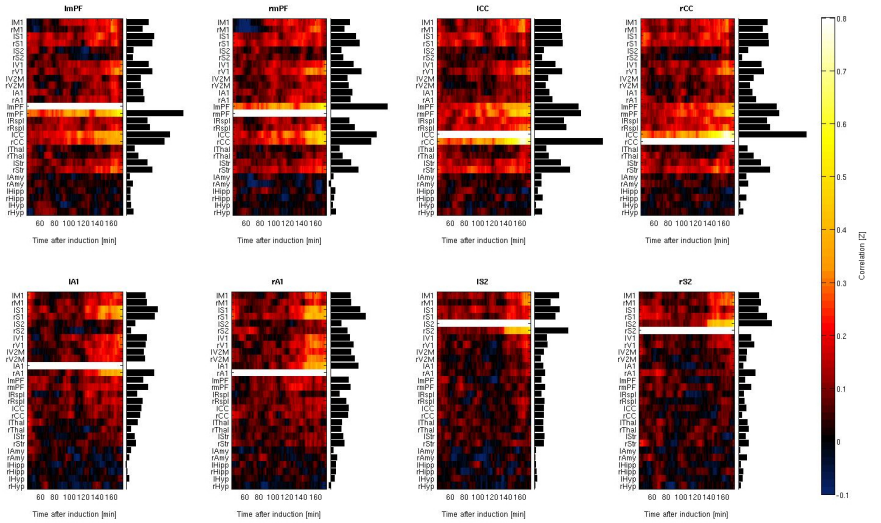

Figure B.2: Individual FC time courses of a subset of cortical ROIs. Each panel depicts the functional connectivity time course of a given cortical area with all other areas, computed from 90% overlapping sliding windows of 10 minutes. The horizontal bars on the right of each panel represent the mean pairwise correlation between the ROI and all other areas calculated across all the recording, and emphasize which are the preferred subset of regions that exhibit the highest correlations with a given area over all protocol time. A first feature that is possible to appreciate is that contralateral ROIs show increased correlation as the effect of anesthesia gradually vanishes over time, being its value among the highest ones, where not the highest itself. In addition, these analysis strongly suggest the presence of an underlying correlation structure, which become clearer as anesthetic effects gradually fades out over time. Indeed, cortical regions exhibit the tendency to cluster preferentially with different subsets of other regions, as exemplified by mPF and CC, which seem to take part to the same functional cluster (top panels), and by A1 with S1 and V2M (bottom-left panels) and by S2 with primary sensory (S1) and motor (M1) cortices (bottom-right panels).

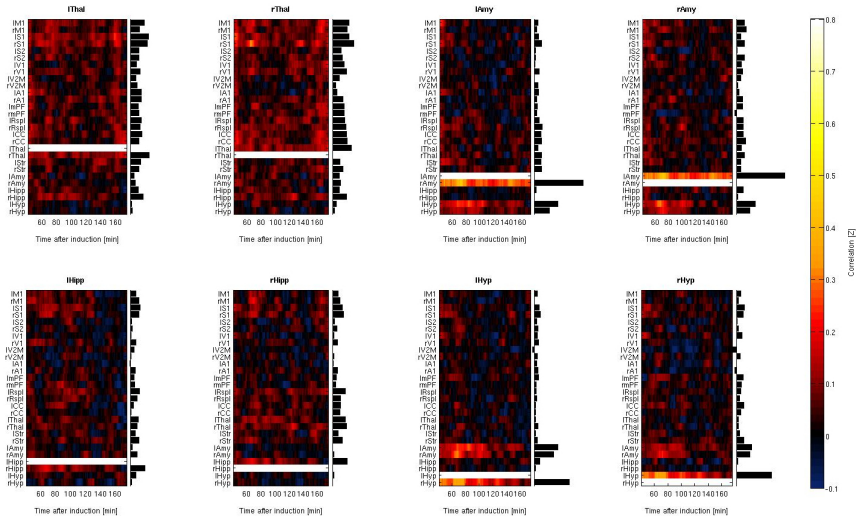

Figure B.3: Individual FC time courses of a subset of subcortical areas. Each panel depicts the functional connectivity time course of a given subcortical area with all other areas, computed from 90% overlapping sliding windows of 10 minutes. The horizontal bars on the right of each panel represent the mean pairwise correlation between the ROI and all other areas calculated across all the recording, and emphasize which are the preferred subset of regions that exhibit the highest correlations with a given area over all protocol time. Subcortical areas tend to show overall lower correlations with other areas than cortical ones. Interesting is the temporal pattern of coactivations within and between the amydgalas and the hypothalami (top-right and bottom-right panels), which (after a first increase during deeper stages of aneshesia) is decreasing, whereas most of cortical areas (see Figure B.2) and to some extent the thalami (top-left panels) exhibit increasing functional connectivity over time.

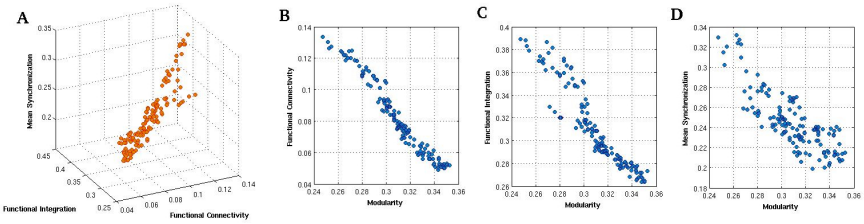

Figure B.4: Scatterplots of variables measuring different aspects of functional dynamics. (A) Three dimensional scatterplot of the FC, functional integration and mean synchronization time courses. It is possible to see that, as expected, the three variables are highly correlated. Pairwise correlation between FC and functional integration is 0.9596, that between FC and mean synchronization 0.8069 whereas between functional integration and mean synchronization is 0.8009. (B) The relationship between Modularity Q with the three measures plotted in panel A confirms that this metric conveys complementary information with respect to the others. Pairwise correlation between Modularity and FC is in fact - 0.9775. (C) Correlation between Modularity and funcional integration is 0.9370. (D) Correlation between Modularity and mean synchronization is 0.8182.

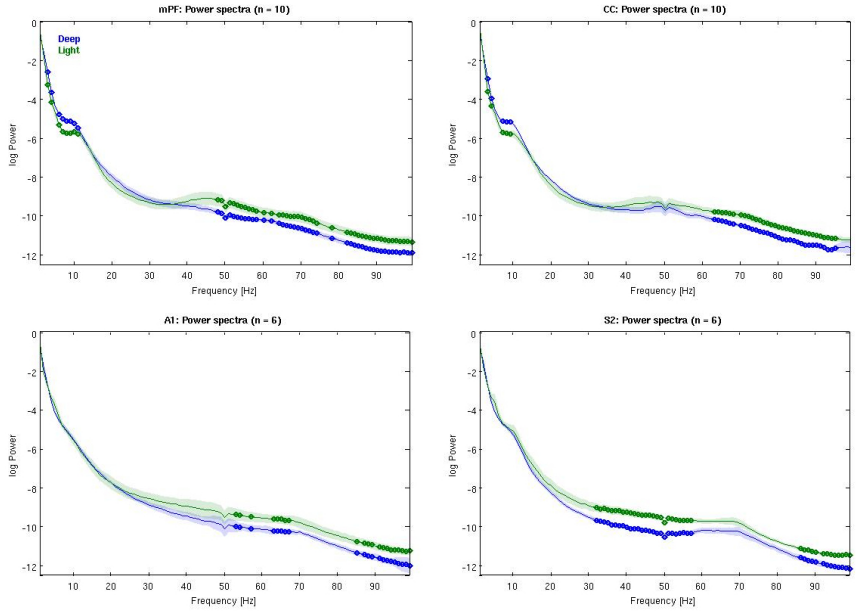

Figure B.5: Ketamine/medetomidine modulation of the power spectra in deep and light intervals. Empty rhombuses indicate individual frequencies whose power were significantly different in the two intervals recorded in in vivo experiments ($p<0.05$, paired t-test). It is possible to appreciate that during deep anesthesia the power of oscillations tend to be somehow reduced over all the spectrum above 25-30 Hz in all four recorded areas, whereas power in the α range (10 Hz) is increased for DMN areas (mPF and CC). It should be noted that, compared to A1 and S2, mPF and CC presented a more prominent peak at around 10 Hz both in deep and light anesthesia. Shaded areas represent the standard error of the mean.

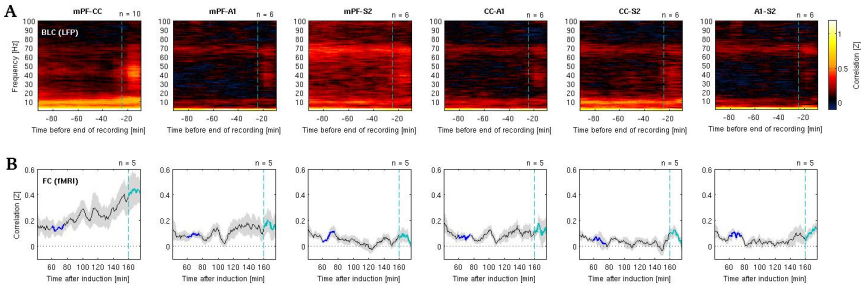

Figure B.6: BLC time courses of all area pairs simultaneously recorded in LFP experiments and BOLD FC time courses of the corresponding ROIs. (A) Average band-limited correlations (BLC) over time. Note that individual LFP recordings were slightly different in duration (see Figure 1A). Indeed, the present panels where plotted just for visualization purposes, as it was not possible to highlight an unique "deep" interval. In fact, before averaging the BLC were aligned to the end point and then equalized with respect to the shortest one. For this reason, only the interval corresponding to light anesthesia is marked, starting in correspondence of the dashed light-blue line and until the end of the recording (see Materials and Methods 2.3). (B) Correlation time courses of the corresponding pairs of ROIs obtained from separate fMRI scans. Dark- and light-blue lines superimposed over the time courses in panels B represent deep and light intervals , respectively. Interpretations of the possible relationship between BLC and FC time courses are not straightforward. In fact, imaging and in vivo experiments were not simultaneous, made use of different rats and had different durations, factors that imposed methodological limitations in performing a direct and reliable measurement of their association. Nonetheless, it is possible to qualitatively appreciate a number of features, both within and between the two different recording techniques. First, BLCs tend to exhibit a relative increase during the light interval at around 30-50 Hz (low-γ) in virtually all cases, the magnitude of this increase being the factor that apparently distinguished between mPF-CC and the other pairs of areas. Second, they also showed a rather persistent presence of correlated oscillations around 10 Hz (α) and another at around 70 Hz (mid-γ), both of which seemingly independent to the anesthetic state; It is worth to note that the size of the correlation peak in the α band is much bigger in mPF-CC (and CC-S2) compared to other area pairs. In contrast, in imaging results the only difference is between the correlation time course of mPF-CC (which increased in time) and the other ones (which maintained stable values). Taken together, these findings seem to suggest a possible relationship between brain correlated activity measured from BOLD signal and coupled neural oscillation in the γ range.

B.1 Estimation of BOLD global synchronization

To compute the Kuramoto order parameter χ, we first extracted the BOLD signal of each ROI corresponding to each 10 minutes sliding window (each one corresponding to $T = 200$ sample points) for all rats and computed the Hilbert envelope of the bandpassed (0.04-0.07 Hz, Glerean et al. 2012) signal. The time-varying overall network synchronization within each sliding window was calculated as

$$\chi(t) = \| \frac{1}{N} \sum_{i=1}^{N} e^{j\phi_i(t)} \| \tag{B.1}$$

where $t = (1, 2, ..., T)$ and $\phi_i(t)$ is the phase of the oscillation of each i-esim area at time t, being N the total number of areas.

B.2 Detection of functional communities and modularity

In mathematical terms, being c_i the community to which node i is assigned, Q is defined using the weighted adjacency matrix W_{ij}, representing the strength of the edge between nodes i and j (but set to 0 if no links exists between the two), as

$$Q = \frac{1}{2W} \sum \sum (w_{ij} - \frac{w_i w_j}{2W}) \delta(c_i, c_j) \tag{B.2}$$

where $\delta(c_i, c_j)$ is the Kronecker delta function, which takes 1 if nodes i and j are in the same community and 0 otherwise, the strengths $w_i = \sum w_{ij}$, and the total strength $W = \sum w_i = \sum \sum w_{ij}$.

B.3 LFP data analysis

The difference between the BLCs of the two states (deep and light) was computed separately for each 1 Hz-width frequency band (f) for coupled and uncoupled area pairs ij, as

$$\Delta_{LD} r_{ij}(f) = [r_{Light}(f) - r_{Deep}(f)]_{ij} \tag{B.3}$$

B.4 Quantification of the frequency shift

The relative correlation used to quantify the BLC frequency shift to higher frequencies was calculated as

$$relr_{HL}(s) = \frac{r_H}{r_L}(s) \tag{B.4}$$

where $s = (1, 2, ..., S)$ are the sliding windows, r_H is the mean correlation of the higher component (*e.g.*, 11-15 Hz), and r_L that of the lower one (*e.g.* 8-11 Hz). Each relative correlation coefficient we obtained was then converted to the corresponding Fisher's z-score.

Appendix C

Measuring graph properties

> "Classical science in its diverse disciplines, be it chemistry, biology, psychology or the social sciences, tried to isolate the elements of the observed universe - chemical compounds and enzymes, cells, elementary sensations, freely competing individuals, what not – expecting that, by putting them together again, conceptually or experimentally, the whole or system - cell, mind, society - would result and be intelligible. Now we have learned that for an understanding not only the elements but their interrelations as well are required."
>
> L. von Bertalanffy

Real world's entities are never isolated from one another, but instead are characterized by the relationships they have with other entities (Bertalanffy, 1968), giving rise to systems of varying complexity. Some of the properties of these systems can be summarized in terms of the pattern of relations between their elements, and the resulting "maps" are referred to networks. Examples can be as simple as a map of the underground, or as complex as the dynamical interactions between all the metabolites in an or-

ganism. Many of the resulting networks can be represented and analyzed as *graphs*, mathematical objects consisting of a set V of N_V *vertices* (also called *nodes*) and a set E of N_E *edges* (also called *links*) connecting the vertices (Biggs 1993; Bang-Jensen and Gutin 2008, see Figure C.1 for an example of this procedure of progressive abstraction).

The resulting graphs are typically organized in matrices, where each column (row) represents a given node, and the elements in the matrix correspond to the link between the corresponding individual nodes. Depending on the kind of system under investigation, the links between nodes can be associated with real numbers or can be either 1 if the connection is present, and 0 otherwise; in the former case, the corresponding matrix is referred to as *weighted matrix*, W, whereas in the latter case the corresponding binary matrix is called *adjacency matrix*, A (see Figure C.2). Graphs can also be *directed* if the connection between nodes i and j is different from that between j and i, whereas in *undirected* graphs the connectivity between the nodes is symmetrical.

Below we will make a non exaustive list of some of the most common measures used to quantify topological properties of graphs, together with less common ones that we used in the main body of the present dissertation.

C.1 Graph Density

The fraction of existing edges, N_E, over all possible ones, $\mathbf{N}_E$, quantifies the *density* D of a graph.

$$D = \frac{N_E}{\mathbf{N}_E} \tag{C.1}$$

The maximum number of edges in a directed graph is given by $\mathbf{N}_E^d = N_V(N_V - 1)$, whereas in undirected graphs is $\mathbf{N}_E^u = {}^1/_2 N_V(N_V - 1)$. See Figure C.3.

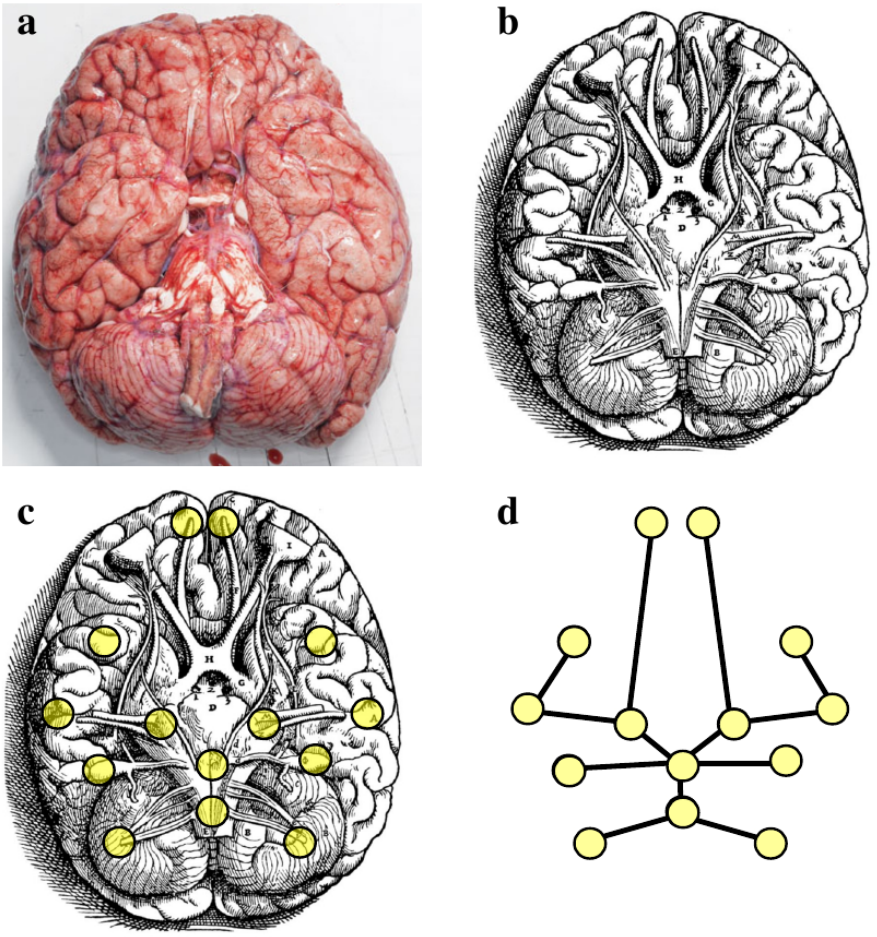

Figure C.1: Graph representation. The figure illustrates the process of progressive abstraction leading to a graph representation. (a) Real human brain viewed from below. (b) Anatomical table of the same view of the brain, as drawn from Belgian anatomist Andreas Vesalius in his *De humani corporis fabrica* (1543). (c) Some regions of the brain are highlighted. This "parcellation" of the system under examination in distinct parts (called either *nodes* or *vertices*) is the first step to create a graph. (d) Graph representation. Different regions of the brain, the nodes, are connected between them according to anatomical connections. Note that the graph depicted in panel (d) does not necessarily correspond to a realistic representation of the anatomical connectivity between the highlighted regions, but have been used only as an illustrative example of the process of progressive abstraction behind the representation of a system as a graph.

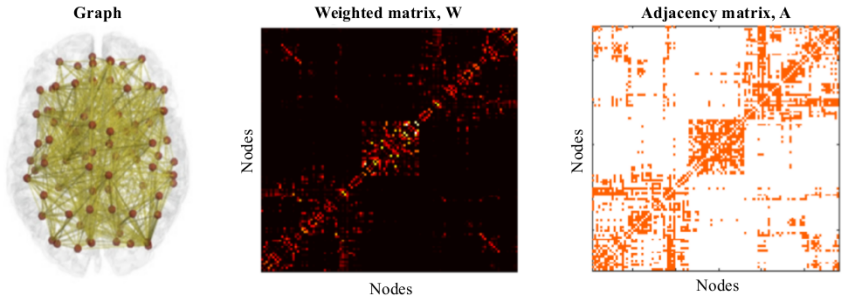

Figure C.2: Weighted and adjaency matrices. (Left) Graph representation of anatomical brain connections. Adapted from Kringelbach et al. 2015. (Middle) The same graph in a weighted matrix form. The values of each element of the matrix correspond, in this case, to the number of reconstructed streamlines between regions as obtained with diffusion tractography (see Section 1.2.4). (Right) Adjacency matrix. Orange indicates when connection between two brain regions is present (1), white that no streamline was reconstructed between the two areas (0). In this case, both networks are *undirected*, as connectivity is symmetrical.

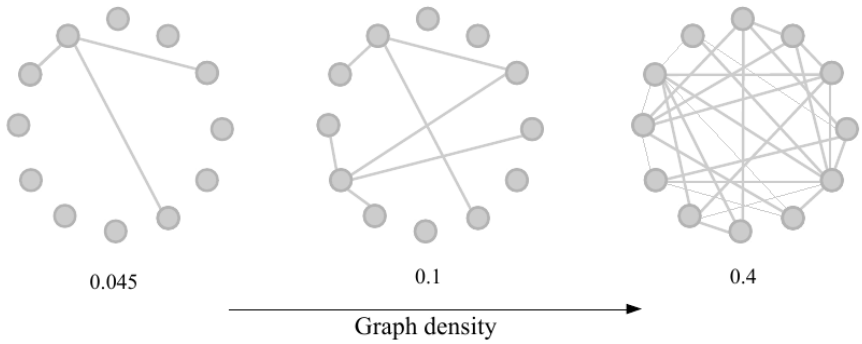

Figure C.3: Graph density. The total number of possible edges in a undirected graph with 12 vertices is 66. The three examples have 3, 7, and 28 existing edges each.

C.2 Degree and Strength

In undirected networks, the *degree* k_i of the node i corresponds to the number of other nodes it is connected with, and as such is a measure that does not take into account the weight of the connections. On the other hand, the weighted degree (the *strength*) k_i^w of a node is the sum of the weights of all its connections.

$$\begin{aligned} k_i &= \sum_{j \in N_V} a_{ij} \\ k_i^w &= \sum_{j \in N_V} w_{ij}, \end{aligned} \tag{C.2}$$

where a_{ij} is the corresponding element of the adjacency matrix A, a binary matrix storing the presence (1) or absence (0) of a connection between all pair of nodes, and w_{ij} is the weight of the corresponding connection in the weighted matrix W. In directed graphs, it is possible to compute these measures for both incoming and outcoming connections, referred to in-degree(strength) and out-degree(strength), respectively. Together with graph density, strength and degree distributions have important influence in determining (or bounding) more complex topological properties and network measures (Bang-Jensen and Gutin, 2008; Rubinov and Sporns, 2010).

C.3 Measures of Assortativity

Assortativity is a general concept referring to the coupling of elements with similar properties. In graph theory, assortativity can be measured in several ways. One of these is given by the *matching index*, MI, a measure that quantifies the similarity of the first-neighbors of two different vertices v and v'. The first-neighbors of a given node, $\Gamma(v)$ is the subset of nodes directly connected to that node, $\Gamma(v) = \{j : A_{jv} = 1\}$. As such, $MI(v, v')$ can be considered as a measure of topological similarity that take into account only the local neighborhood space of v and v', computed

as the ratio between their shared first-neighbors, $|\Gamma(v) \cap \Gamma(v')|$, with respect to the set of other distinct nodes they connect with, $|\Gamma(v) \cup \Gamma(v')|$:

$$MI(v, v') = \frac{|\Gamma(v) \cap \Gamma(v')|}{|\Gamma(v) \cup \Gamma(v')|} = \frac{\sum_{i,j=1}^{N_V} A_{vi} A_{v'j}}{k(v) + k(v') - \sum_{i,j=1}^{N_V} A_{vi} A_{v'j}}, \tag{C.3}$$

where $k(v)$ and $k(v')$ are the degree of v and v', respectively. $MI(v, v') = 0$ if the two nodes have no common neighbors, whereas $MI(v, v') = 1$ if their neighbors are identical. The classic matching index defined above is based on the adjacency matrix, and as such cannot be measured on weighted networks unless they are binarized. A similar measure that is applicable on weighted networks is *assortativity*, $S(v, v')$, that can be quantified as the correlation between the entire sets of weights defining the edges connected with two different nodes, v and v', and stored as column (or row) vectors in the weighted matrix W. $S(v, v') = cor(\mathbf{w}(v), \mathbf{w}(v'))$ is the measure used in the main body of the thesis (see Figure 4.12), and conceptually can be considered as a weighted matching index.

C.4 Clustering coefficient

The clustering coefficient is based on the observation that, in complex networks, nodes tend to cluster in densely connected groups, behavior that can be described with a metaphor describing social relationships: "*the friends of my friends are also my friends*" (Holland and Leinhardt, 1971; Watts and Strogatz, 1998). In formal terms, the clustering coefficient of a given node is given as the fraction of existing edges between its neighbors, with respect to all possible edges between them (see Figure C.4).

This measure thus quantifies how densely the i-th vertex clusters with the neighboring nodes, which is reflected by the fraction of triangles of which i is part of (*i.e.* the fraction of triangles formed

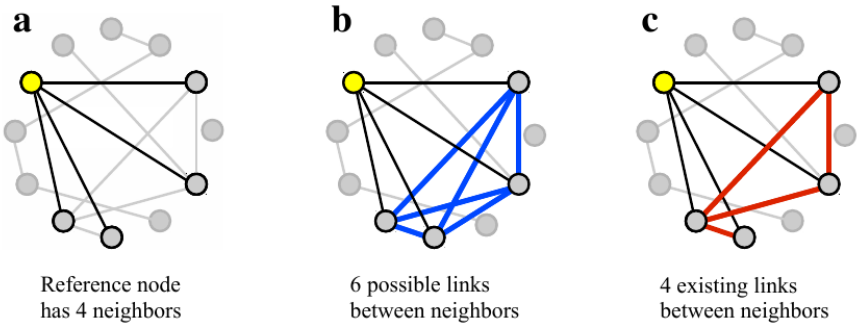

Figure C.4: Local clustering coefficient. Schematic representation of how to compute the local clustering coefficient of a given reference node, v (highlighted in yellow). (a) Original network, with connection between reference node v and its 4 neighbors highlighted in black. (b) All possible edges (6) between the neighbors of v are highlighted in blue. (c) In red, the 4 existing connections between the neighbors of v. The local clustering coefficient on node v thus corresponds to $C_v = 4/6 = 0.67$.

by the i-th node and other two connected neighbors of i). The number of triangles around a given node i is given by

$$\nabla_i = \frac{1}{2} \sum_{j,h \in N_V} a_{ij} a_{ih} a_{jh}, \tag{C.4}$$

where a_{ij}, a_{ih}, and a_{jh} are the corresponding elements of the adjacency matrix A (see Figure C.2). This measure can be extended to weighted networks, replacing a_{ij}, a_{ih}, and a_{jh} for the corresponding weights w_{ij}, w_{ih}, and w_{jh}: in that case, ∇_i will represent the "intensity" of triangles around the i-th node. Formally, the clustering coefficient of node i is defined as

$$C_i = \frac{2\nabla_i}{k_i(k_i - 1)}, \tag{C.5}$$

where k_i is the degree of the node (see Section C.2) and $k_i(k_i - 1)$ is the number of all possible edges between the neighbors of i. Another measure is the *joint clustering coefficient*, defined as

$$JC_{ij} = C_i C_j \tag{C.6}$$

The joint clustering is high if both nodes have large clustering coefficients, and low otherwise. Nonetheless, it is important to highlight that this measure does *not* account for possible overlap between the triangles around the two nodes (*i.e.* if two nodes share neighboring triangles), and as such it cannot be used as a measure of the integration between the two nodes, that can exhibit high JC but share no neighbor at all.

C.5 Path length

The path between two nodes is defined as the number of links separating them, and as such can be considered a simple measure of the influence that one node exerts over another. The number of paths of length l between nodes i and j corresponds to the l-th power of the adjacency matrix A^l_{ij} of the network (Bang-Jensen and Gutin, 2008), and as such the total number of paths of any length between any pair of nodes in the network is given by

$$\mathcal{P} = \mathbf{1} + A + A^2 + A^3 + \cdots = \sum_{l=0}^{\infty} A^l, \tag{C.7}$$

meaning that the total number of paths of any length is in fact infinite. Nonetheless, as the strength of the influence of one node over another is indeed inversely related with the length of the path (Huberman and Adamic, 2004; Ashton et al., 2005; Trusina et al., 2005), typical applications of path length usually take into account only relatively short paths, or focuses on measures such as the shortest path connecting two nodes. The *shortest path length* $L_{v,v'}$ between two vertices v and v', is the minimum number of links interposed between them (see Figure C.5), whereas the *characteristic path length* $\langle L \rangle$ of a network is the average over the shortest paths across all pair of vertices in the network (in fact it is also referred to as average path length).

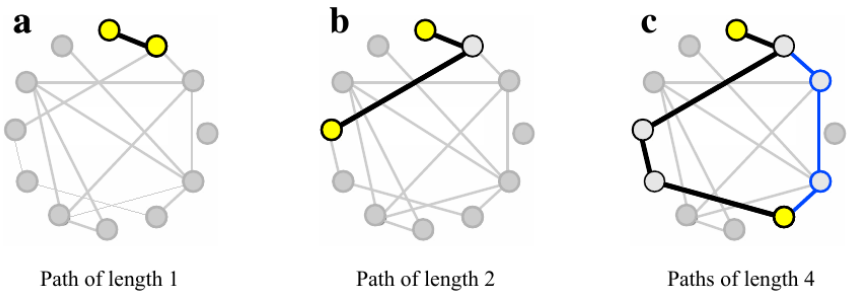

Figure C.5: Shortest path. Schematic representation of the shortest path between different pairs of nodes (highlighted in yellow). (a) Shortest path is 1. (b) Shortest path is 2. (c) Shortest path is 4. Note that there can be more than one shortest path, as highlighted in blue.

The inverse of the shortest path between two nodes has been proposed (Latora and Marchiori, 2001) as a measure of *efficiency* of information transfer, a measure that can be computed for both individual pairs of nodes (resulting in what is called *local* efficiency) or using the average shortest path length, resulting in what is referred to *global* efficiency, an unique scalar used to summarize the overall integration capacity of the network. Nonetheless, this measure does not provide any more information than path length, but has been proven to be numerically useful for disconnected graphs, as in these situations the efficiency would be zero, whereas $\langle L \rangle = \infty$ (Achard and Bullmore, 2007).

C.6 Small-Worldness

In an influential paper, Watts and Strogatz (1998) noted that many real-world systems are neither completely regular nor completely random, but rather exhibit some intermediate topological architecture. In particular, they noted that these systems tend to show high local connectivity, meaning that the probability of nodes to be connected decayed with distance, but and the same time they have few long-range connections. This kind of architecture, considered to be optimal in terms of whole-network infor-

mation transfer (Latora and Marchiori, 2001), has been referred to as "small-world" (see Figure C.6).

The two authors of this observation thus proposed a measure to quantify how "small-world" a given network is. This measure is just a simple ratio between the average clustering coefficient and the average path length of a network (both normalized for random network having the same degree distribution of the original one).

$$SW = \frac{C/C_{rand}}{L/L_{rand}} \tag{C.8}$$

The more SW exceeds 1, the more the network is considered to be small-world. It is believed that, in principle, brain networks should at least exhibit some degree of small-worldness, as this kind of architecture should mirror the co-existence of segregated modules that nonetheless interact with each other (Sporns and Zwi, 2004; Sporns and Honey, 2006; Bassett and Bullmore, 2006). Nonetheless, it has been noted that how much "small-world" a brain is crucially depends on the level of observation (Hilgetag and Goulas, 2015), as recent experimental evidences suggest that, at the cellular level, the cortex is densely connected in a manner that is incompatible with a small-world topology (Markov et al., 2013).

C.7 Communicability

The classic measure of path length (Appendix C.5) ignores the number of possible alternative paths existing between any pair of nodes. In fact, information flow does not follow a unique path, but rather spreads along several ones, each of different length and strength. This kind of information is exploited by a metric called *communicability*, a generalization of path length that accounts for the influence along all paths of any length between two nodes (Estrada and Hatano, 2008). As such, the communicability accounts for the possibility of a "peripheral" spreading of communications through multiple paths of different lengths.

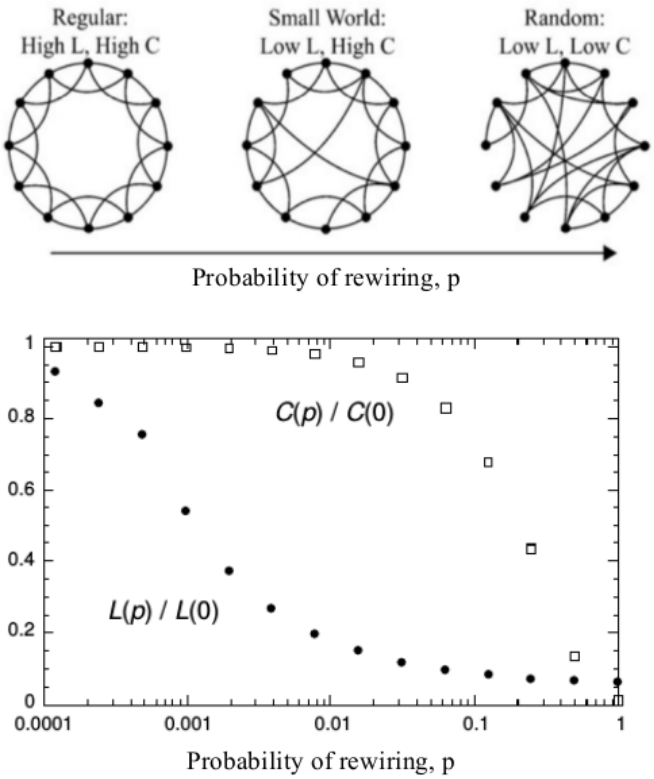

Figure C.6: Small-world topology. Top: Examples of three different networks obtained rewiring each link with a given probability p, but maintain the same number of links as in the regular lattice (Top-Left). Bottom: Average clustering coefficient, C, and average path length, L (each normalized using an appropriate random network) for different values of rewiring probability. According to Watts and Strogatz 1998, small-world architectures correspond to large average clustering and low average path length. Adapted from Watts and Strogatz 1998

Shorter paths are linked to more effective communications between nodes (Huberman and Adamic, 2004; Ashton et al., 2005; Trusina et al., 2005; Zamora-López et al., 2016), which motivated the use of a "penalty" for longer paths in the form of a decay of their influence. With this in mind, Estrada and Hatano (2008) introduced a measure of communicability based on the assumption that shorter paths contributes more than longer ones through the form of an exponential decay, and showed that in this case the communicability matrix $\mathcal{C}$ corresponds, by definition, to the exponential of the matrix A.

$$\mathcal{C} = \sum_{l=0}^{\infty} \frac{A^l}{l!} = \mathbf{1} + A + \frac{A^2}{2!} + \frac{A^3}{3!} + \cdots = e^A \tag{C.9}$$

The communicability matric $\mathcal{C}$ can be obtained both from adjacency (A) or from weighted matrix W, making this measure an excellent and versatile candidate to quantify the *influence*, accumulated over all possible paths of any length, exerted by a given node over any other node in the network, where longer paths will contribute less than shorter ones. From a physical perspective, this measure is analogous to a diffusion process characterized by a nonlinear decay for longer paths (Zamora-López et al., 2016). Its use in this context is justified by the above cited theoretical findings and the results from network models presented in Section 4.2; furthermore, due to the intrinsic stochasticity of synaptic activity and the complex interactions between excitatory and inhibitory neurons, it is legitimate to assume that the net influence that a given neuron (or a population) have on the activity of another neuron (population) is inversely related with the minimal number of synaptic connections separating the two, which can be considered their "synaptic" distance.

C.8 Expected covariation

Using the information about the influence that a given node exerts on any other node through any path (through the use of the measure of communicability described above in Appendix C.7),

it is possible to derive an analytical measure that quantifies the strength of the *covariation* that one can expect in the activity between any pair of nodes in a network. The i-th column $\mathbf{c}_i$ of the communicability matrix $\mathcal{C}$ represents the overall relative topological influence that the i-th node receives -through all paths of any length- from the rest of the network in which it is embedded. With this in mind, it is legitimate to assume that, if two nodes have similar topological profiles (*i.e.* they receive similar influences from all other nodes in the network), their activities will strongly co-vary. We can thus define the *expected covariation* $\mathcal{T}_{ij}$ between two nodes i and j as the similarity between the corresponding vectors $\mathbf{c}_i$ and $\mathbf{c}_j$. Here we will use the cosine similarity between the vectors, even if any measures of similarity between vectors can be used. In this case, we defined $\mathcal{T}_{ij}$ as

$$\mathcal{T}_{ij} = \frac{\mathbf{c_i} \cdot \mathbf{c_j}}{\|\mathbf{c_i}\|\|\mathbf{c_j}\|} \tag{C.10}$$

This original measure of expected covariation is based on the similarity of the complete topological profiles between any pair of nodes (in fact it shares the same logic behind assortativity measures, see Appendix C.3), and is in principle applicable to any type of network from which the communicability matrix $\mathcal{C}$ can be obtained. It ranges from -1 to 1, and its interpretation is analogous to that of a classic Pearson's correlation coefficient r. In fact, due to the well-known relationship between the cosine between two vectors and r, if the vectors in $\mathcal{C}$ are centered by subtracting their vector mean, then the expected covariation matrix $\mathcal{T}$ is equivalent to a correlation matrix. in addition, the fact that $\mathcal{T}$ is obtained analytically, makes it very easy and versatile to use, avoiding possibly long and computationally expansive numerical simulations. Finally, the effects that other specific topological properties of the network (such as its degree distribution, the existence of modules, the type of graph and so on) exert on the arising correlation structure should in principle be all implicitly captured and resumed in $\mathcal{T}$.

The above mentioned properties makes $\mathcal{T}$ a powerful candidate when it comes to evaluate the major contribution of network

topology on the emerging pattern of covariations displayed by individual elements of the system, and independently quantified (on a distinct dataset putatively sharing the same connectivity matrix) using measures of pairwise relationship such as the Pearson correlation coefficient. The hypothesized relationship between the topological expected covariation and the average correlation structure of network activity, namely that $\mathcal{T} \approx \langle R \rangle$, can in principle be tested in different ways. For example, assuming that the matrix A (or W) is a good representation of the real structural network, then the more instances ("samples") R_i are used to compute $\langle R \rangle$, the better $\mathcal{T}$ should approximate $\langle R \rangle$, provided that each R_i share the same A (W).

The topological covariation $\mathcal{T}$ quantifies the extent of the similarity of the communicability profiles between pairs of nodes, and provides a good approximation of the overall average correlation structure that a given network can sustain. As such, we are making the explicit assumption that covariation (in a given direction) of the topological profiles somehow corresponds to covariation (in the same direction) of the dynamical profiles. Nonetheless, it is important to stress that (i) this assumption, even if legitimate, does not correspond to an absolute necessity, and (ii) the same caveats of both the covariance and the correlation hold when interpreting results from this measure of expected covariation: these measures only quantify the extent to which two random variables change together, but give no clue on the causal relationship between them.

In real world, different systems are usually characterized by distinct local dynamics, determined by different parameters (which may be unknown); this can dramatically change the strength of the dependence on the underlying topology, *e.g.* making even longer paths potentially relevant (as in the case of information spreading in social networks). In neuroscience, a seminal example of the fundamental effects that endogenous modulation of local dynamics have on changing the dependence of the system on the underlying connectivity is the observation that, compared to the awake state, the spreading of neural activity across the cortex (measured with EEG) following a perturbation (*via* TMS)

is significantly reduced during sleep, resulting in a rapid spatial fading of the evoked activity around the perturbed locus (Massimini et al., 2005). As such, it can be preferable to find the working regime of $\mathcal{T}$ that best fits the empirical data, *e.g.* by multiplying the communicability matrix $\mathcal{C}$ by a global coupling factor g prior to computing $\mathcal{T}$ ($i.e\ C = e^{gA}$), and optimize it in order to control for the particular strength of the dependence on the network structure. This optimization procedure allows to obtain meaningful insights, as about the extent to which the system of interest can be understood mainly in terms of the topology of the relationship between its parts; or it may inform, through comparing the best-fitting g obtained from different states, about specific dynamical changes in the relationship between structure and function, or about the overall quality and reliability of the network used to obtain $\mathcal{T}$ (or about some of its individual links or elements); or it can be used to make precise predictions of the whole-network changes in pairwise relationships following any type of structural or dynamical perturbations.

Bibliography

Achard, S. and Bullmore, E. (2007). Efficiency and cost of economical brain functional networks. *PLoS Comput Biol*, 3(2):e17. 167

Ahrens, M. B., Orger, M. B., Robson, D. N., Li, J. M., and Keller, P. J. (2013). Whole-brain functional imaging at cellular resolution using light-sheet microscopy. *Nature Methods*, 10(5):413–420. 146, 147

Alkire, M. T., Hudetz, A. G., and Tononi, G. (2008). Consciousness and Anesthesia. *Science*, 322(5903):876–880. 68, 73

Alkire, M. T. M., Haier, R. J. P., Shah, N. K. M., and Anderson, C. T. M. (1997). Positron Emission Tomography Study of Regional Cerebral Metabolism in Humans during Isoflurane Anesthesia. *The Journal of the American Society of Anesthesiologists*, 86(3):549–557. 1

Allen, E. A., Damaraju, E., Plis, S. M., Erhardt, E. B., Eichele, T., and Calhoun, V. D. (2012). Tracking Whole-Brain Connectivity Dynamics in the Resting State. *Cerebral Cortex*, page bhs352. 23

Alstott, J., Breakspear, M., Hagmann, P., Cammoun, L., and Sporns, O. (2009). Modeling the Impact of Lesions in the Human Brain. *PLOS Comput Biol*, 5(6):e1000408. 80

Ames III, A. (2000). CNS energy metabolism as related to function. *Brain Research Reviews*, 34(12):42–68. 12

Arenas, A., Daz-Guilera, A., Kurths, J., Moreno, Y., and Zhou, C. (2008). Synchronization in complex networks. *Physics Reports*, 469(3):93–153. 110, 133

Arieli, A., Sterkin, A., Grinvald, A., and Aertsen, A. (1996). Dynamics of Ongoing Activity: Explanation of the Large Variability in Evoked Cortical Responses. *Science*, 273(5283):1868–1871. 3, 4

Arnett, D. W. (1978). Statistical dependence between neighboring retinal ganglion cells in goldfish. *Experimental Brain Research*, 32(1):49–53. 140

Ashton, D. J., Jarrett, T. C., and Johnson, N. F. (2005). Effect of Congestion Costs on Shortest Paths Through Complex Networks. *Physical Review Letters*, 94(5):058701. 166, 170

Attwell, D. and Laughlin, S. B. (2001). An Energy Budget for Signaling in the Grey Matter of the Brain. *Journal of Cerebral Blood Flow & Metabolism*, 21(10):1133–1145. 12

Avena-Koenigsberger, A., Mišić, B., Hawkins, R. X., Griffa, A., Hagmann, P., Goñi, J., and Sporns, O. (2016). Path ensembles and a tradeoff between communication efficiency and resilience in the human connectome. *Brain Structure and Function*, pages 1–16. 133

Bak, P., Tang, C., and Wiesenfeld, K. (1987). Self-organized criticality: An explanation of the 1/ \textit{f} noise. *Physical Review Letters*, 59(4):381–384. 24

Bang-Jensen, J. and Gutin, G. Z. (2008). *Digraphs: Theory, Algorithms and Applications*. Springer. 99, 103, 106, 160, 163, 166

Barabsi, A.-L. and Albert, R. (1999). Emergence of Scaling in Random Networks. *Science*, 286(5439):509–512. 133

Barnes, S. J. and Finnerty, G. T. (2010). Sensory Experience and Cortical Rewiring. *The Neuroscientist*, 16(2):186–198. 37

Bassett, D. S. and Bullmore, E. (2006). Small-World Brain Networks. *The Neuroscientist*, 12(6):512–523. 68, 168

Becerra, L., Pendse, G., Chang, P.-C., Bishop, J., and Borsook, D. (2011). Robust Reproducible Resting State Networks in the Awake Rodent Brain. *PLOS ONE*, 6(10):e25701. 43

Beckmann, C. F., DeLuca, M., Devlin, J. T., and Smith, S. M. (2005). Investigations into resting-state connectivity using independent component analysis. *Philosophical Transactions of the Royal Society B: Biological Sciences*, 360(1457):1001–1013. 4, 7, 8, 16, 17, 18, 43

Bertalanffy, L. v. (1968). *General System Theory: Foundations, Development, Applications*. G. Braziller. 9, 159

Bettinardi, R. G., Tort-Colet, N., Ruiz-Mejias, M., Sanchez-Vives, M. V., and Deco, G. (2015). Gradual emergence of spontaneous correlated brain activity during fading of general anesthesia in rats: Evidences from fMRI and local field potentials. *NeuroImage*, 114:185–198. 6, 42, 149

Bienenstock, E. L., Cooper, L. N., and Munro, P. W. (1982). Theory for the development of neuron selectivity: orientation specificity and binocular interaction in visual cortex. *The Journal of Neuroscience*, 2(1):32–48. 78

Biggs, N. (1993). *Algebraic Graph Theory*. Cambridge University Press. 106, 160

Bihan, D. L. and Iima, M. (2015). Diffusion Magnetic Resonance Imaging: What Water Tells Us about Biological Tissues. *PLOS Biol*, 13(7):e1002203. 29

Birbaumer, N., Elbert, T., Canavan, A. G., and Rockstroh, B. (1990). Slow potentials of the cerebral cortex and behavior. *Physiological Reviews*, 70(1):1–41. 26

Birn, R. M., Diamond, J. B., Smith, M. A., and Bandettini, P. A. (2006). Separating respiratory-variation-related fluctuations from neuronal-activity-related fluctuations in fMRI. *NeuroImage*, 31(4):1536–1548. 17

Birn, R. M., Molloy, E. K., Patriat, R., Parker, T., Meier, T. B., Kirk, G. R., Nair, V. A., Meyerand, M. E., and Prabhakaran, V. (2013). The effect of scan length on the reliability of resting-state fMRI connectivity estimates. *NeuroImage*, 83:550–558. 20, 22, 23

Biswal, B., Zerrin Yetkin, F., Haughton, V. M., and Hyde, J. S. (1995). Functional connectivity in the motor cortex of resting human brain using echo-planar mri. *Magnetic Resonance in*

Medicine, 34(4):537–541. 2, 3, 7, 9, 16, 43

Biswal, B. B., Mennes, M., Zuo, X.-N., Gohel, S., Kelly, C., Smith, S. M., Beckmann, C. F., Adelstein, J. S., Buckner, R. L., Colcombe, S., Dogonowski, A.-M., Ernst, M., Fair, D., Hampson, M., Hoptman, M. J., Hyde, J. S., Kiviniemi, V. J., Kötter, R., Li, S.-J., Lin, C.-P., Lowe, M. J., Mackay, C., Madden, D. J., Madsen, K. H., Margulies, D. S., Mayberg, H. S., McMahon, K., Monk, C. S., Mostofsky, S. H., Nagel, B. J., Pekar, J. J., Peltier, S. J., Petersen, S. E., Riedl, V., Rombouts, S. A. R. B., Rypma, B., Schlaggar, B. L., Schmidt, S., Seidler, R. D., Siegle, G. J., Sorg, C., Teng, G.-J., Veijola, J., Villringer, A., Walter, M., Wang, L., Weng, X.-C., Whitfield-Gabrieli, S., Williamson, P., Windischberger, C., Zang, Y.-F., Zhang, H.-Y., Castellanos, F. X., and Milham, M. P. (2010). Toward discovery science of human brain function. *Proceedings of the National Academy of Sciences*, 107(10):4734–4739. 7, 16, 18, 22

Blondel, V. D., Guillaume, J.-L., Lambiotte, R., and Lefebvre, E. (2008). Fast unfolding of communities in large networks. *Journal of Statistical Mechanics: Theory and Experiment*, 2008(10):P10008. 52

Boccaletti, S., Latora, V., Moreno, Y., Chavez, M., and Hwang, D. U. (2006). Complex networks: Structure and dynamics. *Physics Reports*, 424(45):175–308. 134

Boveroux, P., Vanhaudenhuyse, A., Bruno, M.-A., Noirhomme, Q., Lauwick, S., Luxen, A., Degueldre, C., Plenevaux, A., Schnakers, C., Phillips, C., Brichant, J.-F., Bonhomme, V., Maquet, P., Greicius, M. D., Laureys, S., and Boly, M. (2010). Breakdown of within- and between-network Resting State Functional Magnetic Resonance Imaging Connectivity during Propofol-induced Loss of Consciousness:. *Anesthesiology*, 113(5):1038–1053. 43, 71

Braun, A. R., Balkin, T. J., Wesenten, N. J., Carson, R. E., Varga, M., Baldwin, P., Selbie, S., Belenky, G., and Herscovitch, P. (1997). Regional cerebral blood flow throughout the sleep-wake cycle. An H2(15)O PET study. *Brain*, 120(7):1173–1197. 1

Breakspear, M. and Jirsa, V. K. (2007). Neuronal Dynamics and Brain Connectivity. In Jirsa, V. K. and McIntosh, A. R., editors, *Handbook of Brain Connectivity*, Understanding Complex Systems, pages 3–64. Springer Berlin Heidelberg. DOI: 10.1007/978-3-540-71512-2_1. 79

Breakspear, M., Terry, J. R., and Friston, K. J. (2003). Modulation of excitatory synaptic coupling facilitates synchronization and complex dynamics in a biophysical model of neuronal dynamics. *Network: Computation in Neural Systems*, 14(4):703–732. 80, 82

Brewer, J. A., Worhunsky, P. D., Gray, J. R., Tang, Y.-Y., Weber, J., and Kober, H. (2011). Meditation experience is associated with differences in default mode network activity and connectivity. *Proceedings of the National Academy of Sciences*, 108(50):20254–20259. 43

Brookes, M. J., Woolrich, M., Luckhoo, H., Price, D., Hale, J. R., Stephenson, M. C., Barnes, G. R., Smith, S. M., and Morris, P. G. (2011). Investigating the electrophysiological basis of resting state networks using magnetoencephalography. *Proceedings of the National Academy of Sciences*, 108(40):16783–16788. 53, 72

Brown, E. N., Lydic, R., and Schiff, N. D. (2010). General Anesthesia, Sleep, and Coma. *New England Journal of Medicine*, 363(27):2638–2650. 43, 74

Brown, E. N., Purdon, P. L., and Van Dort, C. J. (2011). General Anesthesia and Altered States of Arousal: A Systems Neuroscience Analysis. *Annual Review of Neuroscience*, 34:601–628. 74, 75

Bruhn, J., Rpcke, H., and Hoeft, A. (2000). Approximate Entropy as an Electroencephalographic Measure of Anesthetic Drug Effect during Desflurane Anesthesia:. *Anesthesiology*, 92(3):715–726. 73

Brunel, N. and Wang, X.-J. (2001). Effects of Neuromodulation in a Cortical Network Model of Object Working Memory Dominated by Recurrent Inhibition. *Journal of Computational Neuroscience*, 11(1):63–85. 85

Buckner, R. L., Andrews-Hanna, J. R., and Schacter, D. L. (2008). The Brain's Default Network. *Annals of the New York Academy of Sciences*, 1124(1):1–38. 70

Buckner, R. L. and Carroll, D. C. (2007). Self-projection and the brain. *Trends in Cognitive Sciences*, 11(2):49–57. 70

Buckner, R. L. and Vincent, J. L. (2007). Unrest at rest: Default activity and spontaneous network correlations. *NeuroImage*, 37(4):1091–1096. 1

Bullmore, E. and Sporns, O. (2009). Complex brain networks: graph theoretical analysis of structural and functional systems. *Nature Reviews Neuroscience*, 10(3):186–198. 37, 38, 105, 116

Bullmore, E. and Sporns, O. (2012). The economy of brain network organization. *Nature Reviews Neuroscience*, 13(5):336–349. 39

Buzsaki, G. (2006). *Rhythms of the Brain*. Oxford University Press. 44

Buzsáki, G. (2010). Neural Syntax: Cell Assemblies, Synapsembles, and Readers. *Neuron*, 68(3):362–385. 37

Buzsáki, G. and Draguhn, A. (2004). Neuronal Oscillations in Cortical Networks. *Science*, 304(5679):1926–1929. 24, 25, 44

Buzsáki, G., Logothetis, N., and Singer, W. (2013). Scaling Brain Size, Keeping Timing: Evolutionary Preservation of Brain Rhythms. *Neuron*, 80(3):751–764. 24, 25

Cabeza, R. and Nyberg, L. (2000). Imaging Cognition II: An Empirical Review of 275 PET and fMRI Studies. *Journal of Cognitive Neuroscience*, 12(1):1–47. 2, 13

Cabral, J., Hugues, E., Sporns, O., and Deco, G. (2011). Role of local network oscillations in resting-state functional connectivity. *NeuroImage*, 57(1):130–139. 56, 79, 89

Cabral, J., Kringelbach, M. L., and Deco, G. (2014a). Exploring the network dynamics underlying brain activity during rest. *Progress in Neurobiology*, 114:102–131. 43, 53, 79, 94

Cabral, J., Luckhoo, H., Woolrich, M., Joensson, M., Mohseni, H., Baker, A., Kringelbach, M. L., and Deco, G. (2014b). Exploring mechanisms of spontaneous functional connectivity in MEG: How delayed network interactions lead to structured am-

plitude envelopes of band-pass filtered oscillations. *NeuroImage*, 90:423–435. 72

Carhart-Harris, R. L., Erritzoe, D., Williams, T., Stone, J. M., Reed, L. J., Colasanti, A., Tyacke, R. J., Leech, R., Malizia, A. L., Murphy, K., Hobden, P., Evans, J., Feilding, A., Wise, R. G., and Nutt, D. J. (2012). Neural correlates of the psychedelic state as determined by fMRI studies with psilocybin. *Proceedings of the National Academy of Sciences of the United States of America*, 109(6):2138–2143. 6, 43, 71

Cauda, F., Micon, B. M., Sacco, K., Duca, S., D'Agata, F., Geminiani, G., and Canavero, S. (2009). Disrupted intrinsic functional connectivity in the vegetative state. *Journal of Neurology, Neurosurgery, and Psychiatry*, 80(4):429–431. 8

Cheetham, C. E. J., Hammond, M. S. L., McFarlane, R., and Finnerty, G. T. (2008). Altered Sensory Experience Induces Targeted Rewiring of Local Excitatory Connections in Mature Neocortex. *The Journal of Neuroscience*, 28(37):9249–9260. 37

Choe, A. S., Jones, C. K., Joel, S. E., Muschelli, J., Belegu, V., Caffo, B. S., Lindquist, M. A., Zijl, C. M., and Pekar, J. J. (2015). Reproducibility and Temporal Structure in Weekly Resting-State fMRI over a Period of 3.5 Years:e0140134. *PLoS One*, 10(10). 7, 20, 21, 22

Christoff, K., Gordon, A. M., Smallwood, J., Smith, R., and Schooler, J. W. (2009). Experience sampling during fMRI reveals default network and executive system contributions to mind wandering. *Proceedings of the National Academy of Sciences*, 106(21):8719–8724. 16

Chung, K. and Deisseroth, K. (2013). CLARITY for mapping the nervous system. *Nature Methods*, 10(6):508–513. 29

Chung, K., Wallace, J., Kim, S.-Y., Kalyanasundaram, S., Andalman, A. S., Davidson, T. J., Mirzabekov, J. J., Zalocusky, K. A., Mattis, J., Denisin, A. K., Pak, S., Bernstein, H., Ramakrishnan, C., Grosenick, L., Gradinaru, V., and Deisseroth, K. (2013). Structural and molecular interrogation of intact biological systems. *Nature*, 497(7449):332–337. 29

Churchland, P. S. and Sejnowski, T. J. (1988). Perspectives on

cognitive neuroscience. *Science*, 242(4879):741–745. 10

Churchland, P. S. and Sejnowski, T. J. (1994). *The Computational Brain*. MIT Press. 9, 37

Coenen, A., Fine, E., and Zayachkivska, O. (2014). Adolf Beck: A Forgotten Pioneer in Electroencephalography. *Journal of the History of the Neurosciences*, 23(3):276–286. 1

Cohen, E., Ivenshitz, M., Amor-Baroukh, V., Greenberger, V., and Segal, M. (2008). Determinants of spontaneous activity in networks of cultured hippocampus. *Brain Research*, 1235:21–30. 140

Compte, A., Sanchez-Vives, M. V., McCormick, D. A., and Wang, X.-J. (2003). Cellular and Network Mechanisms of Slow Oscillatory Activity (<1 Hz) and Wave Propagations in a Cortical Network Model. *Journal of Neurophysiology*, 89(5):2707–2725. 141

Conturo, T. E., Lori, N. F., Cull, T. S., Akbudak, E., Snyder, A. Z., Shimony, J. S., McKinstry, R. C., Burton, H., and Raichle, M. E. (1999). Tracking neuronal fiber pathways in the living human brain. *Proceedings of the National Academy of Sciences*, 96(18):10422–10427. 29

Csicsvari, J., Jamieson, B., Wise, K. D., and Buzsáki, G. (2003). Mechanisms of Gamma Oscillations in the Hippocampus of the Behaving Rat. *Neuron*, 37(2):311–322. 24, 26

Cumin, D. and Unsworth, C. P. (2007). Generalising the Kuramoto model for the study of neuronal synchronisation in the brain. *Physica D: Nonlinear Phenomena*, 226(2):181–196. 56

Damoiseaux, J. S., Rombouts, S. a. R. B., Barkhof, F., Scheltens, P., Stam, C. J., Smith, S. M., and Beckmann, C. F. (2006). Consistent resting-state networks across healthy subjects. *Proceedings of the National Academy of Sciences*, 103(37):13848–13853. 6

Damoiseaux, J. S., Seeley, W. W., Zhou, J., Shirer, W. R., Coppola, G., Karydas, A., Rosen, H. J., Miller, B. L., Kramer, J. H., and Greicius, M. D. (2012). Gender Modulates the APOE 4 Effect in Healthy Older Adults: Convergent Evidence from Functional Brain Connectivity and Spinal Fluid Tau Levels.

The Journal of Neuroscience, 32(24):8254–8262. 8

Deco, G., Jirsa, V., McIntosh, A. R., Sporns, O., and Kotter, R. (2009a). Key role of coupling, delay, and noise in resting brain fluctuations. *Proceedings of the National Academy of Sciences*, 106(25):10302–10307. 68

Deco, G., Jirsa, V., McIntosh, A. R., Sporns, O., and Kötter, R. (2009b). Key role of coupling, delay, and noise in resting brain fluctuations. *Proceedings of the National Academy of Sciences*, 106(25):10302–10307. 79, 84, 85

Deco, G. and Jirsa, V. K. (2012). Ongoing Cortical Activity at Rest: Criticality, Multistability, and Ghost Attractors. *The Journal of Neuroscience*, 32(10):3366–3375. 79, 85

Deco, G., Jirsa, V. K., and McIntosh, A. R. (2011). Emerging concepts for the dynamical organization of resting-state activity in the brain. *Nature Reviews Neuroscience*, 12(1):43–56. 43

Deco, G., Jirsa, V. K., and McIntosh, A. R. (2013). Resting brains never rest: computational insights into potential cognitive architectures. *Trends in Neurosciences*, 36(5):268–274. 88, 94

Deco, G., Jirsa, V. K., Robinson, P. A., Breakspear, M., and Friston, K. (2008). The Dynamic Brain: From Spiking Neurons to Neural Masses and Cortical Fields. *PLOS Comput Biol*, 4(8):e1000092. 85

Deco, G. and Kringelbach, M. (2014). Great Expectations: Using Whole-Brain Computational Connectomics for Understanding Neuropsychiatric Disorders. *Neuron*, 84(5):892–905. 38

Deco, G. and Kringelbach, M. L. (2016). Metastability and Coherence: Extending the Communication through Coherence Hypothesis Using A Whole-Brain Computational Perspective. *Trends in Neurosciences*, 39(3):125–135. 90, 96, 133

Deco, G. and Rolls, E. T. (2006). Decision-making and Weber's law: a neurophysiological model. *European Journal of Neuroscience*, 24(3):901–916. 85

Engel, A. K., Fries, P., and Singer, W. (2001). Dynamic predictions: Oscillations and synchrony in topdown processing. *Nature Reviews Neuroscience*, 2(10):704–716. 24

Engel, A. K. and Singer, W. (2001). Temporal binding and the neural correlates of sensory awareness. *Trends in Cognitive Sciences*, 5(1):16–25. 24

Estrada, E. and Hatano, N. (2008). Communicability in complex networks. *Physical Review E*, 77(3):036111. 113, 134, 168, 170

Estrada, E., Hatano, N., and Benzi, M. (2012). The physics of communicability in complex networks. *Physics Reports*, 514(3):89–119. 113

Faisal, A. A., Selen, L. P. J., and Wolpert, D. M. (2008). Noise in the nervous system. *Nature Reviews Neuroscience*, 9(4):292–303. 2

Faivre, A., Rico, A., Zaaraoui, W., Crespy, L., Reuter, F., Wybrecht, D., Soulier, E., Malikova, I., Confort-Gouny, S., Cozzone, P. J., Pelletier, J., Ranjeva, J.-P., and Audoin, B. (2012). Assessing brain connectivity at rest is clinically relevant in early multiple sclerosis. *Multiple Sclerosis Journal*, 18(9):1251–1258. 8

Ferenets, R., Vanluchene, A., Lipping, T., Heyse, B., and Struys, M. M. R. F. (2007). Behavior of Entropy/Complexity Measures of the Electroencephalogram during Propofol-induced Sedation: Dose-dependent Effects of Remifentanil. *Anesthesiology*, 106(4):696–706. 73

Fillard, P., Descoteaux, M., Goh, A., Gouttard, S., Jeurissen, B., Malcolm, J., Ramirez-Manzanares, A., Reisert, M., Sakaie, K., Tensaouti, F., Yo, T., Mangin, J.-F., and Poupon, C. (2011). Quantitative evaluation of 10 tractography algorithms on a realistic diffusion MR phantom. *NeuroImage*, 56(1):220–234. 29

Finn, E. S., Shen, X., Scheinost, D., Rosenberg, M. D., Huang, J., Chun, M. M., Papademetris, X., and Constable, R. T. (2015). Functional connectome fingerprinting: identifying individuals using patterns of brain connectivity. *Nature Neuroscience*, 18(11):1664–1671. 20

Fishbein, I. and Segal, M. (2007). Miniature synaptic currents become neurotoxic to chronically silenced neurons. *Cerebral Cortex*, 17(6):1292–1306. 147

Fisher, R. A. (1915). Frequency Distribution of the Values of the

Correlation Coefficient in Samples from an Indefinitely Large Population. *Biometrika*, 10(4):507–521. 49

FitzHugh, R. (1961). Impulses and Physiological States in Theoretical Models of Nerve Membrane. *Biophysical Journal*, 1(6):445–466. 83

Fornito, A., Zalesky, A., and Breakspear, M. (2013). Graph analysis of the human connectome: Promise, progress, and pitfalls. *NeuroImage*, 80:426–444. 39

Fox, M. D. and Raichle, M. E. (2007). Spontaneous fluctuations in brain activity observed with functional magnetic resonance imaging. *Nature Reviews Neuroscience*, 8(9):700–711. 15

Fox, M. D., Snyder, A. Z., Vincent, J. L., Corbetta, M., Essen, D. C. V., and Raichle, M. E. (2005). The human brain is intrinsically organized into dynamic, anticorrelated functional networks. *Proceedings of the National Academy of Sciences of the United States of America*, 102(27):9673–9678. 5, 7, 16, 43, 85

Franks, N. P. (2008). General anaesthesia: from molecular targets to neuronal pathways of sleep and arousal. *Nature Reviews Neuroscience*, 9(5):370–386. 43, 71

Fransson, P. (2005). Spontaneous low-frequency BOLD signal fluctuations: An fMRI investigation of the resting-state default mode of brain function hypothesis. *Human Brain Mapping*, 26(1):15–29. 6

Fransson, P. (2006). How default is the default mode of brain function?: Further evidence from intrinsic BOLD signal fluctuations. *Neuropsychologia*, 44(14):2836–2845. 4

Fransson, P., Skild, B., Engstrm, M., Hallberg, B., Mosskin, M., den, U., Lagercrantz, H., and Blennow, M. (2009). Spontaneous Brain Activity in the Newborn Brain During Natural SleepAn fMRI Study in Infants Born at Full Term. *Pediatric Research*, 66(3):301–305. 43

Fransson, P., Skild, B., Horsch, S., Nordell, A., Blennow, M., Lagercrantz, H., and den, U. (2007). Resting-state networks in the infant brain. *Proceedings of the National Academy of Sciences*, 104(39):15531–15536. 43

Freyer, F., Roberts, J. A., Becker, R., Robinson, P. A., Ritter, P., and Breakspear, M. (2011). Biophysical Mechanisms of Multistability in Resting-State Cortical Rhythms. *The Journal of Neuroscience*, 31(17):6353–6361. 90

Freyer, F., Roberts, J. A., Ritter, P., and Breakspear, M. (2012). A Canonical Model of Multistability and Scale-Invariance in Biological Systems. *PLOS Comput Biol*, 8(8):e1002634. 90

Fries, P. (2005). A mechanism for cognitive dynamics: neuronal communication through neuronal coherence. *Trends in Cognitive Sciences*, 9(10):474–480. 24, 73

Fries, P. (2009). Neuronal Gamma-Band Synchronization as a Fundamental Process in Cortical Computation. *Annual Review of Neuroscience*, 32(1):209–224. 73

Friston, K. J., Frith, C. D., Liddle, P. F., and Frackowiak, R. S. J. (1993). Functional Connectivity: The Principal-Component Analysis of Large (PET) Data Sets. *Journal of Cerebral Blood Flow & Metabolism*, 13(1):5–14. 18, 49, 53, 55

Friston, K. J., Harrison, L., and Penny, W. (2003). Dynamic causal modelling. *NeuroImage*, 19(4):1273–1302. 84, 89

Gambuzza, L. V., Cardillo, A., Fiasconaro, A., Fortuna, L., Gómez-Gardeñes, J., and Frasca, M. (2013). Analysis of remote synchronization in complex networks. *Chaos: An Interdisciplinary Journal of Nonlinear Science*, 23(4):043103. 102

Gerstein, G. L. and Perkel, D. H. (1969). Simultaneously Recorded Trains of Action Potentials: Analysis and Functional Interpretation. *Science*, 164(3881):828–830. 18

Ghosh, A., Rho, Y., McIntosh, A. R., Kötter, R., and Jirsa, V. K. (2008). Noise during Rest Enables the Exploration of the Brain's Dynamic Repertoire. *PLOS Comput Biol*, 4(10):e1000196. 79, 83

Glerean, E., Salmi, J., Lahnakoski, J. M., Jskelinen, I. P., and Sams, M. (2012). Functional Magnetic Resonance Imaging Phase Synchronization as a Measure of Dynamic Functional Connectivity. *Brain Connectivity*, 2(2):91–101. 18, 19, 96, 156

Gómez, S., Jensen, P., and Arenas, A. (2009). Analysis of community structure in networks of correlated data. *Physical Review*

E, 80(1):016114. 52

Gómez-Gardeñes, J., Moreno, Y., and Arenas, A. (2007). Paths to Synchronization on Complex Networks. *Physical Review Letters*, 98(3):034101. 133

Goñi, J., Heuvel, M. P. v. d., Avena-Koenigsberger, A., Mendizabal, N. V. d., Betzel, R. F., Griffa, A., Hagmann, P., Corominas-Murtra, B., Thiran, J.-P., and Sporns, O. (2014). Resting-brain functional connectivity predicted by analytic measures of network communication. *Proceedings of the National Academy of Sciences*, 111(2):833–838. 133

Greicius, M. D., Flores, B. H., Menon, V., Glover, G. H., Solvason, H. B., Kenna, H., Reiss, A. L., and Schatzberg, A. F. (2007). Resting-State Functional Connectivity in Major Depression: Abnormally Increased Contributions from Subgenual Cingulate Cortex and Thalamus. *Biological Psychiatry*, 62(5):429–437. 8, 148

Greicius, M. D., Kiviniemi, V., Tervonen, O., Vainionp, V., Alahuhta, S., Reiss, A. L., and Menon, V. (2008). Persistent default-mode network connectivity during light sedation. *Human Brain Mapping*, 29(7):839–847. 9, 43, 70

Greicius, M. D., Krasnow, B., Reiss, A. L., and Menon, V. (2003). Functional connectivity in the resting brain: A network analysis of the default mode hypothesis. *Proceedings of the National Academy of Sciences*, 100(1):253–258. 5, 43

Gusnard, D. A. and Raichle, M. E. (2001). Searching for a baseline: Functional imaging and the resting human brain. *Nature Reviews Neuroscience*, 2(10):685–694. 4, 5, 6

Haas, L. F. (2003). Hans Berger (18731941), Richard Caton (18421926), and electroencephalography. *Journal of Neurology, Neurosurgery & Psychiatry*, 74(1):9–9. 1

Hagmann, P., Cammoun, L., Gigandet, X., Gerhard, S., Ellen Grant, P., Wedeen, V., Meuli, R., Thiran, J.-P., Honey, C. J., and Sporns, O. (2010). MR connectomics: Principles and challenges. *Journal of Neuroscience Methods*, 194(1):34–45. 37

Hagmann, P., Cammoun, L., Gigandet, X., Meuli, R., Honey, C. J., Wedeen, V. J., and Sporns, O. (2008). Mapping

the Structural Core of Human Cerebral Cortex. *PLOS Biol*, 6(7):e159. 71

Haken, H. (1975). Cooperative phenomena in systems far from thermal equilibrium and in nonphysical systems. *Reviews of Modern Physics*, 47(1):67. 79

Hasenkamp, W. and Barsalou, L. W. (2012). Effects of meditation experience on functional connectivity of distributed brain networks. *Frontiers in Human Neuroscience*, 6:38. 43

He, B. J. and Raichle, M. E. (2009). The fMRI signal, slow cortical potential and consciousness. *Trends in Cognitive Sciences*, 13(7):302–309. 26

Hebb, D. O. (1949). *The Organization of Behavior: A Neuropsychological Theory*. Psychology Press. 37

Hilgetag, C. C. and Goulas, A. (2015). Is the brain really a small-world network? *Brain Structure and Function*, 221(4):2361–2366. 168

Hindriks, R., van Putten, M. J. A. M., and Deco, G. (2014). Intracortical propagation of EEG alpha oscillations. *NeuroImage*, 103:444–453. 79

Hipp, J. F., Hawellek, D. J., Corbetta, M., Siegel, M., and Engel, A. K. (2012). Large-scale cortical correlation structure of spontaneous oscillatory activity. *Nature Neuroscience*, 15(6):884–890. 27, 53, 72

Hodgkin, A. L. and Huxley, A. F. (1952). A quantitative description of membrane current and its application to conduction and excitation in nerve. *The Journal of Physiology*, 117(4):500–544. 78, 83

Hofman, M. A. (1989). On the evolution and geometry of the brain in mammals. *Progress in neurobiology*, 32(2):137–158. 44

Holland, P. W. and Leinhardt, S. (1971). Transitivity in structural models of small groups. *Comparative Group Studies*, 2(2):107–124. 164

Honey, C. J., Kötter, R., Breakspear, M., and Sporns, O. (2007). Network structure of cerebral cortex shapes functional connectivity on multiple time scales. *Proceedings of the National Academy of Sciences*, 104(24):10240–10245. 80

Honey, C. J., Sporns, O., Cammoun, L., Gigandet, X., Thiran, J. P., Meuli, R., and Hagmann, P. (2009). Predicting human resting-state functional connectivity from structural connectivity. *Proceedings of the National Academy of Sciences*, 106(6):2035–2040. 39, 79, 80

Horovitz, S. G., Braun, A. R., Carr, W. S., Picchioni, D., Balkin, T. J., Fukunaga, M., and Duyn, J. H. (2009). Decoupling of the brain's default mode network during deep sleep. *Proceedings of the National Academy of Sciences*, 106(27):11376–11381. 9, 16, 43, 70

Horovitz, S. G., Fukunaga, M., de Zwart, J. A., van Gelderen, P., Fulton, S. C., Balkin, T. J., and Duyn, J. H. (2008). Low frequency BOLD fluctuations during resting wakefulness and light sleep: A simultaneous EEG-fMRI study. *Human Brain Mapping*, 29(6):671–682. 43

Horwitz, B., Warner, B., Fitzer, J., Tagamets, M.-A., Husain, F. T., and Long, T. W. (2005). Investigating the neural basis for functional and effective connectivity. Application to fMRI. *Philosophical Transactions of the Royal Society of London B: Biological Sciences*, 360(1457):1093–1108. 18

Hubel, D. H. and Wiesel, T. N. (1959). Receptive fields of single neurones in the cat's striate cortex. *The Journal of Physiology*, 148(3):574–591. 140

Huberman, B. A. and Adamic, L. A. (2004). Information Dynamics in the Networked World. In Ben-Naim, E., Frauenfelder, H., and Toroczkai, Z., editors, *Complex Networks*, number 650 in Lecture Notes in Physics, pages 371–398. Springer Berlin Heidelberg. DOI: 10.1007/978-3-540-44485-5_17. 166, 170

Hudetz, A. G., Liu, X., and Pillay, S. (2014). Dynamic Repertoire of Intrinsic Brain States Is Reduced in Propofol-Induced Unconsciousness. *Brain Connectivity*, 5(1):10–22. 68

Hurlburt, R. T., Alderson-Day, B., Fernyhough, C., and Khn, S. (2015). What goes on in the resting-state? A qualitative glimpse into resting-state experience in the scanner. *Frontiers in Psychology*, 6. 16

Hutchison, R. M., Mirsattari, S. M., Jones, C. K., Gati, J. S., and

Leung, L. S. (2010). Functional Networks in the Anesthetized Rat Brain Revealed by Independent Component Analysis of Resting-State fMRI. *Journal of Neurophysiology*, 103(6):3398–3406. 43, 48

Hutchison, R. M., Womelsdorf, T., Allen, E. A., Bandettini, P. A., Calhoun, V. D., Corbetta, M., Della Penna, S., Duyn, J. H., Glover, G. H., Gonzalez-Castillo, J., Handwerker, D. A., Keilholz, S., Kiviniemi, V., Leopold, D. A., de Pasquale, F., Sporns, O., Walter, M., and Chang, C. (2013). Dynamic functional connectivity: Promise, issues, and interpretations. *NeuroImage*, 80:360–378. 23, 49

Izhikevich, E. M. and Edelman, G. M. (2008). Large-scale model of mammalian thalamocortical systems. *Proceedings of the National Academy of Sciences*, 105(9):3593–3598. 79

Izquierdo, E. J. and Beer, R. D. (2013). Connecting a Connectome to Behavior: An Ensemble of Neuroanatomical Models of C. elegans Klinotaxis. *PLOS Comput Biol*, 9(2):e1002890. 37

Jbabdi, S., Sotiropoulos, S. N., Haber, S. N., Van Essen, D. C., and Behrens, T. E. (2015). Measuring macroscopic brain connections in vivo. *Nature Neuroscience*, 18(11):1546–1555. 29

Jones, D. K. (2010). Challenges and limitations of quantifying brain connectivity in vivo with diffusion MRI. *Imaging in Medicine*, 2(3):341–355. 29, 32, 119

Jones, D. K., Knsche, T. R., and Turner, R. (2013). White matter integrity, fiber count, and other fallacies: The do's and don'ts of diffusion MRI. *NeuroImage*, 73:239–254. 29

Kaisti, K. K., Metshonkala, L., Ters, M., Oikonen, V., Aalto, S., Jskelinen, S., Hinkka, S., and Scheinin, H. (2002). Effects of Surgical Levels of Propofol and Sevoflurane Anesthesia on Cerebral Blood Flow in Healthy Subjects Studied with Positron Emission Tomography. *The Journal of the American Society of Anesthesiologists*, 96(6):1358–1370. 43

Kasthuri, N., Hayworth, K., Berger, D., Schalek, R., Conchello, J., Knowles-Barley, S., Lee, D., Vzquez-Reina, A., Kaynig, V., Jones, T., Roberts, M., Morgan, J., Tapia, J., Seung, H. S., Roncal, W., Vogelstein, J., Burns, R., Sussman, D., Priebe, C.,

Pfister, H., and Lichtman, J. (2015). Saturated Reconstruction of a Volume of Neocortex. *Cell*, 162(3):648–661. 29, 30

Katz, L. C. and Shatz, C. J. (1996). Synaptic Activity and the Construction of Cortical Circuits. *Science*, 274(5290):1133–1138. 146

Kayser, C., Kim, M., Ugurbil, K., Kim, D.-S., and Knig, P. (2004). A Comparison of Hemodynamic and Neural Responses in Cat Visual Cortex Using Complex Stimuli. *Cerebral Cortex*, 14(8):881–891. 26, 74

Kazama, H. and Wilson, R. I. (2009). Origins of correlated activity in an olfactory circuit. *Nature Neuroscience*, 12(9):1136–1144. 142

Keilholz, S. D., Magnuson, M. E., Pan, W.-J., Willis, M., and Thompson, G. J. (2012). Dynamic Properties of Functional Connectivity in the Rodent. *Brain Connectivity*, 3(1):31–40. 49, 68

Kennedy, D. P. and Courchesne, E. (2008). The intrinsic functional organization of the brain is altered in autism. *NeuroImage*, 39(4):1877–1885. 8, 148

Klimesch, W. (1999). EEG alpha and theta oscillations reflect cognitive and memory performance: a review and analysis. *Brain Research Reviews*, 29(23):169–195. 24

Kopell, N., Ermentrout, G. B., Whittington, M. A., and Traub, R. D. (2000). Gamma rhythms and beta rhythms have different synchronization properties. *Proceedings of the National Academy of Sciences*, 97(4):1867–1872. 24

Kötter, R. (2004). Online retrieval, processing, and visualization of primate connectivity data from the CoCoMac Database. *Neuroinformatics*, 2(2):127–144. 29, 80

Kringelbach, M. L., McIntosh, A. R., Ritter, P., Jirsa, V. K., and Deco, G. (2015). The Rediscovery of Slowness: Exploring the Timing of Cognition. *Trends in Cognitive Sciences*, 19(10):616–628. 162

Kuramoto, Y. (1975). Self-entrainment of a population of coupled non-linear oscillators. In Araki, P. H., editor, *International Symposium on Mathematical Problems in Theoretical Physics*,

number 39 in Lecture Notes in Physics, pages 420–422. Springer Berlin Heidelberg. DOI: 10.1007/BFb0013365. 49

Kuramoto, Y. (1984). *Chemical Oscillations, Waves, and Turbulence*, volume 19 of *Springer Series in Synergetics*. Springer Berlin Heidelberg, Berlin, Heidelberg. 89

Larson-Prior, L. J., Power, J. D., Vincent, J. L., Nolan, T. S., Coalson, R. S., Zempel, J., Snyder, A. Z., Schlaggar, B. L., Raichle, M. E., and Petersen, S. E. (2011). Modulation of the brain's functional network architecture in the transition from wake to sleep. *Progress in brain research*, 193. 43

Latora, V. and Marchiori, M. (2001). Efficient Behavior of Small-World Networks. *Physical Review Letters*, 87(19):198701. 68, 105, 167, 168

Laufs, H., Krakow, K., Sterzer, P., Eger, E., Beyerle, A., Salek-Haddadi, A., and Kleinschmidt, A. (2003). Electroencephalographic signatures of attentional and cognitive default modes in spontaneous brain activity fluctuations at rest. *Proceedings of the National Academy of Sciences*, 100(19):11053–11058. 26

Laughlin, S. B. (2001). Energy as a constraint on the coding and processing of sensory information. *Current Opinion in Neurobiology*, 11(4):475–480. 12, 13

Laureys, S., Owen, A. M., and Schiff, N. D. (2004). Brain function in coma, vegetative state, and related disorders. *The Lancet Neurology*, 3(9):537–546. 71

Lennie, P. (2003). The Cost of Cortical Computation. *Current Biology*, 13(6):493–497. 12

Leopold, D. A. and Maier, A. (2012). Ongoing physiological processes in the cerebral cortex. *NeuroImage*, 62(4):2190–2200. 18, 26

Leung, L. S., Luo, T., Ma, J., and Herrick, I. (2014). Brain areas that influence general anesthesia. *Progress in Neurobiology*, 122:24–44. 70

Lewis, L. D., Weiner, V. S., Mukamel, E. A., Donoghue, J. A., Eskandar, E. N., Madsen, J. R., Anderson, W. S., Hochberg, L. R., Cash, S. S., Brown, E. N., and Purdon, P. L. (2012). Rapid fragmentation of neuronal networks at the onset of

propofol-induced unconsciousness. *Proceedings of the National Academy of Sciences*, 109(49):E3377–E3386. 66

Liang, Z., King, J., and Zhang, N. (2011). Uncovering Intrinsic Connectional Architecture of Functional Networks in Awake Rat Brain. *The Journal of Neuroscience*, 31(10):3776–3783. 9, 16, 43, 68

Liu, X., Zhu, X.-H., Zhang, Y., and Chen, W. (2011). Neural Origin of Spontaneous Hemodynamic Fluctuations in Rats under BurstSuppression Anesthesia Condition. *Cerebral Cortex*, 21(2):374–384. 43

Liu, Z., Fukunaga, M., de Zwart, J. A., and Duyn, J. H. (2010). Large-scale spontaneous fluctuations and correlations in brain electrical activity observed with magnetoencephalography. *NeuroImage*, 51(1):102–111. 26

Logothetis, N. K. (2008). What we can do and what we cannot do with fMRI. *Nature*, 453(7197):869–878. 11, 14, 15

Logothetis, N. K., Pauls, J., Augath, M., Trinath, T., and Oeltermann, A. (2001). Neurophysiological investigation of the basis of the fMRI signal. *Nature*, 412(6843):150–157. 15, 26, 73

Lu, H., Zou, Q., Gu, H., Raichle, M. E., Stein, E. A., and Yang, Y. (2012). Rat brains also have a default mode network. *Proceedings of the National Academy of Sciences*, 109(10):3979–3984. 6, 7, 9, 16, 43, 62, 68, 70, 71

Lu, H., Zuo, Y., Gu, H., Waltz, J. A., Zhan, W., Scholl, C. A., Rea, W., Yang, Y., and Stein, E. A. (2007). Synchronized delta oscillations correlate with the resting-state functional MRI signal. *Proceedings of the National Academy of Sciences*, 104(46):18265–18269. 43

Macey, P. M., Macey, K. E., Kumar, R., and Harper, R. M. (2004). A method for removal of global effects from fMRI time series. *NeuroImage*, 22(1):360–366. 18

Magri, C., Schridde, U., Murayama, Y., Panzeri, S., and Logothetis, N. K. (2012). The Amplitude and Timing of the BOLD Signal Reflects the Relationship between Local Field Potential Power at Different Frequencies. *The Journal of Neuroscience*, 32(4):1395–1407. 15, 26, 74

Maistrenko, Y. L., Lysyansky, B., Hauptmann, C., Burylko, O., and Tass, P. A. (2007). Multistability in the Kuramoto model with synaptic plasticity. *Physical Review E*, 75(6):066207. 56

Majeed, W., Magnuson, M., and Keilholz, S. D. (2009). Spatiotemporal dynamics of low frequency fluctuations in BOLD fMRI of the rat. *Journal of Magnetic Resonance Imaging*, 30(2):384–393. 23

Majewska, A. K. and Sur, M. (2006). Plasticity and specificity of cortical processing networks. *Trends in Neurosciences*, 29(6):323–329. 37

Makarenko, V. and Llinás, R. (1998). Experimentally determined chaotic phase synchronization in a neuronal system. *Proceedings of the National Academy of Sciences*, 95(26):15747–15752. 140

Mantini, D., Gerits, A., Nelissen, K., Durand, J.-B., Joly, O., Simone, L., Sawamura, H., Wardak, C., Orban, G. A., Buckner, R. L., and Vanduffel, W. (2011). Default Mode of Brain Function in Monkeys. *The Journal of Neuroscience*, 31(36):12954–12962. 43

Markov, N. T., Ercsey-Ravasz, M., Essen, D. C. V., Knoblauch, K., Toroczkai, Z., and Kennedy, H. (2013). Cortical High-Density Counterstream Architectures. *Science*, 342(6158):1238406. 168

Marr, D. (2010). *Vision: A Computational Investigation Into the Human Representation and Processing of Visual Information*. London. 9

Martuzzi, R., Ramani, R., Qiu, M., Rajeevan, N., and Constable, R. T. (2010). Functional connectivity and alterations in baseline brain state in humans. *NeuroImage*, 49(1):823–834. 66

Mason, M. F., Norton, M. I., Horn, J. D. V., Wegner, D. M., Grafton, S. T., and Macrae, C. N. (2007). Wandering Minds: The Default Network and Stimulus-Independent Thought. *Science*, 315(5810):393–395. 6

Massimini, M., Ferrarelli, F., Huber, R., Esser, S. K., Singh, H., and Tononi, G. (2005). Breakdown of Cortical Effective Con-

nectivity During Sleep. *Science*, 309(5744):2228–2232. 73, 173

Mazoyer, B., Zago, L., Mellet, E., Bricogne, S., Etard, O., Houd, O., Crivello, F., Joliot, M., Petit, L., and Tzourio-Mazoyer, N. (2001). Cortical networks for working memory and executive functions sustain the conscious resting state in man. *Brain Research Bulletin*, 54(3):287–298. 4

Mcculloch, W. and Pitts, W. (1943). A logical calculus of the ideas immanent in nervous activity. *Bulletin of Mathematical Biophysics*, 5. 78

Meunier, D., Lambiotte, R., and Bullmore, E. T. (2010). Modular and hierarchically modular organization of brain networks. *Frontiers in Neuroscience*, 4:200. 68

Milo, R., Shen-Orr, S., Itzkovitz, S., Kashtan, N., Chklovskii, D., and Alon, U. (2002). Network Motifs: Simple Building Blocks of Complex Networks. *Science*, 298(5594):824–827. 110

Mohajerani, M. H., Chan, A. W., Mohsenvand, M., LeDue, J., Liu, R., McVea, D. A., Boyd, J. D., Wang, Y. T., Reimers, M., and Murphy, T. H. (2013). Spontaneous cortical activity alternates between motifs defined by regional axonal projections. *Nature Neuroscience*, 16(10):1426–1435. 143

Momose-Sato, Y., Sato, K., and Kinoshita, M. (2007). Spontaneous depolarization waves of multiple origins in the embryonic rat CNS. *European Journal of Neuroscience*, 25(4):929–944. 146

Monod, J. (1974). On Chance and Necessity. In Ayala, F. J. and Dobzhansky, T., editors, *Studies in the Philosophy of Biology*, pages 357–375. Macmillan Education UK. DOI: 10.1007/978-1-349-01892-5_20. 135

Morris, C. and Lecar, H. (1981). Voltage oscillations in the barnacle giant muscle fiber. *Biophysical Journal*, 35(1):193–213. 80

Murphy, K., Birn, R. M., and Bandettini, P. A. (2013). Resting-state fMRI confounds and cleanup. *NeuroImage*, 80:349–359. 17

Murphy, K., Birn, R. M., Handwerker, D. A., Jones, T. B., and Bandettini, P. A. (2009). The impact of global signal regres-

sion on resting state correlations: Are anti-correlated networks introduced? *NeuroImage*, 44(3):893–905. 18

Nagumo, J., Arimoto, S., and Yoshizawa, S. (1962). An Active Pulse Transmission Line Simulating Nerve Axon. *Proceedings of the IRE*, 50(10):2061–2070. 83

Nakagawa, T. T., Woolrich, M., Luckhoo, H., Joensson, M., Mohseni, H., Kringelbach, M. L., Jirsa, V., and Deco, G. (2014). How delays matter in an oscillatory whole-brain spiking-neuron network model for MEG alpha-rhythms at rest. *NeuroImage*, 87:383–394. 79

Newman, M., Barabsi, A.-L., and Watts, D. J. (2011). *The Structure and Dynamics of Networks*. Princeton University Press. 94, 134

Newton, J. R. and Sur, M. (2005). Rewiring Cortex: Functional Plasticity of the Auditory Cortex during Development. In Syka, J. and Merzenich, M. M., editors, *Plasticity and Signal Representation in the Auditory System*, pages 127–137. Springer US. DOI: 10.1007/0-387-23181-1_11. 37

Nicosia, V., Valencia, M., Chavez, M., Daz-Guilera, A., and Latora, V. (2013). Remote Synchronization Reveals Network Symmetries and Functional Modules. *Physical Review Letters*, 110(17):174102. 102

Niessing, J., Ebisch, B., Schmidt, K. E., Niessing, M., Singer, W., and Galuske, R. A. W. (2005). Hemodynamic Signals Correlate Tightly with Synchronized Gamma Oscillations. *Science*, 309(5736):948–951. 26, 74

O'Donovan, M. J. (1999). The origin of spontaneous activity in developing networks of the vertebrate nervous system. *Current Opinion in Neurobiology*, 9(1):94–104. 145

Ogawa, S., Lee, T. M., Kay, A. R., and Tank, D. W. (1990a). Brain magnetic resonance imaging with contrast dependent on blood oxygenation. *Proceedings of the National Academy of Sciences*, 87(24):9868–9872. 2

Ogawa, S., Lee, T.-M., Nayak, A. S., and Glynn, P. (1990b). Oxygenation-sensitive contrast in magnetic resonance image of rodent brain at high magnetic fields. *Magnetic Resonance in*

Medicine, 14(1):68–78. 14

Ogawa, S. and Sung, Y.-W. (2007). Functional magnetic resonance imaging. *Scholarpedia*, 2(10):3105. 44

Ogawa, S., Tank, D. W., Menon, R., Ellermann, J. M., Kim, S. G., Merkle, H., and Ugurbil, K. (1992). Intrinsic signal changes accompanying sensory stimulation: functional brain mapping with magnetic resonance imaging. *Proceedings of the National Academy of Sciences*, 89(13):5951–5955. 44

Palay, L. (1956). *Synapses in the central nervous system*. 37

Pan, W.-J., Thompson, G., Magnuson, M., Majeed, W., Jaeger, D., and Keilholz, S. (2011). Broadband Local Field Potentials Correlate with Spontaneous Fluctuations in Functional Magnetic Resonance Imaging Signals in the Rat Somatosensory Cortex Under Isoflurane Anesthesia. *Brain Connectivity*, 1(2):119–131. 26, 74

Park, H.-J. and Friston, K. (2013). Structural and Functional Brain Networks: From Connections to Cognition. *Science*, 342(6158):1238411. 44

Pasquale, F. d., Penna, S. D., Snyder, A. Z., Lewis, C., Mantini, D., Marzetti, L., Belardinelli, P., Ciancetta, L., Pizzella, V., Romani, G. L., and Corbetta, M. (2010). Temporal dynamics of spontaneous MEG activity in brain networks. *Proceedings of the National Academy of Sciences*, 107(13):6040–6045. 72

Pawela, C. P., Biswal, B. B., Cho, Y. R., Kao, D. S., Li, R., Jones, S. R., Schulte, M. L., Matloub, H. S., Hudetz, A. G., and Hyde, J. S. (2008). Resting-state functional connectivity of the rat brain. *Magnetic Resonance in Medicine*, 59(5):1021–1029. 43, 68

Paxinos, G. and Watson, C. (2006). *The Rat Brain in Stereotaxic Coordinates: Hard Cover Edition*. Academic Press. 48

Poldrack, R. A. (2006). Can cognitive processes be inferred from neuroimaging data? *Trends in Cognitive Sciences*, 10(2):59–63. 9

Porter, K. R., Claude, A., and Fullam, E. F. (1945). A study of tissue culture cells by electron microscopy: Methods and preliminary observations. *The Journal of experimental medicine*,

81(3):233–246. 36

Power, J., Cohen, A., Nelson, S., Wig, G., Barnes, K., Church, J., Vogel, A., Laumann, T., Miezin, F., Schlaggar, B., and Petersen, S. (2011). Functional Network Organization of the Human Brain. *Neuron*, 72(4):665–678. 23

Quibell, R., Prommer, E. E., Mihalyo, M., Twycross, R., and Wilcock, A. (2011). Ketamine*. *Journal of Pain and Symptom Management*, 41(3):640–649. 75, 132

Raichle, M. E. (1983). Positron emission tomography. *Annual Review of Neuroscience*, 6:249–267. 44

Raichle, M. E. (2006). The Brain's Dark Energy. *Science*, 314(5803):1249–1250. 12

Raichle, M. E., MacLeod, A. M., Snyder, A. Z., Powers, W. J., Gusnard, D. A., and Shulman, G. L. (2001). A default mode of brain function. *Proceedings of the National Academy of Sciences of the United States of America*, 98(2):676–682. 5, 35, 70

Raichle, M. E. and Mintun, M. A. (2006). Brain Work and Brain Imaging. *Annual Review of Neuroscience*, 29(1):449–476. 12

Raichle, M. E. and Snyder, A. Z. (2007). A default mode of brain function: A brief history of an evolving idea. *NeuroImage*, 37(4):1083–1090. 6

Ramón y Cajal, S. (1909). *Histologie du systme nerveux de l'homme & des vertbrs*. Paris : Maloine. 28

Richiardi, J., Altmann, A., Milazzo, A.-C., Chang, C., Chakravarty, M. M., Banaschewski, T., Barker, G. J., Bokde, A. L., Bromberg, U., Büchel, C., et al. (2015). Correlated gene expression supports synchronous activity in brain networks. *Science*, 348(6240):1241–1244. 143, 144

Richiardi, J., Eryilmaz, H., Schwartz, S., Vuilleumier, P., and Van De Ville, D. (2011). Decoding brain states from fMRI connectivity graphs. *NeuroImage*, 56(2):616–626. 16

Rilling, J. K., Barks, S. K., Parr, L. A., Preuss, T. M., Faber, T. L., Pagnoni, G., Bremner, J. D., and Votaw, J. R. (2007). A comparison of resting-state brain activity in humans and chimpanzees. *Proceedings of the National Academy of Sciences*,

104(43):17146–17151. 70

Rombouts, S. A. R. B., Stam, C. J., Kuijer, J. P. A., Scheltens, P., and Barkhof, F. (2003). Identifying confounds to increase specificity during a no task condition: Evidence for hippocampal connectivity using fMRI. *NeuroImage*, 20(2):1236–1245. 17

Rubinov, M. and Sporns, O. (2010). Complex network measures of brain connectivity: Uses and interpretations. *NeuroImage*, 52(3):1059–1069. 52, 116, 163

Ruiz-Mejias, M., Ciria-Suarez, L., Mattia, M., and Sanchez-Vives, M. V. (2011). Slow and fast rhythms generated in the cerebral cortex of the anesthetized mouse. *Journal of Neurophysiology*, 106(6):2910–2921. 48, 141

Sämann, P. G., Wehrle, R., Hoehn, D., Spoormaker, V. I., Peters, H., Tully, C., Holsboer, F., and Czisch, M. (2011). Development of the Brain's Default Mode Network from Wakefulness to Slow Wave Sleep. *Cerebral Cortex*, page bhq295. 70, 71

Sanchez-Vives, M. V. and McCormick, D. A. (2000). Cellular and network mechanisms of rhythmic recurrent activity in neocortex. *Nature Neuroscience*, 3(10):1027–1034. 141

Sancristbal, B., Rebollo, B., Boada, P., Sanchez-Vives, M. V., and Garcia-Ojalvo, J. (2016). Collective stochastic coherence in recurrent neuronal networks. *Nature Physics*, advance online publication. 2

Schmahmann, J. D., Pandya, D. N., Wang, R., Dai, G., D'Arceuil, H. E., Crespigny, A. J. d., and Wedeen, V. J. (2007). Association fibre pathways of the brain: parallel observations from diffusion spectrum imaging and autoradiography. *Brain*, 130(3):630–653. 31, 34

Schlvinck, M. L., Maier, A., Ye, F. Q., Duyn, J. H., and Leopold, D. A. (2010). Neural basis of global resting-state fMRI activity. *Proceedings of the National Academy of Sciences*, 107(22):10238–10243. 26, 74

Sejnowski, T. J., Churchland, P. S., and Movshon, J. A. (2014). Putting big data to good use in neuroscience. *Nature neuroscience*, 17(11):1440–1441. 11

Sherrington, C. S. (1906). Observations on the scratch-reflex in

the spinal dog. *The Journal of Physiology*, 34(1-2):1–50. 36

Shmuel, A. and Leopold, D. A. (2008). Neuronal correlates of spontaneous fluctuations in fMRI signals in monkey visual cortex: Implications for functional connectivity at rest. *Human Brain Mapping*, 29(7):751–761. 17, 26

Shulman, R. G., Rothman, D. L., Behar, K. L., and Hyder, F. (2004). Energetic basis of brain activity: implications for neuroimaging. *Trends in Neurosciences*, 27(8):489–495. 4, 12

Sinclair, M. D. (2003). A review of the physiological effects of 2-agonists related to the clinical use of medetomidine in small animal practice. *The Canadian Veterinary Journal*, 44(11):885–897. 75

Singer, W. (1999). Neuronal Synchrony: A Versatile Code for the Definition of Relations? *Neuron*, 24(1):49–65. 24, 73

Sirota, A., Csicsvari, J., Buhl, D., and Buzsáki, G. (2003). Communication between neocortex and hippocampus during sleep in rodents. *Proceedings of the National Academy of Sciences*, 100(4):2065–2069. 24

Smith, S. M., Fox, P. T., Miller, K. L., Glahn, D. C., Fox, P. M., Mackay, C. E., Filippini, N., Watkins, K. E., Toro, R., Laird, A. R., and Beckmann, C. F. (2009). Correspondence of the brain's functional architecture during activation and rest. *Proceedings of the National Academy of Sciences*, 106(31):13040–13045. 7, 8

Snyder, A. Z. and Raichle, M. E. (2012). A brief history of the resting state: The Washington University perspective. *NeuroImage*, 62(2):902–910. 7

Sokoloff, L., Mangold, R., Wechsler, R. L., Kennedy, C., and Kety, S. S. (1955). THE EFFECT OF MENTAL ARITHMETIC ON CEREBRAL CIRCULATION AND METABOLISM 1. *Journal of Clinical Investigation*, 34(7 Pt 1):1101–1108. 1

Song, H. F., Kennedy, H., and Wang, X.-J. (2014). Spatial embedding of structural similarity in the cerebral cortex. *Proceedings of the National Academy of Sciences*, 111(46):16580–16585. 37

Sporns, O. (2013). Network attributes for segregation and integration in the human brain. *Current Opinion in Neurobiology*,

23(2):162–171. 68

Sporns, O. (2014). Contributions and challenges for network models in cognitive neuroscience. *Nature Neuroscience*, 17(5):652–660. 37, 38, 39

Sporns, O. and Honey, C. J. (2006). Small worlds inside big brains. *Proceedings of the National Academy of Sciences*, 103(51):19219–19220. 168

Sporns, O. and Kötter, R. (2004). Motifs in Brain Networks. *PLOS Biol*, 2(11):e369. 110

Sporns, O., Tononi, G., and Edelman, G. (2002). Theoretical neuroanatomy and the connectivity of the cerebral cortex. *Behavioural Brain Research*, 135(1-2):69–74. 105

Sporns, O. and Zwi, J. (2004). The small world of the cerebral cortex. *NeuroInformatics*, 2(2):145–162. 68, 105, 168

Stafford, J. M., Jarrett, B. R., Miranda-Dominguez, O., Mills, B. D., Cain, N., Mihalas, S., Lahvis, G. P., Lattal, K. M., Mitchell, S. H., David, S. V., Fryer, J. D., Nigg, J. T., and Fair, D. A. (2014). Large-scale topology and the default mode network in the mouse connectome. *Proceedings of the National Academy of Sciences*, 111(52):18745–18750. 70

Stamatakis, E. A., Adapa, R. M., Absalom, A. R., and Menon, D. K. (2010). Changes in Resting Neural Connectivity during Propofol Sedation. *PLOS ONE*, 5(12):e14224. 43

Stein, R. B., Gossen, E. R., and Jones, K. E. (2005). Neuronal variability: noise or part of the signal? *Nature Reviews Neuroscience*, 6(5):389–397. 2

Stender, J., Mortensen, K., Thibaut, A., Darkner, S., Laureys, S., Gjedde, A., and Kupers, R. (2016). The Minimal Energetic Requirement of Sustained Awareness after Brain Injury. *Current Biology*, 26(11):1494–1499. 13, 14

Stephan, K. E., Kamper, L., Bozkurt, A., Burns, G. A. P. C., Young, M. P., and Kötter, R. (2001). Advanced database methodology for the Collation of Connectivity data on the Macaque brain (CoCoMac). *Philosophical Transactions of the Royal Society B: Biological Sciences*, 356(1412):1159–1186. 29

Steriade, M. (2001). Impact of Network Activities on Neuronal

Properties in Corticothalamic Systems. *Journal of Neurophysiology*, 86(1):1–39. 24, 26

Steriade, M., Amzica, F., and Contreras, D. (1996). Synchronization of fast (30-40 Hz) spontaneous cortical rhythms during brain activation. *The Journal of Neuroscience*, 16(1):392–417. 44, 140

Steriade, M., McCormick, D. A., and Sejnowski, T. J. (1993). Thalamocortical oscillations in the sleeping and aroused brain. *Science*, 262(5134):679–685. 71

Striedter, G. F. (2004). *Principles of Brain Evolution*. Sinauer Associates, Sunderland, Mass, 1 edition edition. 44

Strogatz, S. H. (2001). Exploring complex networks. *Nature*, 410(6825):268–276. 134

Sur, M. and Rubenstein, J. L. R. (2005). Patterning and Plasticity of the Cerebral Cortex. *Science*, 310(5749):805–810. 147

Swanson, L. W. (2012). *Brain Architecture: Understanding the Basic Plan*. OUP USA. 28

Tagliazucchi, E. and Laufs, H. (2014). Decoding Wakefulness Levels from Typical fMRI Resting-State Data Reveals Reliable Drifts between Wakefulness and Sleep. *Neuron*, 82(3):695–708. 16, 17

Tagliazucchi, E., von Wegner, F., Morzelewski, A., Borisov, S., Jahnke, K., and Laufs, H. (2012). Automatic sleep staging using fMRI functional connectivity data. *NeuroImage*, 63(1):63–72. 16

Tang, Y.-Y., Rothbart, M. K., and Posner, M. I. (2012). Neural correlates of establishing, maintaining, and switching brain states. *Trends in Cognitive Sciences*, 16(6):330–337. 43, 66

Tavor, I., Jones, O. P., Mars, R. B., Smith, S. M., Behrens, T. E., and Jbabdi, S. (2016). Task-free MRI predicts individual differences in brain activity during task performance. *Science*, 352(6282):216–220. 20

Thomas, C., Ye, F. Q., Irfanoglu, M. O., Modi, P., Saleem, K. S., Leopold, D. A., and Pierpaoli, C. (2014). Anatomical accuracy of brain connections derived from diffusion MRI tractography is inherently limited. *Proceedings of the National Academy of*

Sciences, 111(46):16574–16579. 29, 119

Thompson, G. J., Merritt, M. D., Pan, W.-J., Magnuson, M. E., Grooms, J. K., Jaeger, D., and Keilholz, S. D. (2013). Neural correlates of time-varying functional connectivity in the rat. *NeuroImage*, 83:826–836. 23, 49

Timofeev, I., Grenier, F., Bazhenov, M., Sejnowski, T. J., and Steriade, M. (2000). Origin of Slow Cortical Oscillations in Deafferented Cortical Slabs. *Cerebral Cortex*, 10(12):1185–1199. 140

Tong, Y. and Frederick, B. d. (2010). Time lag dependent multimodal processing of concurrent fMRI and near-infrared spectroscopy (NIRS) data suggests a global circulatory origin for low-frequency oscillation signals in human brain. *NeuroImage*, 53(2):553–564. 19

Tononi, G. and Massimini, M. (2008). Why Does Consciousness Fade in Early Sleep? *Annals of the New York Academy of Sciences*, 1129(1):330–334. 73

Trachtenberg, J. T., Chen, B. E., Knott, G. W., Feng, G., Sanes, J. R., Welker, E., and Svoboda, K. (2002). Long-term in vivo imaging of experience-dependent synaptic plasticity in adult cortex. *Nature*, 420(6917):788–794. 147

Traub, R. D., Miles, R., and Wong, R. K. (1989). Model of the origin of rhythmic population oscillations in the hippocampal slice. *Science*, 243(4896):1319–1325. 140

Tritsch, N. X., Yi, E., Gale, J. E., Glowatzki, E., and Bergles, D. E. (2007). The origin of spontaneous activity in the developing auditory system. *Nature*, 450(7166):50–55. 146

Trusina, A., Rosvall, M., and Sneppen, K. (2005). Communication Boundaries in Networks. *Physical Review Letters*, 94(23):238701. 166, 170

Tu, Y., Yu, T., Fu, X.-Y., Xie, P., Lu, S., Huang, X.-Q., and Gong, Q.-Y. (2011). Altered Thalamocortical Functional Connectivity by Propofol Anesthesia in Rats. *Pharmacology*, 88(5-6):322–326. 43

Turrigiano, G. G. and Nelson, S. B. (2004). Homeostatic plasticity in the developing nervous system. *Nature Reviews Neuro-*

science, 5(2):97–107. 146

van den Heuvel, M. P., de Reus, M. A., Feldman Barrett, L., Scholtens, L. H., Coopmans, F. M. T., Schmidt, R., Preuss, T. M., Rilling, J. K., and Li, L. (2015). Comparison of diffusion tractography and tract-tracing measures of connectivity strength in rhesus macaque connectome. *Human Brain Mapping*, 36(8):3064–3075. 31, 33

van den Heuvel, M. P., Mandl, R. C., Kahn, R. S., and Hulshoff Pol, H. E. (2009). Functionally linked resting-state networks reflect the underlying structural connectivity architecture of the human brain. *Human Brain Mapping*, 30(10):3127–3141. 34, 35

van der Want, J. J. L., Klooster, J., Nunes Cardozo, B., de Weerd, H., and Liem, R. S. B. (1997). Tract-tracing in the nervous system of vertebrates using horseradish peroxidase and its conjugates: tracers, chromogens and stabilization for light and electron microscopy. *Brain Research Protocols*, 1(3):269–279. 28

Van Dijk, K. R. A., Sabuncu, M. R., and Buckner, R. L. (2012). The influence of head motion on intrinsic functional connectivity MRI. *NeuroImage*, 59(1):431–438. 17

Varela, F., Lachaux, J.-P., Rodriguez, E., and Martinerie, J. (2001). The brainweb: Phase synchronization and large-scale integration. *Nature Reviews Neuroscience*, 2(4):229–239. 24

Vedel Jensen, E. B. and Thorarinsdottir, T. L. (2007). A Spatio-Temporal Model for Functional Magnetic Resonance Imaging Data with a View to Resting State Networks. *Scandinavian Journal of Statistics*, 34(3):587–614. 23

Vincent, J. L., Patel, G. H., Fox, M. D., Snyder, A. Z., Baker, J. T., Van Essen, D. C., Zempel, J. M., Snyder, L. H., Corbetta, M., and Raichle, M. E. (2007). Intrinsic functional architecture in the anaesthetized monkey brain. *Nature*, 447(7140):83–86. 6, 9, 16, 19, 70

Viswanathan, A. and Freeman, R. D. (2007). Neurometabolic coupling in cerebral cortex reflects synaptic more than spiking activity. *Nature Neuroscience*, 10(10):1308–1312. 15, 74

Vollenweider, F. X. and Kometer, M. (2010). The neurobiology

of psychedelic drugs: implications for the treatment of mood disorders. *Nature Reviews Neuroscience*, 11(9):642–651. 43

Wang, K., van Meer, M. P., van der Marel, K., van der Toorn, A., Xu, L., Liu, Y., Viergever, M. A., Jiang, T., and Dijkhuizen, R. M. (2011). Temporal scaling properties and spatial synchronization of spontaneous blood oxygenation level-dependent (BOLD) signal fluctuations in rat sensorimotor network at different levels of isoflurane anesthesia. *NMR in Biomedicine*, 24(1):61–67. 43

Wang, X. F. (2002). Complex networks: topology, dynamics and synchronization. *International Journal of Bifurcation and Chaos*, 12(05):885–916. 134

Watts, D. J. and Strogatz, S. H. (1998). Collective dynamics of small-world networks. *Nature*, 393(6684):440–442. 68, 105, 133, 164, 167, 169

Wedeen, V. J., Hagmann, P., Tseng, W.-Y. I., Reese, T. G., and Weisskoff, R. M. (2005). Mapping complex tissue architecture with diffusion spectrum magnetic resonance imaging. *Magnetic Resonance in Medicine*, 54(6):1377–1386. 29

Whitfield-Gabrieli, S. and Ford, J. M. (2012). Default Mode Network Activity and Connectivity in Psychopathology. *Annual Review of Clinical Psychology*, 8(1):49–76. 70

Whitfield-Gabrieli, S., Thermenos, H. W., Milanovic, S., Tsuang, M. T., Faraone, S. V., McCarley, R. W., Shenton, M. E., Green, A. I., Nieto-Castanon, A., LaViolette, P., Wojcik, J., Gabrieli, J. D. E., and Seidman, L. J. (2009). Hyperactivity and hyperconnectivity of the default network in schizophrenia and in first-degree relatives of persons with schizophrenia. *Proceedings of the National Academy of Sciences*, 106(4):1279–1284. 8, 148

Williams, K. A., Magnuson, M., Majeed, W., LaConte, S. M., Peltier, S. J., Hu, X., and Keilholz, S. D. (2010). Comparison of -chloralose, medetomidine and isoflurane anesthesia for functional connectivity mapping in the rat. *Magnetic Resonance Imaging*, 28(7):995–1003. 43

Wilson, C. J. and Kawaguchi, Y. (1996). The origins of two-state spontaneous membrane potential fluctuations of neostri-

atal spiny neurons. *The Journal of Neuroscience*, 16(7):2397–2410. 140

Wilson, H. R. and Cowan, J. D. (1972). Excitatory and Inhibitory Interactions in Localized Populations of Model Neurons. *Biophysical Journal*, 12(1):1–24. 84

Womelsdorf, T., Schoffelen, J.-M., Oostenveld, R., Singer, W., Desimone, R., Engel, A. K., and Fries, P. (2007). Modulation of Neuronal Interactions Through Neuronal Synchronization. *Science*, 316(5831):1609–1612. 24

Yan, L., Zhuo, Y., Ye, Y., Xie, S. X., An, J., Aguirre, G. K., and Wang, J. (2009). Physiological origin of low-frequency drift in blood oxygen level dependent (BOLD) functional magnetic resonance imaging (fMRI). *Magnetic Resonance in Medicine*, 61(4):819–827. 48

Yarom, Y. and Hounsgaard, J. (2011). Voltage Fluctuations in Neurons: Signal or Noise? *Physiological Reviews*, 91(3):917–929. 2

Yuste, R. (2011). Dendritic Spines and Distributed Circuits. *Neuron*, 71(5):772–781. 37

Yuste, R. (2015). From the neuron doctrine to neural networks. *Nature Reviews Neuroscience*, 16(8):487–497. 37

Yvert, B., Branchereau, P., and Meyrand, P. (2004). Multiple Spontaneous Rhythmic Activity Patterns Generated by the Embryonic Mouse Spinal Cord Occur Within a Specific Developmental Time Window. *Journal of Neurophysiology*, 91(5):2101–2109. 146

Zalesky, A., Fornito, A., Cocchi, L., Gollo, L. L., and Breakspear, M. (2014). Time-resolved resting-state brain networks. *Proceedings of the National Academy of Sciences*, 111(28):10341–10346. 23

Zamora-López, G., Chen, Y., Deco, G., Kringelbach, M. L., and Zhou, C. (2016). Functional complexity emerging from anatomical constraints in the brain: the significance of network modularity and rich-clubs. *arXiv:1602.07625 [q-bio]*. arXiv: 1602.07625. 39, 170

Zamora-López, G., Zhou, C., and Kurths, J. (2011). Exploring

brain function from anatomical connectivity. *Frontiers in Neuroscience*, 5:83. 94

Zhang, N., Rane, P., Huang, W., Liang, Z., Kennedy, D., Frazier, J. A., and King, J. (2010). Mapping resting-state brain networks in conscious animals. *Journal of Neuroscience Methods*, 189(2):186–196. 43, 68

Zhang, X. S., Roy, R. J., and Jensen, E. W. (2001). EEG complexity as a measure of depth of anesthesia for patients. *IEEE Transactions on Biomedical Engineering*, 48(12):1424–1433. 73

Zhou, C., Zemanov, L., Zamora-López, G., Hilgetag, C. C., and Kurths, J. (2007). Structurefunction relationship in complex brain networks expressed by hierarchical synchronization. *New Journal of Physics*, 9(6):178. 39, 94

Zuo, X.-N. and Xing, X.-X. (2014). Test-retest reliabilities of resting-state FMRI measurements in human brain functional connectomics: A systems neuroscience perspective. *Neuroscience & Biobehavioral Reviews*, 45:100–118. 20, 22